

p-type Gallium Nitride Semiconductor Development and  
Characterization for LEDs and other Devices

by  
Gregorey L. Togtema

A Thesis  
Presented to Lakehead University  
in Partial Fulfillment of the Requirement for the Degree of  
Master of Science  
in  
Electrical and Computer Engineering

Thunder Bay, Ontario, Canada

May 6, 2013

ProQuest Number: 10611956

All rights reserved

INFORMATION TO ALL USERS

The quality of this reproduction is dependent upon the quality of the copy submitted.

In the unlikely event that the author did not send a complete manuscript and there are missing pages, these will be noted. Also, if material had to be removed, a note will indicate the deletion.



ProQuest 10611956

Published by ProQuest LLC (2017). Copyright of the Dissertation is held by the Author.

All rights reserved.

This work is protected against unauthorized copying under Title 17, United States Code  
Microform Edition © ProQuest LLC.

ProQuest LLC.  
789 East Eisenhower Parkway  
P.O. Box 1346  
Ann Arbor, MI 48106 - 1346

## Abstract

Gregorey L. Togtema. p-type Gallium Nitride Semiconductor Development and Characterization for LEDs and other Devices (Under the Supervision of Dr. D. Alexandrov and Dr. K. S. A. Butcher).

Migration Enhanced Afterglow (MEAglow) is proposed as a fabrication technology to produce high indium content indium gallium nitride (InGaN) LEDs operating in the green wavelengths. This research presents results for the first confirmed p-type gallium nitride films grown in a MEAglow system for these applications. Films were fabricated at a variety of low temperatures, illustrating the technology's capability to grow p-GaN at indium preserving conditions for high indium content InGaN LEDs.

Films were resistive and exhibited a degree of codoping that stemmed from background oxygen concentration present during growth, rendering Hall effect measurements unsuitable. Electroluminescent spectra exposed three different emission sources: that from the bandgap, that from magnesium to nitrogen vacancy transitions, and the well known yellow defect. Current-Voltage characterization of films grown on top of an n-GaN template determined the Fermi level inside the p-layer, yielding a net hole concentration of  $9.9 \times 10^{16} \text{cm}^{-3}$  in one film. p-GaN semiconductors were investigated using Scanning Electron Microscopy (SEM), Atomic Force Microscopy (AFM), transmission spectroscopy and X-Ray Diffraction (XRD). It was found that growth rate decreased as the growth temperature increased from  $545^{\circ}\text{C}$  to  $635^{\circ}\text{C}$ , indicating the desorption of gallium and nitrogen from the lattice at low growth pressures. Conditions used in the fabrication of films were also conducive to producing nanowires and nanostructures, which were shown to correlate with a decrease in luminosity; a worsening of the crystal structure, and is indicative of metal rich material. Attempts were made at optimizing the molecular flow rates of gallium, nitrogen and magnesium to yield better materials.

A single heterojunction GaN-InGaN LED was fabricated using the material studied in this thesis. It was shown that a small degree of codoping reduced the resistivity of commercially acquired p-GaN by two orders of magnitude, down to  $0.038\Omega \cdot cm$ . This p-GaN was placed below an InGaN active layer, removing the need for magnesium doping at low temperatures. The low series resistance along the p-GaN material allowed large currents to be applied without much overheating. The high indium content InGaN layer produced yellow light with high electrical conversion efficiency not usually characteristic of nitride or phosphide semiconductor LEDs.

## Biographical Summary

Gregorey L. Togtema is an electrical engineer, graduated from University of Toronto's Engineering Sciences undergraduate program in 2008. He has over three years of industrial engineering experience in both the medical and computer hardware sectors. His work on introducing a new 16-channel RF coil antenna array for breast cancer imaging in an MRI setting gave the receiver architecture for a new line of second generation products, furthering technology that won the prestigious R&D Magazine's Innovator of the Year award. He has also developed analog and digital instrumentation and processes for two other collaborations - MEAglow included - who have won innovation awards, including a novel ultrasound based prostate cancer ablation system guided by real-time medical imaging. Greg is a member of the IEEE, acting as vice chair of Lakehead's student branch during his Master's degree, and was a member of the school's hybrid electric vehicle team, designing power electronics for battery charging applications. With the completion of this M.Sc. degree, he should have all qualifications to obtain his professional engineering license.

## Acknowledgments

With high regards, I would like to thank Dr. Scott Butcher for his direct supervision. The impact of his involvement is seen by the industrial relevance, technical accuracy and sound presentation of this work. He has a genuine concern for those that work for him and devotes a substantial amount of time to address their needs. This author also recognizes the technological know how, infrastructural development and the economic overhead required in producing this work. That is why I would like to thank Dr. Dimiter Alexandrov for the establishment of the lab, the grant funding to continue the research operations, and the administrative liaisons he employed to facilitate the requirements of this degree. Coworkers Vasil Georgiev, Dimka Georgieva, Rositsa Gergova, Peter Binsted and Penka Terziyska have helped fabulously, quickly bringing me up to speed so I could complete my research in a timely manner. Additionally, they are great comrades after hours, and made my time at Lakehead enjoyable. Lastly, the author would like to thank his family. His creative ability he learned from his mother, H el ene, and his ingenuity from his father, John. Lastly, his wife, Melissa (Ph. D. candidate, Biology), is truly an inspiration. She sets her research standards so high that it is encouraging to follow suit. She also gratefully directed this research by playing devil’s advocate, ensuring it did not go down a fruitless path.

Greg Togtema

gtogtema@lakeheadu.ca

*"Ice is slippery.*

*You could either say, I'm satisfied with that. You've answered me. Ice is slippery; that explains it. Or you could go on to say, why is ice slippery? Then you're involved with something."*

Richard Feynman

# Contents

<b>List of Symbols</b>	<b>vii</b>
<b>List of Abbreviations</b>	<b>ix</b>
<b>List of Figures</b>	<b>xi</b>
<b>List of Tables</b>	<b>xv</b>
<b>1 Introduction</b>	<b>1</b>
1.1 Plasma-Enabled Low Temperature Nitride Growth . . . . .	3
1.2 Technological Considerations of p-GaN Fabrication . . . . .	4
1.3 Research Motivation and Thesis Outline . . . . .	6
<b>2 Nitride Based LEDs</b>	<b>8</b>
2.1 GaN - Sapphire Nucleation Layers . . . . .	10
2.2 GaN - Sapphire Buffer Layers . . . . .	12
2.3 Impurity Doping and Carrier Concentration of Gallium Nitride . . . . .	16
2.3.1 Background Electron Concentration . . . . .	16
2.3.2 Acceptor Doping in GaN . . . . .	18
2.4 Growth Technology . . . . .	21
2.4.1 Chemical Vapour Deposition (CVD) . . . . .	22
2.4.2 Plasma Based Growth . . . . .	23
2.4.3 Molecular Beam Epitaxy (MBE) . . . . .	26
2.4.4 Migration Enhanced Afterglow (MEAglow) . . . . .	27

2.5	LED Structures . . . . .	31
2.5.1	Quantum Well LEDs . . . . .	32
2.5.2	LED Packaging . . . . .	35
2.6	Chapter Summary . . . . .	36
<b>3</b>	<b>Feasibility and Characterization of Magnesium Doped GaN Fabrication</b>	<b>38</b>
3.1	p-GaN Electroluminescence . . . . .	39
3.2	Electrical Properties Measured by Hall Effect . . . . .	47
3.2.1	Introduction to the Hall Effect Measurement . . . . .	47
3.2.2	Derivation of Carrier Concentration . . . . .	48
3.2.2.1	Four point resistivity and the Van der Pauw Method . . . . .	50
3.2.3	Isotropy, Ohmic and Schottky contacts . . . . .	54
3.2.3.1	Experimental verification of ohmic contacts to GaN . . . . .	57
3.2.4	Hall Measurements on GaN . . . . .	61
3.3	Fermi Level Measurement through I-V Characteristics . . . . .	71
3.4	Chapter Summary . . . . .	76
<b>4</b>	<b>p-type GaN Film Development</b>	<b>78</b>
4.1	MEAgrow growth technology and conditions . . . . .	79
4.1.1	Growth Procession . . . . .	83
4.2	Experimental Fabrication of Magnesium Doped GaN for Analysis . . . . .	84
4.3	Film Investigation through Scanning Electron Microscopy (SEM) . . . . .	86
4.4	Film Investigation through Atomic Force Microscopy (AFM) . . . . .	94
4.5	Gallium Nitride Bandgaps . . . . .	101
4.6	Gallium Nitride Crystallinity observed by X-Ray Diffraction (XRD) . . . . .	109
4.7	P-GaN Growth Optimization . . . . .	114
4.8	Chapter Summary . . . . .	118
<b>5</b>	<b>Inverted High Indium Content InGaN LEDs with Codoped P-type Layer</b>	<b>120</b>
5.1	Active Layer Growth . . . . .	123

5.2	Verification of Device Structure . . . . .	124
5.3	Device Performance . . . . .	126
5.4	Chapter Summary . . . . .	130
<b>6</b>	<b>Conclusions and Future Work</b>	<b>131</b>

# List of Symbols

$\hbar$  Normalized Planck's constant,  $h = \hbar/2\pi$

$\lambda$  Electromagnetic wavelength

$k_b$  (or  $k$ ) Boltzmann constant

$III : V$  The ratio of group three atoms from the periodic table to that of group five

$E_a$  Activation energy

$N^*$  Nitrogen plasma

$p$  Hole concentration in  $cm^{-3}$

$n$  Electron concentration in  $cm^{-3}$

$N_a$  Acceptor impurity concentration in  $cm^{-3}$

$N_d$  Donor impurity concentration in  $cm^{-3}$

$V_{Ga}$  Gallium vacancy

$V_H$  Hall voltage

$R_H$  Hall coefficient

$\rho$  Sample resistivity in  $\Omega \cdot cm$

$R_{ABCD}$  Four point resistivity measured as  $R_{ABCD} = V_{AB}/I_{CD}$

$\sigma$  Sample conductivity

$\mu_p$  Hole mobility in  $cm^2/(V \cdot s)$

$\mu_n$  Electron mobility in  $cm^2/(V \cdot s)$

$r$  Hall scattering factor

$\phi$  or  $\psi$  Semiconductor band potential

$\varepsilon$  The dielectric constant. ( $\varepsilon = \varepsilon_o \varepsilon_r$ ), where  $\varepsilon_o$  is the relative permittivity of free space

$F$  Fermi level

$F_p$  The Fermi level inside an isolated p-type material

$F_n$  The Fermi level inside an isolated n-type material

$\alpha$  Optical attenuation

$h\nu$   $h$  : Planck's constant,  $\nu$  : frequency of light

$E_g$  Bandgap energy

# List of Abbreviations

**AFM** Atomic Force Microscopy

**CP<sub>2</sub>Mg** Biscyclopentadienyl-magnesium

**CVD** Chemical Vapour Deposition

**DC** Direct Current

**EL** Electroluminescence

**FWHM** Full Width at Half Maximum

**LEEBI** Low Energy Electron Beam Irradiation

**LED** Light Emitting Diode

**lm** Lumens, a measure of light intensity

**HVPE** Hydride (or Halide) Vapour Phase Epitaxy

**LCD** Liquid Crystal Display

**LEO** Lateral Epitaxial Overgrowth

**LD** Laser Diodes

**MBE** Molecular Beam Epitaxy

**MEAglow** Migration Enhanced Afterglow

**MFC** Mass Flow Controller

**MME** Metal Modulated Epitaxy

**MOCVD** Metal Organic Chemical Vapour Deposition

**MQW** Multi-Quantum Well

**ODS** Optical Density Squared

**QW** Quantum Well

**RF** Radio Frequency

**RMS** Root Mean Squared

**RPECVD** Remote Plasma Enhanced CVD

**SEM** Scanning Electron Microscopy (or microscope)

**SNR** Signal to Noise Ratio

**SQW** Single Quantum Well (a.k.a. QW)

**TD** Threading Dislocations

**TEM** Transmission Electron Micrograph

**TMG** Trimethylgallium

**XRD** X-Ray Diffraction

# List of Figures

## Chapter 1: Introduction

1.1 LED efficiency of semiconductor alloys .....	3
1.2 P-N junction structure of an LED .....	5
1.3 Stacking configuration of an LED .....	6

## Chapter 2: Nitride Based LEDs

2.1 LED in the MESA structure .....	9
2.2 TEM image of threading dislocations .....	10
2.3 Surface phase diagram for GaN growth .....	12
2.4 Lattice constant mismatch .....	14
2.5 Effect of buffer layer thickness .....	15
2.6 Lateral epitaxial overgrowth (LEO) .....	16
2.7 Nitrogen plasma energy levels .....	25
2.8 Growth rates of GaN in MBE .....	26
2.9 MBE system structure .....	27
2.10 Plasma source architectures .....	30
2.11 The hollow cathode source .....	31
2.12 A Langmuir probe .....	31
2.13 Single quantum well .....	34
2.14 Multi quantum well .....	35

## **Chapter 3: Feasibility and Characterization of Magnesium Doped GaN Fabrication**

<b>3.1</b>	Surface Oxide .....	40
<b>3.2</b>	Magnesium energy level .....	41
<b>3.3</b>	GaN:Mg - GaN:Si structure with exposed sublayer .....	42
<b>3.4</b>	EL spectrum of MEAgrow grown GaN .....	43
<b>3.5</b>	EL spectrum of MEAgrow grown by MOCVD .....	44
<b>3.6</b>	Weak signal version of Figure 3.5 .....	46
<b>3.7</b>	Hall measurement of a bar sample .....	48
<b>3.8</b>	Four point probe setup .....	51
<b>3.9</b>	Van der Pauw contact position .....	52
<b>3.10</b>	Metal-Semiconductor junction .....	55
<b>3.11</b>	Metal-Semiconductor junction band diagram .....	56
<b>3.12</b>	Hall effect test circuit board .....	58
<b>3.13</b>	Ohmic contact verification of indium .....	59
<b>3.14</b>	Sample preparation of p-GaN film .....	60
<b>3.15</b>	Ohmic contact verification of gold .....	61
<b>3.16</b>	p-type germanium Hall sample .....	65
<b>3.17</b>	Temperature dependent Hall effect enclosure .....	69
<b>3.18</b>	Simulation of temperature dependence of codoped p-GaN .....	71
<b>3.19</b>	Current-Voltage characterizaiton of p-GaN films .....	74
<b>3.20</b>	I-V curves of Figure 3.19 with series resistance removed .....	75

## Chapter 4: p-type GaN Film Development

4.1 Gas flow system of MEAglow reactor .....	82
4.2 Growth timing diagram .....	83
4.3 Sapphire placement on reaction chamber sample holder .....	85
4.4 Sample holder for SEM imaging .....	88
4.5 SEM cross sectional images of p-GaN .....	89
4.6 Surface SEM images of p-GaN .....	91
4.7 Film thickness as a function of temperature .....	92
4.8 SEM images of nanowires .....	93
4.9 Columnar structure of GaN .....	94
4.10 AFM operational diagram .....	95
4.11 AFM images of GaN grown by HVPE .....	97
4.12 AFM images of GaN grown by MEAglow .....	99
4.13 Band structure of GaN .....	102
4.14 Transmission spectrophotometry probing setup .....	102
4.15 Transmission spectrum of p-GaN grown by HVPE .....	104
4.16 Fabry P�erot cavity .....	105
4.17 Transmission spectrum of p-GaN grown by MEAglow .....	106
4.18 Optical density squared response .....	107
4.19 XRD curve of p-GaN grown by MEAglow, wide span .....	110

4.20	XRD curve of p-GaN grown by MEAglow, narrow span .....	112
4.21	Transmission spectrum of sample grown with smaller CP <sub>2</sub> Mg flow .....	116
4.22	AFM image of sample studied in Figure 4.21 .....	117
4.23	XRD curve of sample studied in Figure 4.21 .....	118

**Chapter 5: Inverted High Indium Content InGaN LEDs with Codoped P-type Layer**

5.1	Inverted single heterojunction LED structure .....	122
5.2	Current-Voltage characterization of single heterojunction LED .....	125
5.3	Surface oxide effect of single heterojunction LED .....	126
5.4	Photo of light emission from LED .....	128
5.5	Electroluminescence spectrum of single heterojunction LED .....	129
5.6	Energy bandgap bowing characteristics of InGaN .....	130

# List of Tables

## **Chapter 3: Feasibility and Characterization of Magnesium Doped GaN Fabrication**

<b>3.1</b> Hall effect results of p-GaN .....	63
<b>3.2</b> Hall effect results of p-Ge .....	65
<b>3.3</b> Temperature dependent Hall effect results of p-GaN .....	69

## **Chapter 4: p-type GaN Film Development**

<b>4.1</b> Film thickness of magnesium doped GaN .....	90
<b>4.2</b> Surface roughness of p-GaN grown by MEAgrow .....	101
<b>4.3</b> Measured bandgaps of GaN .....	109
<b>4.4</b> XRD results of GaN grown by MEAgrow and HVPE .....	113

# Chapter 1

## Introduction

Over the past two decades, gallium nitride has emerged as a material for use in optoelectronic, microwave and high power electronic applications. Despite the presence of extended defects, it exhibits extraordinarily high electrical-optical conversion efficiencies, high saturation velocities and large breakdown voltages. As a result, devices can be interfaced with short wavelength light and be switched quickly under high power densities, making the material suitable for Light Emitting Diodes (LEDs), Laser Diodes (LD) and microwave power amplifiers. While gallium arsenide and silicon already represent most of the microwave transistor market [1], no other material addresses so many of the current needs of solid state lighting. Firstly, GaN produces blue light very efficiently on account of a  $2.85eV$  interband energy transition [2], thus justifying its use in laser diode based high density optical storage systems like that of a Blu-Ray<sup>(TM)</sup> system. Secondly, according to the Planck relation,  $E = 2\pi\hbar c/\lambda$ , its 3.4 electron volt bandgap signifies that light can be produced in the near ultraviolet region [3]. Thirdly, when combined in a ternary configuration with a lower energy bandgap material, say indium nitride, its bandgap approximately becomes a weighted fraction of the two. Thus, light-emitting carrier recombination of  $In_xGa_{1-x}N$ <sup>1</sup> can occur at any energy level between indium nitride's  $0.7eV$  bandgap [3] and that of GaN, potentially producing light at any desired wavelength in this range.

---

<sup>1</sup> $x$  is the mole fraction

This ternary alloy is thus a candidate material to solve a serious shortcoming in LED technology, the “Green Gap.” Currently, there is no material that adequately serves the needs of solid state lighting in the green,  $520 - 580nm$ , region [4]; each existing technology has its drawback. For instance, *II - VI* semiconductors<sup>2</sup> like magnesium sulfide (MgS) and zinc selenide (ZnSe) emit green light at high radiation powers, but have lifetimes of only a couple hundred hours due to their low atomic bonding strengths [5]. Alloys of gallium and phosphorous, GaP, also produce green light, but the materials have low internal quantum efficiencies<sup>3</sup> on account of their indirect bandgaps. This is why some full colour displays (red-green-blue) do not have as pleasing a colour spectrum [6]. By tuning the indium mole fraction, InGaN’s high output power and reliability in the blue spectra could possibly be a solution for the green emission in these devices.

As can be seen from Figure 1.1, however, the quantum efficiency of III-V semiconductor alloys drops in the green region. For InGaN, this is due to the attributes of thin film growth of indium. Segregation at high concentrations, diffusion across device layers, island nucleation and decomposition<sup>4</sup> from the alloy all serve to lower the indium incorporation in the semiconductor lattice [7, 8, 9, 10]. From this separation, the structure more strongly resembles that of gallium nitride and has a tendency to emit blue light rather than green. One of the most popular methods to remediate these defects is to grow at low temperatures. Unlike typical chemical vapour deposition (CVD) epitaxy of GaN, which occurs at temperatures in excess of  $1000^{\circ}C$ , environments below  $600^{\circ}C$  preserve the indium composition better [11, 12]. Therefore, in addition to multitude of other growth parameters (growth rates, molecular partial pressures, etc.), proper growth temperature can play a significant role in the colour of emission from the LED.

---

<sup>2</sup>Formed by the bond between a group II element on the periodic table and one from the group VI

<sup>3</sup>The conversion efficiency between charge carrier recombination and emitted photons

<sup>4</sup>Spinoidal decompositions - the unmixing of elements in a solution

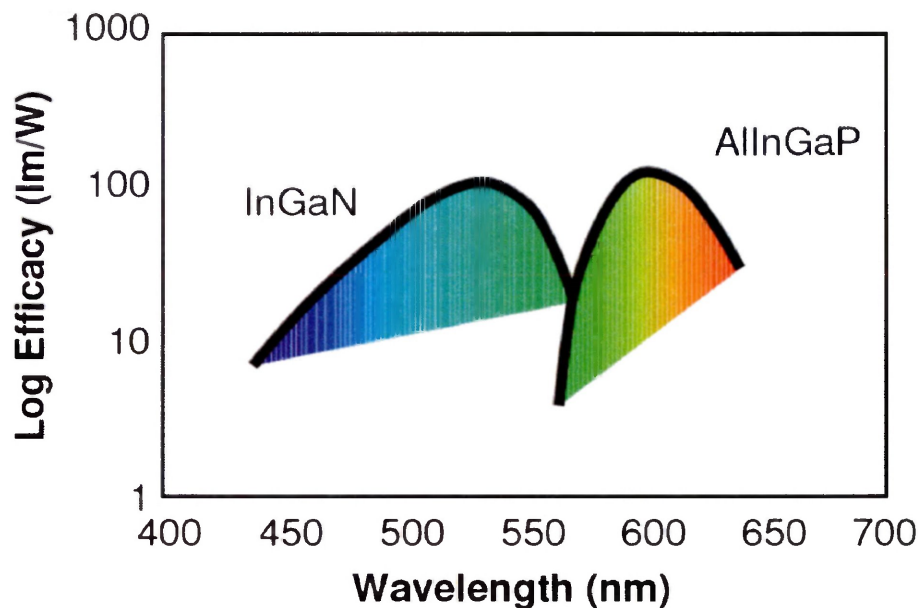


Figure 1.1: The reported efficiency of LED structures from two well established III-V semiconductor alloys as of the year 2012. As can be seen, both have reduced emission in the green region of the visible spectrum. Picture taken from [9].

## 1.1 Plasma-Enabled Low Temperature Nitride Growth

While lower temperatures are sought, this places a constraint on the gases used for deposition. The commonly used nitrogen source, ammonia, cracks most efficiently at  $1100^{\circ}\text{C}$  [13] and is less useful for deposition at lower temperatures; it has been used as low as the mid  $600^{\circ}\text{C}$ , but the deposition rates are extremely low [14]. The use of nitrogen plasma, on the other hand, is independent of temperature and provides nitrogen atoms with sufficient energy to incorporate themselves into the GaN lattice. By exciting pure nitrogen gas with electric or magnetic fields at either DC, radio frequency (RF) or microwave frequencies, electrons can be excited to higher energy level orbitals, giving the atom the required potential energy for growth. As a result, plasma can be made from a multitude of source architectures to create different growth methodologies like Remote Plasma Enhanced CVD (RPECVD) and Plasma Assisted Molecular Beam Epitaxy (MBE) [15, 16]. The Semiconductor Lab at Lakehead University has developed a new

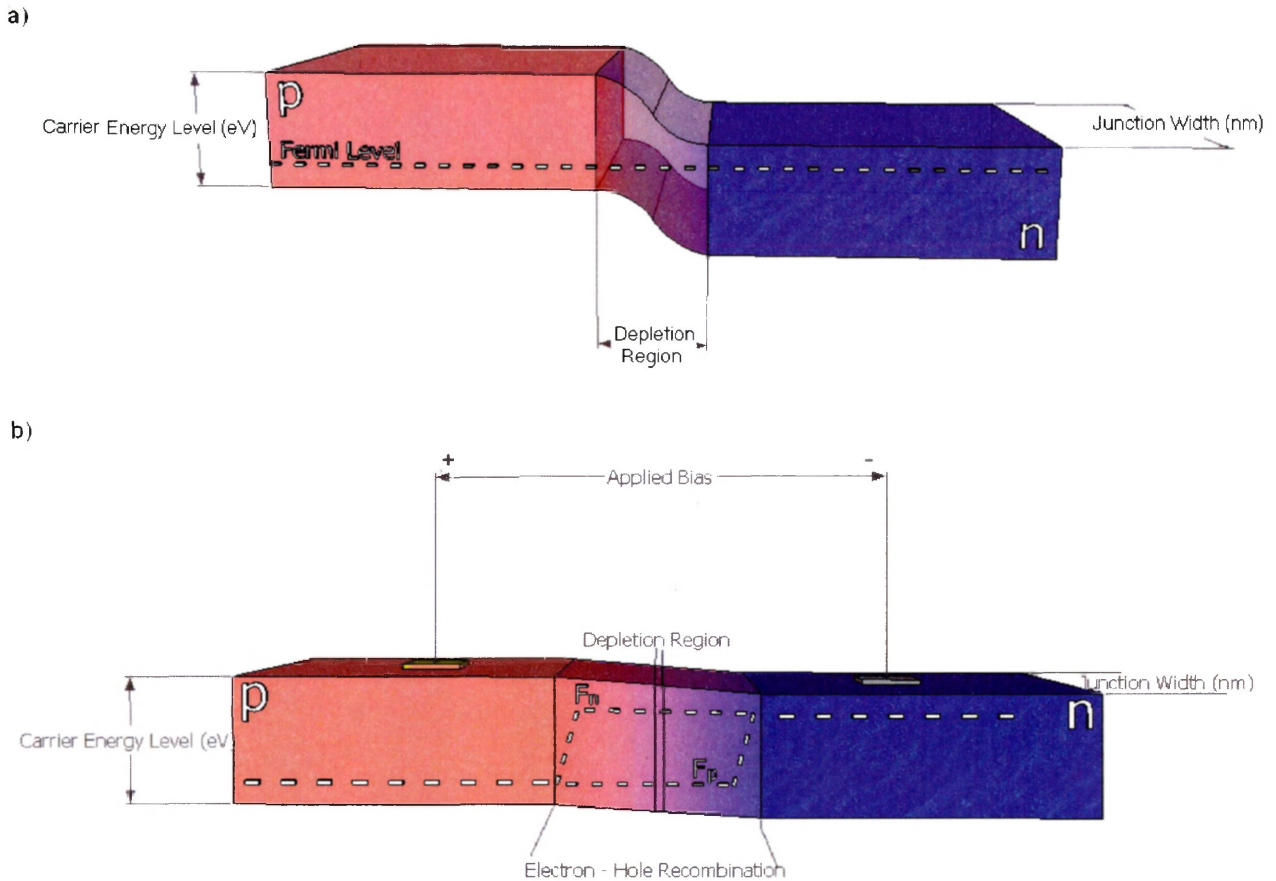
plasma architecture. Coined “MEAglow” (Migration Enhanced Afterglow), its hollow cathode plasma source is distant from the growth surface like that of RPECVD, but is also scalable to provide high volume production of large films [17, 18]. From this configuration, InGaN materials emitting strong yellow light have been produced<sup>5</sup>.

## 1.2 Technological Considerations of p-GaN Fabrication

Being in its infancy, however, certain attributes of nitride semiconductor growth using MEAglow have not yet been optimized. In particular, p-type conductivity has not been achieved. Therefore, a full LED structure cannot be fabricated in the current facilities. Further, creating the most efficient LED requires the p-type carrier concentration to be as high as possible. Formed by a p-n junction, an LED produces light when p-type carriers diffuse across the junction and perform photoelectric recombination with n-type electrons as shown in Figure 1.2; the same happens with n-type diffusion. Therefore, having more holes in the p-type layer helps produce more light, and thus the highest carrier concentration is desired.

---

<sup>5</sup>Data presented but not published at ISSLED 2012 conference in Germany



1.2: a) A p-n junction with pink and blue colours representing hole and electron concentrations respectively. b) When under bias, minority carriers drift and diffuse across the junction, producing light when they combine with majority carriers.

Achieving p-type conductivity in gallium nitride is notably difficult for various reasons. Firstly, there are no acceptor impurities having a shallow activation energy relative to the valence band. Magnesium's activation energy is the lowest, and its value is large at  $150 - 209\text{meV}$ <sup>6</sup> [14]. Since thermal energy<sup>7</sup>,  $E = f \cdot \frac{1}{2}k_bT$ , is the only driving force for acceptor activation at equilibrium, a temperature of over  $1700^\circ\text{C}$  is needed to induce all possible carriers. Hence, at room

<sup>6</sup>The variation is due to the measurement methodology

<sup>7</sup> $k_b$  is the Boltzmann constant, and  $f$  is the number of degrees of freedom

temperatures, less than one in 100 magnesium dopant atoms form p-type carriers. The second impediment to p-type conductivity is that magnesium has a self-compensating mechanism. If there is too much magnesium, the acceptor impurities can change into an independent structure [19], and it is an accepted theory that they can become compensated by the deep donor energy state of nitrogen vacancies [20, 21]. Therefore, while increasing the magnesium concentration should increase the hole density, too much will, in fact, reduce this value. Thirdly, the magnesium atoms can form binding complexes with ambient hydrogen [14]. Not being integrated into the GaN lattice, it does not accept electrons, and thus no holes are formed. To ameliorate this problem, certain treatment methods are required to activate the magnesium as an acceptor after film growth with ambient hydrogen species.

With regards to an LED structure, the p-type GaN layer is difficult to fabricate since it, too, must be grown at relatively low temperatures. Most InGaN based light emitting semiconductors are grown atop an n-type GaN (n-GaN) and below a p-type GaN (p-GaN) layer, sandwiching the active InGaN layer in between (Figure 1.3) - this configuration is known as a quantum well LED. The overlying p-GaN must be grown at a temperature low enough that the underlying InGaN is not adversely degraded.

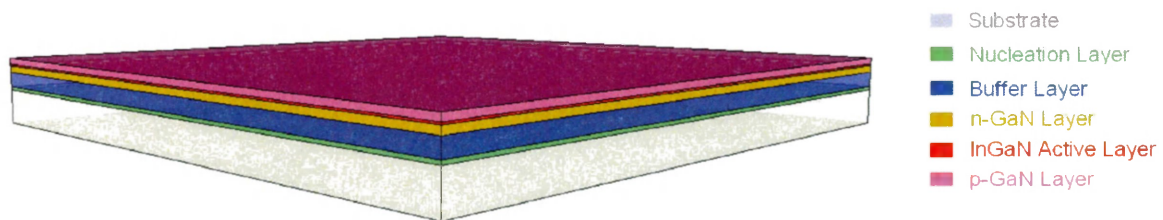


*Figure 1.3 : The n-GaN / InGaN / p-GaN stacking configuration of an LED*

### 1.3 Research Motivation and Thesis Outline

This thesis seeks to demonstrate feasibility and develop the quality of p-type gallium nitride films using a system that employs MEAgrow methodology. Effective p-GaN growth should facilitate the realization of the benefits of MEAgrow technology in the fabrication of GaN-InGaN

LEDs. The ability to fabricate this material at indium preserving temperatures is assessed to judge the relevance to LED applications. To gauge the materials' capabilities, a characterization regime is established first using p-GaN grown by CVD, and thereafter its suitability is assessed when applied to material produced in the MEAgrow system. This knowledge is then applied to the growth of magnesium doped GaN films to determine the parameters necessary to grow adequate layers. Finally, low resistivity p-GaN material motivates the fabrication and testing of an unconventional inverted single heterojunction LED as an alternative to low temperature p-GaN overgrowth on InGaN.

# Chapter 2

## Nitride Based LEDs

Depicted in Figure 1.2 of the previous chapter is an LED structure which emits light when majority carriers flow into oppositely doped semiconductor regions under a sufficient bias. As the applied forward bias yields the flat band condition, charge carriers from both regions diffuse and drift into the opposite region and produce light due to photoelectric recombination. However, this p-n structure does not occur naturally, and must be intentionally fabricated. While it was discovered over 70 years ago that GaN can be crystallized into thin needles by flowing ammonia over hot gallium [14], any functional semiconductor device should follow the established manufacturing technology of epitaxy, the layered growth on a base substrate. That is why GaN based LEDs have been developed into a layered structure such as that shown in Figure 2.1; here, the underlying n-type material is exposed using what is called a Mesa structure so that electrical contacts can be formed at the p and n layers.

The technological growth method to undergo this epitaxy can be addressed through many architectures. For instance, the gallium and nitrogen used to form GaN can be brought into a high temperature reaction chamber in a molecular precursor form - ammonia ( $\text{NH}_3$ ) and trimethyl-gallium ( $((\text{CH})_3\text{Ga})$ ) - as in Chemical Vapour Deposition (CVD), or they can be focused onto the substrate in a beam of atoms or molecules as done in Molecular Beam Epitaxy (MBE). Epitaxy can also occur through sputtering, where energized atoms dissociate from bulk material and

“shower” down on the substrate, and a similar process can be induced by pulsed laser deposition, where a laser is aimed at a bulk target to perform this dissociation [14, 22]. An emerging approach to fabricating GaN is to use a nitrogen plasma instead of ammonia [15]. The necessary growth temperature when using this source is much lower than that of CVD, and this prevents many problems associated with poor indium incorporation as occurs at higher temperatures. Since the film growth architecture used in this research is based on this principle, the chapter at hand will investigate its potential advantages and disadvantages relative to the other epitaxy methods described above.

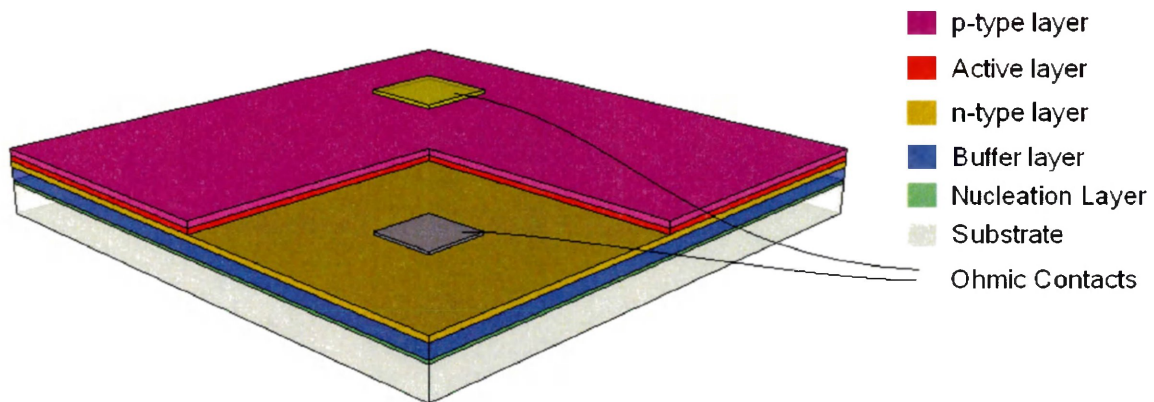


*Figure 2.1: An LED formed in a Mesa structure. Here, a forward bias is applied to the p-type and n-type layers through their ohmic contacts, transporting charge across the active layer.*

*Note: the diagram is not to scale since the layers' thicknesses range between 10 – 3000nm while the device width can be 300 $\mu$ m or larger.*

Simply employing MOCVD or MBE as they have been used for more mature semiconductors, like gallium arsenide and silicon, however, will not yield usable GaN material. Many attempts were made in the 1960s to do just that, and while GaN was in fact grown, it was difficult to fabricate high quality material. In particular, growth was 3 dimensional as opposed to 2D layered epitaxy, and the resulting films had a high density of lattice dislocations (Figure 2.2) because

GaN was grown on a foreign material, usually sapphire ( $\text{Al}_2\text{O}_3$ ). By growing GaN in a two-step sequence, layered growth was promoted. Applying a thin ( $10 - 100\text{nm}$ ), well spread out buffer layer before desired film growth provided a good base for 2D growth [24]. Hence, any subsequent growth tended to follow the layered base, rather than forming islands. The lattice dislocations were reduced by distancing the film surface from the sapphire interface. By growing a second, thicker,  $1 - 3\mu\text{m}$  buffer layer on top of the first, few dislocations penetrate far enough to reach the surface. Therefore, subsequent epilayer growth on top of this buffer had a higher integrity.

Clarification must be made at this point with regards to terminology. The very thin layer used to facilitate 2D growth was termed a ‘buffer layer’ when it was first introduced. Nowadays, the term buffer layer is reserved for the thick,  $1 - 3\mu\text{m}$  GaN layers used to reduce the defect density. The very thin,  $10 - 100\text{nm}$  GaN layer is usually now referred to as a nucleation layer, or seed layer.



*Figure 2.2: Threading dislocations protruding upward from the sapphire substrate located at the figure's bottom. Image is of a Transmission Electron Microscope (TEM) taken from [23].*

## 2.1 GaN - Sapphire Nucleation Layers

As indicated, nucleation (or seed) layers are used to improve the layered nature of growth. The first used was aluminum nitride (AlN), because its lattice constant is a good match to GaN,

and the result produced impressive results; both the electrical and optical characteristics of the GaN epilayer were far superior to that without the buffer. The material's carrier mobility, as measured by a Hall effect system, was more than three times its seedless counterpart, and its peak luminosity measured by cathodoluminescence<sup>1</sup> was 25 times larger [24]. By improving the film integrity, fewer drift scattering mechanisms were available to slow down charge flow, allowing greater diffusion of minority carriers into doped regions for luminescence.

Nine years later, it was shown that using a GaN nucleation layer grown at low temperatures yielded epilayers with better performance. At the optimal interface thickness, the Hall mobility at room temperature was shown to be almost two times larger than material grown with AlN only [25]. Further, the intrinsic background electron concentration, hypothetically arising from dislocations defects, among other debated sources, was an order of magnitude lower ( $10^{16} \text{ cm}^{-3}$  vs.  $10^{17} \text{ cm}^{-3}$ ). Hence, it is no surprise that most growths now begin with this thin, GaN nucleation layer ([10, 29], the references therein, and many others).

The specifics of its growth are rather important. To begin, a high temperature nitridation process ensures the proper AlN monolayer is deposited. Since GaN growth tends to be localized in islands, growing with a 3-dimensional characteristic, the nitride layer facilitates more 2-D planar growth. Next, a thin ( $10 \rightarrow 100 \text{ nm}$ ) GaN nucleation layer is grown at a low temperature ( $450 \rightarrow 600^\circ \text{C}$  [25]). Low temperatures promote a supersaturated growth regime on the film surface, at least for the MBE growth of GaN using plasma reported in [26] and shown in Figure 2.3. This forces the gallium and nitrogen to deposit where vacancies would normally occur. Hence, using low temperatures and filling the reaction chamber with excess  $N_2$  (and historically,  $H_2$ ) is crucial for growth of this nucleation layer in order to allow for smoother films. Sometimes, this thin GaN layer is annealed at a higher temperature to recrystallize the gallium and nitrogen [28, 29]. Since the nucleation was done at low temperatures, subjecting the layer to heat is a good way to remediate nitrogen rich or gallium rich conditions and achieve the desired regime

---

<sup>1</sup>Optical emission due to an incident electron beam

(the transition region, Figure 2.3). At this point, the GaN epilayer is ready to be deposited on the structure with improved results presented above.

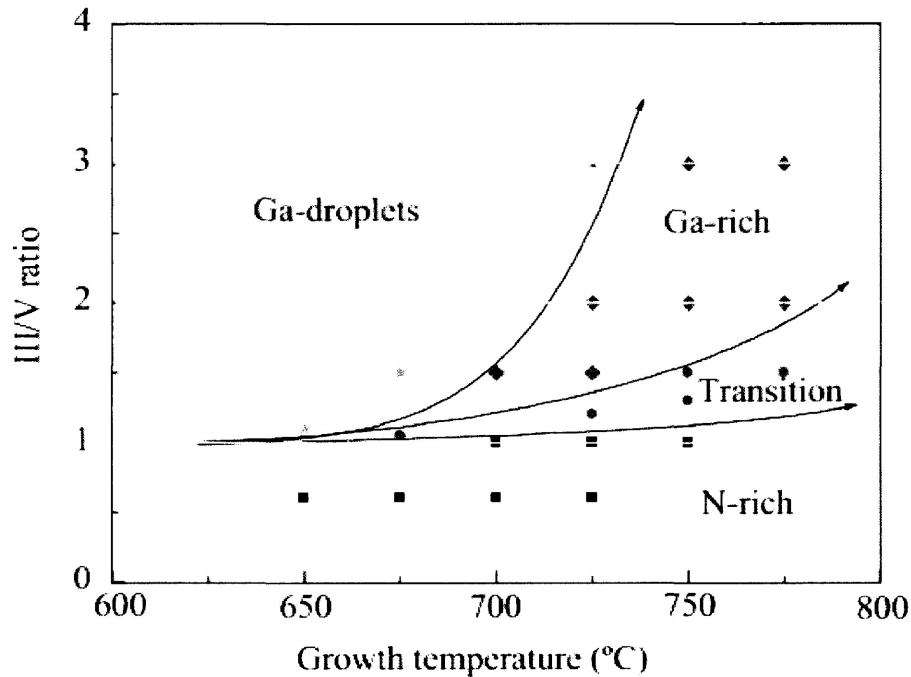


Figure 2.3: Surface phase diagram for plasma assisted MBE growth of GaN. Nitrogen flow was fixed and the gallium flux was varied. Depending on the growth temperature, III-V ratio mismatches can result in either nitrogen rich, gallium rich, balanced (transition region) or gallium droplet conditions.

## 2.2 GaN - Sapphire Buffer Layers

The issue of threading dislocations is considerable for GaN, and it is summarized well in [28]:

“Since there is no GaN bulk single crystal commercially available, all technological development of GaN-based devices relies on heteroepitaxy<sup>2</sup>. Most of the current device structures are grown on sapphire or 6H-SiC. However, since their lattice parameters

<sup>2</sup>The growth of GaN on a foreign material

and thermal expansion coefficients are not well-matched to GaN, the epitaxial growth generates huge densities of defects, with threading dislocations (TDs) being the most prevalent ( $10^9 - 10^{11} \text{ cm}^{-3}$ ). As a comparison, homoepitaxially grown GaAs exhibits  $\sim 10^2 - 10^4$  dislocations  $\text{ cm}^{-3}$ , and homoepitaxial Si almost 0. Actually this large density of TDs in GaN drastically limits the performance and operating lifetime of nitride-based devices. Therefore, there is currently a tremendous technological effort to reduce these defects.”

Since these statements were made, there has been some progress in the development of bulk GaN for homoepitaxy. These templates are available, although their cost is high and their quality still needs improvement. To that end, the situation of heteroepitaxy of GaN on a substrate is equally valid today. As a result of the lattice constant mismatch, certain atoms at the GaN-sapphire interface have no bonds and others are strained as shown in Figure 2.4. This strain and the associated dislocations produce non-radiative energy levels and deep levels with optical interactions at unintended wavelengths. By adding an additional large buffer layer on top of the seed layer as in Figure 2.1, these dislocations are reduced.

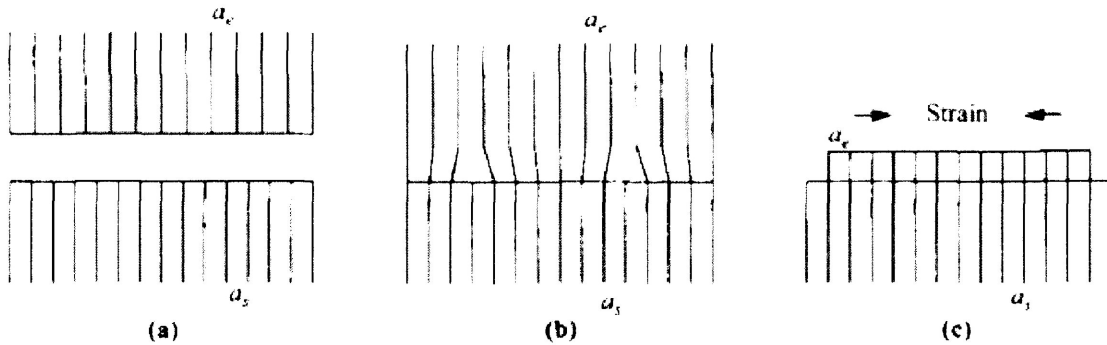


Figure 2.4: A depiction of an epitaxial layer atop a substrate, both with different lattice constants,  $a_e$  and  $a_s$  respectively. a) before interlacing occurs, they maintain expected lattice spacing. b) after interlacing, dislocations become present. c) In between dislocations, the atoms of one of the epitaxial layer strains to match that of the substrate, with the outer atoms experiencing more strain. Figure taken from [27].

The buffer layer is grown at as high a temperature as desired. Since the purpose is to distance the surface from the GaN-sapphire interface, the best stoichiometric ratio would produce fewer defects in the material. The further the separation between the film surface and the interface layer, the dislocation density decreases more so. As shown in Figure 2.5, the defect density decreases from  $\sim 10^{10}cm^{-3}$  to  $\sim 10^8cm^{-3}$  as the buffer layer thickness increases to  $3\mu m$ . Therefore, buffer layers of this large thickness are used to provide the best surface for subsequent GaN growth.

The dislocation density can be greatly decreased further by the use of a dielectric mask. By applying strips, or a grid, of silicon dioxide ( $SiO_2$ ), threading dislocations do not propagate through the dielectric (Figure 2.6). When growth occurs in the windows between the dielectric, 3-dimensional islands form, expanding laterally over the silicon dioxide. As a result, the GaN that overgrows the strips do not have threading dislocations stemming from the interface. This advancement, called Lateral Epitaxial Overgrowth (LEO), decreased the defect density to  $\sim$

$10^6 \text{cm}^{-3}$  [28]. As a result, commercialization of GaN laser diodes (LD) was hastened. Previously, LD lifetimes were only 300 hours on account of the dislocation density [30], and with LEO, devices now last more than 10 000h [28]. This advancement, while pivotal for LDs, is not as beneficial for LEDs. Lifetimes of LEDs can already exceed 100 000h, or eleven years of continuous use [30], so extra usage is not a high priority for LED device development.

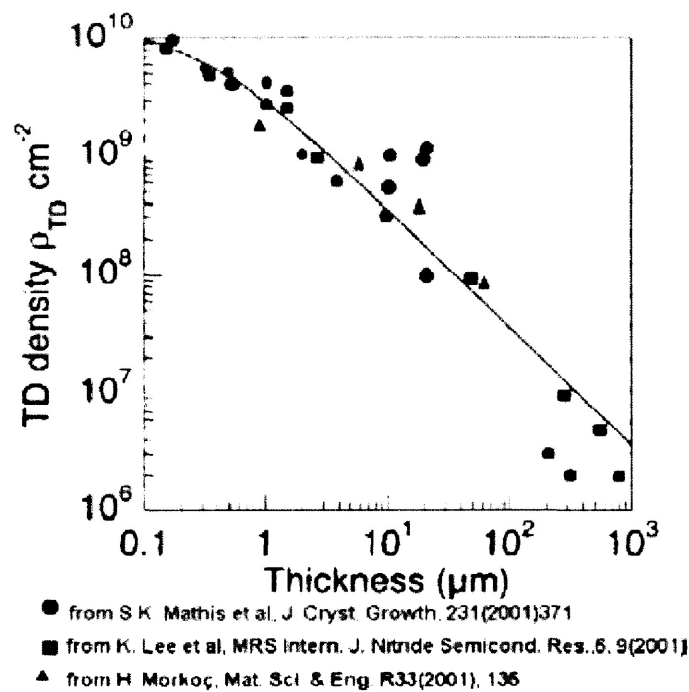
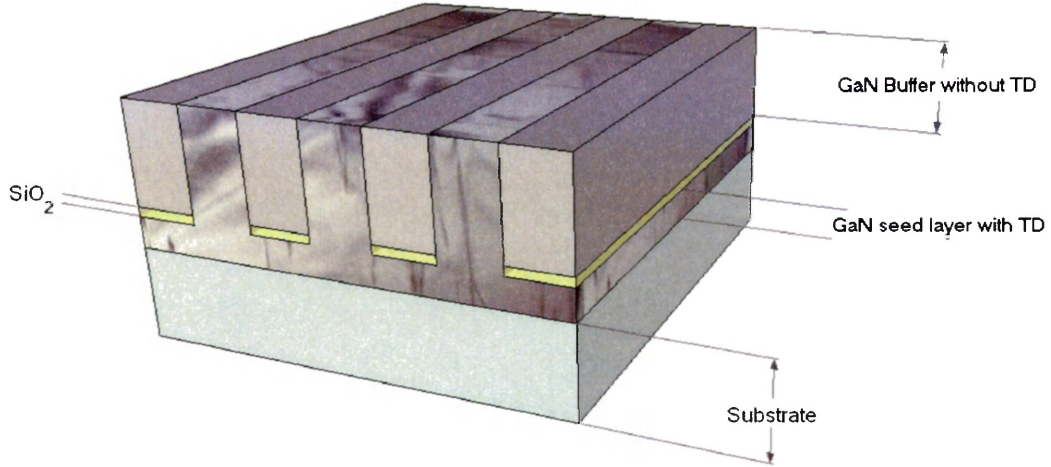


Figure 2.5: A summary of research into the dislocation density as a function of buffer layer thickness. Plot taken from [28].



*Figure 2.6: The principle of the Lateral Epitaxial Overgrowth method. The application of a dielectric mask decreases the threading dislocations in the mask overgrowth by preventing threading dislocations from protruding farther into the film.*

## 2.3 Impurity Doping and Carrier Concentration of Gallium Nitride

Engineering the carrier concentration during growth has been notably difficult for gallium nitride. The inherent background concentration of undoped GaN has been published to be of the order of  $10^{16} \text{cm}^{-3}$  [14], and higher values of  $\sim 10^{17} \text{cm}^{-3}$  are not unusual [2]. This implies that acceptor impurity doping to obtain p-type conductivity must first combat the background electron concentration before a surplus of holes is generated. This is especially problematic when considering the limits of acceptor doping (self compensation, solubility and activation) described earlier; there is only so much doping that can be done to counteract the background electron concentration. In this section, the background electron concentration will be investigated, and then following, a discussion of acceptor doping is detailed.

### 2.3.1 Background Electron Concentration

In the introduction to this chapter, it was conveyed that threading dislocations may be responsible for the background electron concentration, with only a small suggestion of the possibility of

other sources. In fact, this is a contentious issue with strong evidence that counters this theory. In this section, these alternate possibilities are discussed.

The motivation for investigating nitrogen vacancies due to threading dislocations was well justified. At first, other unintentional impurity concentrations were measured to be a few orders of magnitude smaller than the observed background electron concentration, and the dissociation of nitrogen required a low potential energy of around  $75\text{meV}$  [33], indicating its ready formation. It was also calculated that four gallium atoms surrounding a nitrogen vacancy form an interband resonating energy state, allowing an electron to jump to the conduction band, and parts of the model were confirmed experimentally by pressure induced carrier freeze out methods [31]. Coupled with arguments above, the thought of nitrogen vacancies being the predominant cause of the background electron concentration for GaN was commonplace.

This model, however, faced contention by *ab initio* calculations performed by Van de Walle and Neugebauer [32]. The results indicated that the formation energy of the nitrogen vacancy defect was not favourable when the Fermi level rests near the bottom of the conduction band (the formation energy,  $E_F$ , was  $3.0\text{eV}$ ). Accordingly, since unintentionally doped GaN has a high background electron concentration and thus its Fermi level lies proximal to the conduction band, nitrogen vacancies could not be the cause of the electron density. Rather, it was suggested that oxygen is a likely candidate for the background electron concentration. The proposed mechanism was by bonding to gallium vacancies ( $V_{Ga}$ ). Since gallium vacancies have a more accessible formation energy near the conduction band ( $1.8\text{eV}$ ), and since an oxygen atom bound to  $V_{Ga}$  has similar energy requirements, a shallow donor energy level can be formed [32].

There is a possible indicator for the presence of gallium vacancies, thus lending confirmation to the oxygen donor model as discussed by Van de Walle and Neugebauer [32]. The  $V_{Ga} - O$  complex has a deep level energy state of  $1.1\text{eV}$  above the valence band. If a photoelectric transition occurred between this level and the conduction band, it would produce photons with energies of about  $2.3\text{eV}$ , and its yellow light would be apparent. This yellow light is characteristic of a well

observed “yellow band defect.” Yellow emission has been observed in numerous samples whose bandgap is not associated with this energy level, and its appearance has many suggested origins. Since, however, positron annihilation experiments showed the correlation between yellow intensity, gallium vacancies, and oxygen, there is evidence of the relation between the yellow band and oxygen present in the sample [32]. Finally, this oxygen donor model was experimentally verified in silicon doped n-GaN, where the additional oxygen levels measured by secondary ion mass spectrometry<sup>3</sup> account for the electrons not donated by silicon [2]. With these two experiments, among others, oxygen contamination is now the leading theory for the high background electron concentration in GaN.

The implications of this analysis for p-GaN grown by MEAgrow is twofold. First, it is beneficial for LED radiation that the background electron concentration is not completely due to nitrogen vacancies. The strain and formation energy of these vacancies may produce non-radiative energy levels as described above, and thus the performance of an LED would be worse. Secondly, it is good to know the effect of oxygen when creating a model for analysis. All films grown will contain this background impurity, which may act as a compensator for p-type films; the presence of these minority carriers could cancel out the effect of majority ones when in close proximity. Therefore, by understanding its concentration and activation energy, it will be easier to interpret the characterization efforts of this thesis.

### 2.3.2 Acceptor Doping in GaN

Historically, the background n-type concentration was only a concern in the early development of p-type GaN. The inability to activate the acceptor impurities soon became a bigger issue; the amount of acceptors did not correspond to the amount of holes. It was hypothesized and proven that magnesium formed bonds with hydrogen and did not insert itself in the gallium lattice position, thus inactivating the atom as a dopant [14]. In response, other impurity atoms were tried, like beryllium whose enthalpy of formation in a  $Be - N$  binding complex -

---

<sup>3</sup>Mass spectrometry measured off ejected ions from an incident beam that ‘drills’ the surface

and thus its solubility - is more favourable than that of magnesium ( $-6.11eV$  for Mg versus  $-4.8eV$  for Be) [32]. Further, its activation energy ( $170meV$ ) is reported to be slightly lower than magnesium's, stated with caution due to the large range of reported values for magnesium [32]. However, the atomic radius of beryllium is too small, increasing the strain in the lattice and forming compensating mechanisms in interstitial spaces. Thus, its formation energy when actually inserted into the lattice is on the order of magnesium's, depending on the stoichiometry [34]. Other atoms were tested like zinc, mercury, carbon etc. Zinc doped materials were highly resistive and provided a dominant  $0.5eV$  band transition, mercury provided an undesired red shift<sup>4</sup> and carbon peculiarly decreased conductivity by providing a deep level donor [34]. Hence, the issue of magnesium inactivation had to be resolved.

The first successful attempt at reactivating the  $Mg - H$  complexes was with low energy electron beam irradiation (LEEBI) [35]. The resulting material displayed remarkably lower resistivity, higher mobility and a hole concentration around  $2 \times 10^{16} cm^{-3}$ . However, the activation ratio - the number of active acceptors relative to the impurity concentration - was a mere  $2 \times 10^{-4}$  [14], and Nakamura *et al.* [36] later discovered it increases with a more suitable template, namely one with a GaN seed. The resulting material produced a concentration of  $3 \times 10^{18}$  holes  $cm^{-3}$ . Perhaps, the fewer dislocations in the p-GaN epilayer removed a limit in this procedure. Nakamura then went on to show that LEEBI serves only to heat the material to remove the hydrogen complex [14]. By annealing at  $700^{\circ}C$  post growth in the presence of  $N_2$  gas, the resistivity of p-GaN could be dropped to an impressive  $0.2\Omega \cdot cm$  from  $320\Omega \cdot cm$ , and the effect is reversible if the anneal happens with  $H_2$  in the ambient. It is no surprise, then, that many research groups employ this annealing method during p-GaN growth ([16, 2, 37, 38, 39] with many others).

Additional experiments with more controls worked to further prove the  $Mg - H$  model. Miyachi *et al.* [40] created a GaN:Mg<sup>5</sup> on GaN:Si diode with metal surface coatings that presumably

---

<sup>4</sup>When the peak luminosity wavelength becomes longer

<sup>5</sup>The notation GaN:Mg means GaN doped with magnesium

trapped hydrogen within. One would think that the magnesium would be forced to bind with neighbouring hydrogen. However, p-type conductivity could still be obtained if a sufficient bias was applied during the anneal [14]. Hydrogen would dissociate into  $H^+$  ions when hot and recombine with passing electrons from the current leads, producing inert  $H_2$ . From these interpretations, the motivation for thermal annealing in this thesis is well understood and well justified.

When magnesium has been activated by an annealing process, however, very few atoms actually accept electrons to form holes. The magnesium acceptor level is not a shallow one that is easily thermally activated; at room temperature, there is insufficient thermal energy to activate all the Mg. Hence, magnesium doped GaN carrying background oxygen donors could be completely compensated by electrons. Not all magnesium atoms are inactivated acceptors, however. The kinetic energy of the material has a distribution (a Boltzmann distribution), whose average equals<sup>6</sup>  $\langle E \rangle = f \cdot \frac{1}{2}k_bT$ . Hence, the number of acceptors producing holes becomes

$$\frac{p}{N_a} = \exp\left(-\frac{E_a}{k_bT}\right) \quad (2.1)$$

where  $E_a$  is the activation energy of magnesium as an acceptor,  $p$  is the hole concentration and  $N_a$  is the acceptor concentration. Considering the  $\sim 5 \times 10^{19}cm^{-3}$  solubility limit for magnesium indicated in the previous chapter, room temperature would activate  $\sim 10^{17}cm^{-3}$  atoms, or 0.3%.

This limit can be pushed further. By employing a technique called metal modulation epitaxy (MME), it has been shown that magnesium's solubility, or more accurately, its incorporation in the lattice increases. Hence, exceptionally high hole concentrations over  $10^{19}cm^{-3}$  have been achieved [41]. The technique works by sequencing between gallium rich and nitrogen rich flows. Under nitrogen rich conditions only, magnesium easily substitutes itself with a gallium vacancy, however the flow of Ga causes the magnesium to be displaced to the surface. Under gallium rich conditions only, the magnesium indeed is absorbed, but tends to be localized in metallic regions,

---

<sup>6</sup> $f$  is the number of degrees of freedom

and not in the lattice. As a result, the collection of magnesium in unintended areas can cause polarity inversion domains that trap potential holes (N-rich), or simply do not accept electrons (Ga-rich) [41]. By alternating between N-rich and Ga-rich conditions, there are periods of gallium flow that allow the metal to better incorporate itself in the lattice, and also times of nitrogen flow with magnesium to capitalize on improved solubility. With better atomic incorporation, growths can have a p-type carrier concentration of  $1.5 \times 10^{19} \text{cm}^{-3}$  [41].

The increase in magnesium solubility resulting from MME, while impressive, does not increase p-type conductivity as much as having an acceptor with a small activation energy. Due to the exponential relation of the Boltzmann distribution (equation 2.1), a drop in the activation energy can produce a large number of holes. It has been reported, to a small extent, that such change can be obtained if a small amount of codoping is present. With the right proportions of oxygen and magnesium being introduced into the reaction chamber, almost an order of magnitude increase in hole concentration can be obtained [42]; during that experiment, the increase was from  $2 \times 10^{17} \text{cm}^{-3}$  to  $(0.8 \rightarrow 2.0) \times 10^{18} \text{cm}^{-3}$  with the addition of oxygen. Further, the activation energy was shown to drop from  $170 \text{meV}$  in unintentionally compensated GaN:MG to  $135 \text{meV}$  with oxygen. By performing the Hall experiment over a wide range of temperatures, this group determined the necessary thermal energy to activate each impurity. By noting abrupt changes in the measured carrier concentration at certain temperatures, one can obtain this activation energy. For the growths performed in this thesis, it is possible that ambient oxygen compensation could increase p-type conductivity.

## 2.4 Growth Technology

The different growth technologies (CVD, MBE, plasma assisted, etc.) each experience the above phenomena differently. For instance, in MBE, there is often no need for thermal activation of the  $Mg - H$  complexes because the atomic beam effluxes do not contain hydrogen based precursor molecules, and its ultra high vacuum of  $10^{-10} \text{Torr}$  does not contain significant ambient amounts. Hence, a review of experiments presented in the literature must take into account the

technology used. Additionally, different growth methods yield different quality of materials. For example, CVD architectures produce films with more dislocations since they are grown at a higher temperature. The  $1000^{\circ}\text{C}+$  temperature used to dissociate nitrogen from ammonia in CVD causes a thermal mismatch in the film when cooling, ruining the lattice structure. Naturally, then, it is warranted to investigate the advantages of each method to determine in what ways MEAglow compares. It is interesting to note the prevalence of CVD reactor systems. Commercial samples used for comparisons in this thesis used CVD methods due to their standardized recipes optimized years ago.

#### 2.4.1 Chemical Vapour Deposition (CVD)

The term chemical vapour deposition is an umbrella label for growths using vapour flow toward the substrate, but the most common type is metal organic chemical vapour deposition (MOCVD). Since gallium and magnesium are metals, and since they are reactive in air by themselves, they must be transported in a stable vapour form. Trimethylgallium,  $((\text{CH}_3)_3\text{Ga})$ , is the molecule of choice for gallium and biscyclopentadienyl-magnesium ( $\text{CP}_2\text{Mg}$ ) is the magnesium precursor. Since the organics will dissociate to form the metals at a low temperature, Ga and Mg can easily be deposited on the semiconductor surface. In MOCVD, the nitrogen precursor molecule is ammonia,  $(\text{NH}_3)$ . Its use requires high temperatures around  $1000^{\circ}\text{C}$  to dissociate the nitrogen from the molecule. In addition to causing thermal mismatch issues and being too hot for InGaN fabrication, the substrate obtains a contour called “bowing,” which pulls on the GaN when cooling returns it to a planar state. Hence, either the dislocation density will be increased, or the substrate will be permanently bowed, or a combination of the two.

Another form of CVD exists that is closely synonymous to MOCVD. Called Hydride Vapour Phase Epitaxy (HVPE), ammonia is still used as the nitrogen precursor molecule. However, different vapour chemicals are used for gallium and magnesium. The precursor molecule for these are halides, like  $\text{GaCl}_3$ , and the technique has been shown to have high growth rates between  $70 \rightarrow 90\mu\text{m}/\text{h}$  [43]. Since ammonia is still used, however, the growth temperature is

generally too high for the purposes of InGaN based LEDs.

#### 2.4.2 Plasma Based Growth

Using nitrogen plasma is a way to introduce active nitrogen species to the semiconductor surface at temperatures more conducive for indium preservation. The electrons in the atom are excited to an elevated energy level, and the added potential energy is used in the formation reaction. Therefore, the thermal energy required for chemical reactions is not needed and as a result, subsequent deposition on top of the InGaN does not result in much indium desorption or decomposition. Plasma based growth is a niche solution for certain applications. GaN templates grown on sapphire use ammonia based CVD because of the higher growth rate and better stoichiometric ratios, even if issues of lattice dislocations are more prevalent. Nitrogen plasma has, however, found its use in the MBE growth of GaN and in the fabrication of indium nitride and indium gallium nitride materials. Due to the low reaction chamber pressures used in ammonia based MBE, temperatures must be sufficiently low to prevent GaN desorption. Further, the low temperature used in plasma systems preserve indium content regardless of whether vapour deposition or molecular beams are used. To this end, architectures like plasma assisted MBE and plasma assisted CVD are becoming common in the literature.

Nitrogen plasma is an effective way to incorporate active nitrogen species into the film. The minimum excited energy level of  $N_2^*$  is 6.11eV as shown in Figure 2.7, and the  $2Ga + N_2^* \leftrightarrow 2GaN$  reaction proceeds spontaneously on account of its negative Gibbs free energy [44]. Since this energy is greater than most formation enthalpies of concern, nitrogen plasmas are a viable alternative to ammonia for GaN growth. In addition to the lower fabrication temperatures, plasma generated species have the benefit of arriving at the substrate in the desired molecular or atomic form. From Figure 2.7, both molecular and atomic nitrogen are produced from the plasma source, where the lifetime of the higher energetic atomic nitrogen is shorter. If the plasma source is placed sufficiently far from the substrate (as is done in remote plasma enhanced CVD), or if

---

<sup>7\*</sup> means energized plasma

the nitrogen pressure is high enough to introduce energy dispelling collisions, only the molecular species is present. If atomic nitrogen is desired, more than enough energy is imparted to the gas and molecular nitrogen dissociates into atomic nitrogen. If the plasma is energized to the point of becoming ionic, the particles can be deflected away from the sample using electric fields, reducing some of the damage inherent in its kinetic energy. Therefore, depending on the chemical reaction desired at the surface, either species can be obtained.

The preferred species of nitrogen for film growth is still debated. There is a view that atomic nitrogen is preferred because the reaction pathways are more favourable. The reaction pathway,  $Ga + N \leftrightarrow GaN$  does not require the decomposition of molecular nitrogen, thus the reaction should progress at a higher rate. On the other hand, atomic nitrogen has been shown to cause damaging interactions with the semiconductor surface, removing elements from the lattice. For instance, the temperature at which atomic desorption in MBE begins has been shown to occur earlier when using atomic nitrogen as opposed to molecular nitrogen ( $650^{\circ}C$  versus  $720^{\circ}C$ )<sup>8</sup> as seen in Figure 2.8 [45]. One possible explanation is that the atomic nitrogen attempts to form a molecular bond with the nitrogen in the semiconductor lattice, and is lost as a volatile molecule, while the gallium is thermally desorbed [26]. Therefore, the growth conditions used must be taken into consideration when choosing the plasma source type.

---

<sup>8</sup>Depending on the polarity of the film - in the *Ga* (Ga-face) or *N* direction (N-face). For example, in *N*-faced materials, gallium has a higher affinity to the surface and thus desorption requires even higher temperatures.

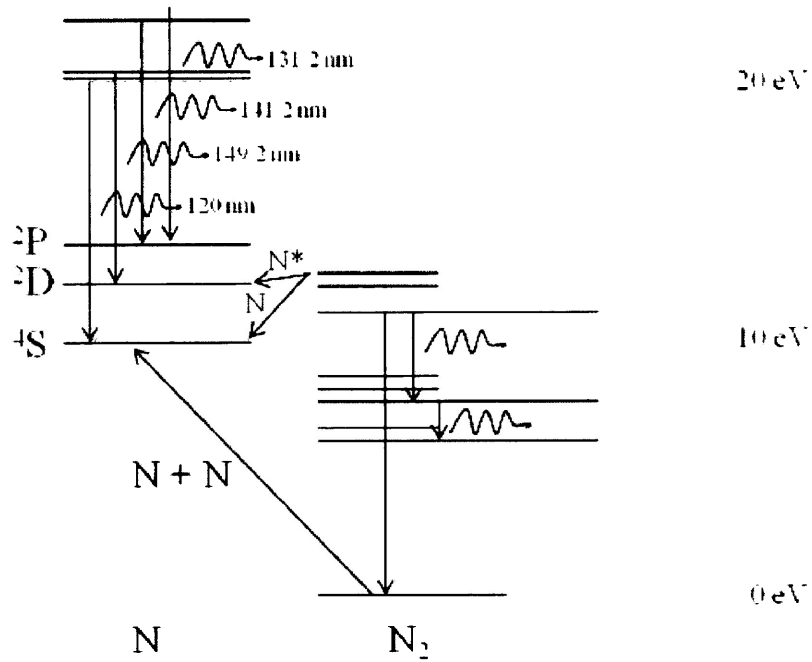


Figure 2.7: The excited energy states of nitrogen. As the energy levels increase, molecular nitrogen dissociates into atomic nitrogen.

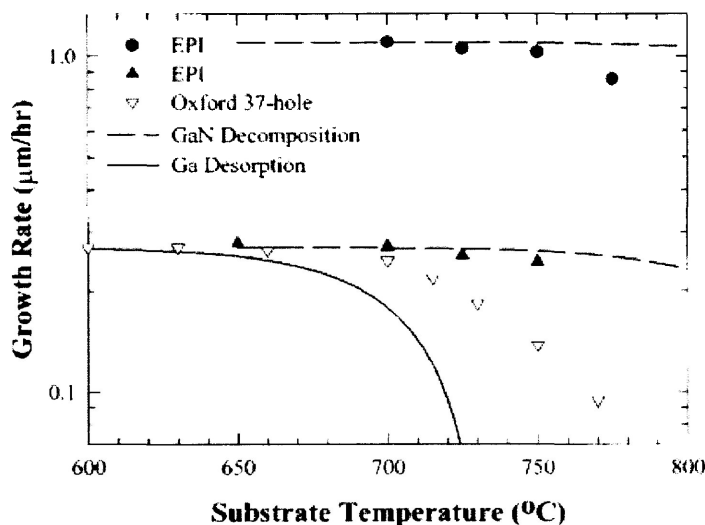


Figure 2.8: The growth rates of GaN in plasma assisted MBE. Two different plasma sources were used. The Oxford 37-hole source tended to produce mainly atomic nitrogen, whereas the EPI source produced mostly molecular nitrogen.  $\blacktriangle$  symbols represent measurements when the growth rate was set low, while  $\bullet$  symbols are when it was set high. Overlaid on the data are predicted desorption rates of gallium desorption (solid line), or GaN desorption (dashed line), depending on whether an overpressure of Ga flow limits its desorption. Picture taken from [45].

### 2.4.3 Molecular Beam Epitaxy (MBE)

MBE is a technique that delivers the required atoms in a beam toward the substrate (see Figure 2.9). Since the pressure of the reaction chamber is very low ( $< 10^{-4}$  Torr), the group-III atoms have no particles to react with until they reach the substrate. Hence, the use of precursor molecules (metalorganics or halides) is not necessary and the metal atomic species are thus stored in effusion cells; by adjusting the temperature and geometry of the cells, the flow rate and beam trajectory can be dictated.

MBE was not prevalent in the development of GaN until the late 1990s [14]. The combination of high temperatures required when using ammonia and ultrahigh vacuums was problematic. In such an environment, gallium and nitrogen would desorb from the lattice at  $> 730^{\circ}\text{C}$  [45]. In this

referenced study, this process could be countered to a small degree by using an over pressure of gallium, increasing the dissociation temperature to  $800^{\circ}\text{C}$ , but is still insufficient for the effective use of ammonia. Nitrogen plasma assisted MBE is used to combat the desorption. The ability to use lower temperatures with these sources promotes GaN formation rather than desorption. Since this hurdle has been overcome, MBE systems can grow high quality and complex films, using effusion cell shuttering to employ MME and to create abrupt heterojunctions [16, 46]. These systems are also quite pure. Since only atomic elements are delivered, and since growth occurs in ultra high vacuums, there are fewer unwanted impurities like hydrogen. Therefore, better semiconductors are produced, and problems like Mg-H passivation are not present. Since the semiconductors grown in the MEAglow system are also produced in a vacuum environment, this suggests that higher temperatures should be avoided in that case too.

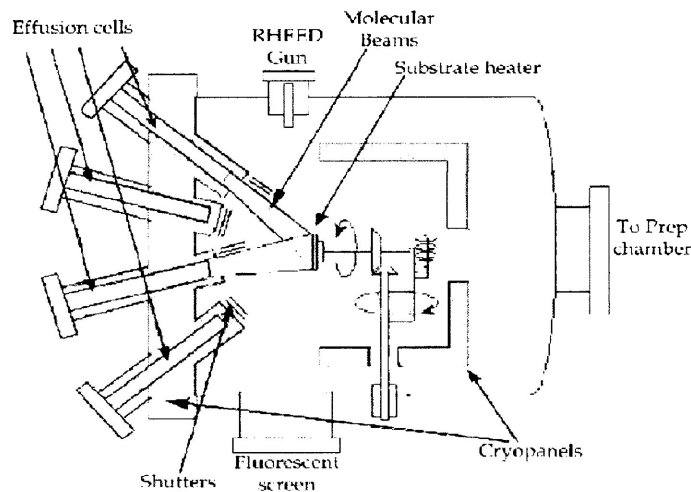


*Figure 2.9: The makeup of an MBE system. Effusion cells emit beams of atoms toward the surface of the substrate where upon contact they form the GaN lattice. Picture taken from [47]*

#### 2.4.4 Migration Enhanced Afterglow (MEAglow)

The plasma can be initiated through many means. Three examples of plasma inducing hardware include capacitively coupled systems, inductive coupling through solenoids and microwave

cavities (Figure 2.10), each of which have their own effect on semiconductor growth. Capacitive systems accelerate atoms from one plate to the other, and the resulting electric potential is transformed into kinetic energy. Although not all the energy is transformed, the high kinetic energy particle collisions with the semiconductor can destroy the surface. Inductively coupled systems use solenoids wrapped around the plasma line to impart electromagnetic energy. Their main advantage is their high plasma density ( $10^{12}cm^{-3}$  versus  $10^{10}cm^{-3}$  for capacitive sources). Microwave cavities influence the nitrogen gas as it passes through an anti-node of the electric standing wave. However, cavities and solenoids have an inherent problem to their design in that oxygen contamination on dielectric component walls can be problematic [17].

In addition to being free of these parasitics, the plasma source used in Migration Enhanced Afterglow (MEAglow) is more favourable to being adopted in commercial manufacturing because of the wide area films it can produce. MEAglow is the term given to a technique that utilizes a hollow cathode plasma source for film deposition (Figure 2.11). The walls of the bores are driven with RF voltage at 13.56MHz, and the plasma itself becomes the RF anode at steady state. With the presence of both a cathode and anode, RF energy can be imparted with three major benefits. Firstly, nitrogen can be delivered to a wider surface area. Since all bore walls are connected to the same potential, it does not matter how many holes or how large the source is. Hence, it can be envisioned that this source can produce 4, 8 or 12 inch wafers, or even larger. This is especially advantageous when compared to MBE based nitride film growth. The effusion cells that deliver atomic species act like point sources, and so the centre of the films receives the most gallium, magnesium, nitrogen etc. As a result, the film's thickness is very inhomogeneous. The second advantage of the hollow cathode source is its plasma density is still competitive compared to the other sources. By energizing the nitrogen to be saturated with ions, the gas is highly conductive and the characteristics can be measured using a Langmuir probe (Figure 2.12). By placing the probe in a conservatively faint plasma location within the hollow cathode, its current-voltage characteristics were mapped to a plasma density of  $n_e = 9 \times 10^{11}cm^{-3}$  by

using the relation [17]:

$$I_{sat} = A \cdot \exp\left(-\frac{1}{2}\right) q \cdot n_e \sqrt{\frac{qT_e}{M}} \quad (2.2)$$

where  $A$  is the area of the probes,  $q$  is the elementary charge,  $M$  is the nitrogen's mass, and  $T_e$  is the electron temperature. The last advantage is that molecular species is almost entirely present. The hollow cathode is placed far from the substrate, and the plasma pressure is high enough to dispel atomic nitrogen energy through particle collisions. Therefore, depending on one's standpoint regarding the optimal plasma species, MEAglow systems can offer a greater potential impact in the manufacturing of low temperature GaN.

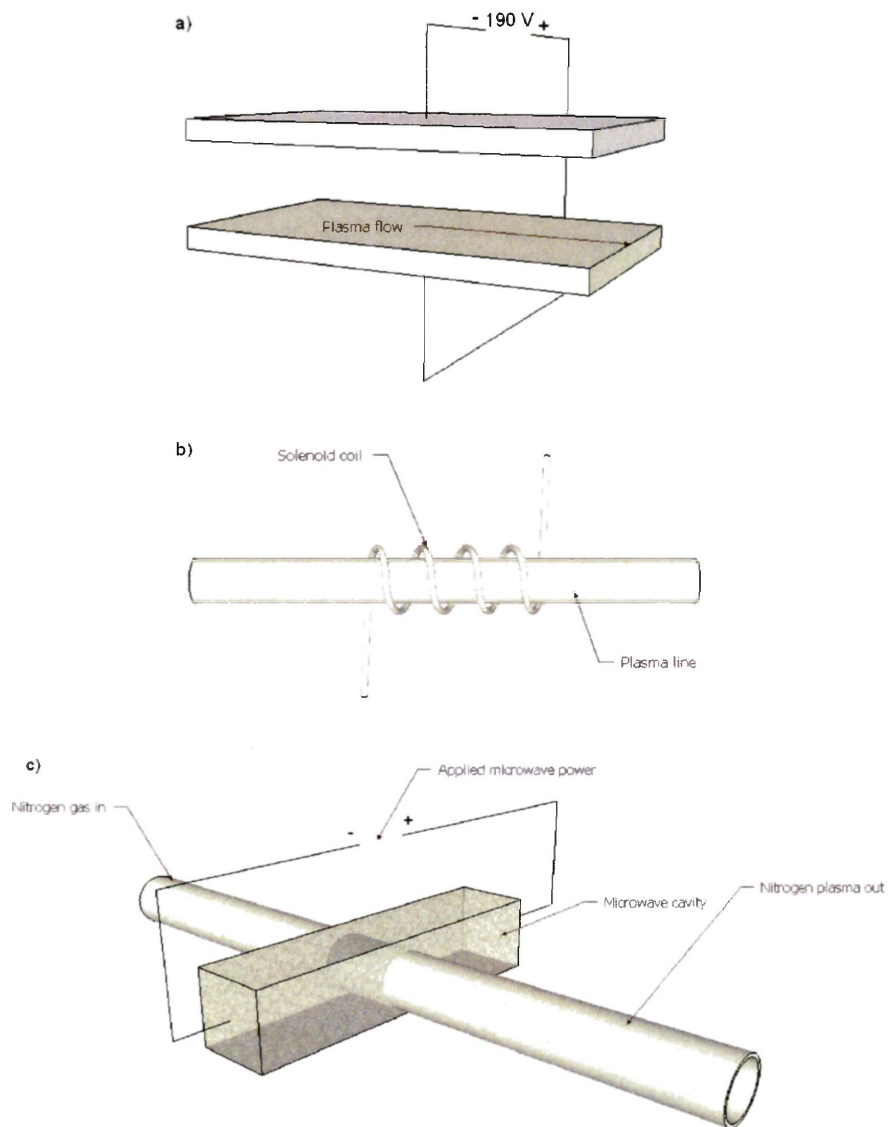
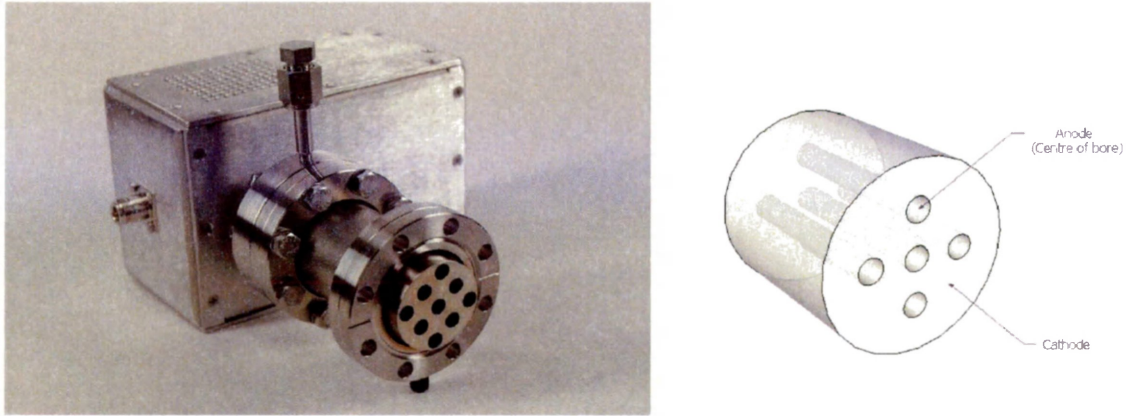


Figure 2.10: Three architectures of plasma sources. a) Capacitive, b) Inductive, c) Microwave



*Figure 2.11: The hollow cathode source*



*Figure 2.12: An example of a Langmuir probe to measure ion density*

## 2.5 LED Structures

As introduced in Chapter 1, high brightness LEDs most often follow a quantum well (QW) configuration as shown in Figure 2.1. The ability to trap charge, preventing it from escaping the LED structure is so beneficial that very seldom would a commercial device neglect it. There are many growth characteristics to consider that potentially affect the quality of the quantum well. For example, if growth is dominated by 3-dimensional islands, there will be no smooth layers for the well to be formed. Hence, proper nucleation and growth conditions will facilitate the well formation. Next, the wrong stoichiometry can produce metal droplets. Since Ga metal is a liquid at near room temperature, the integrity of the semiconductor around the droplets is compromised. Lastly, the control of polarity has been shown to affect luminosity. Ga-face films tend to be smooth, with a surface roughness less than 1nm ([17]), allowing light to transmit from the active layer without scattering. However, the light transmission through smooth surfaces is

subject to total internal reflection so that some fraction does not emanate. N-face films, on the other hand, are rougher, allowing the light to pass regardless of the directional angle. These details, and more, are presented in this section to motivate the optimal LED.

### 2.5.1 Quantum Well LEDs

The structure of the QW LEDs previously introduced have a bit more complex of an arrangement than indicated, using an  $n - GaN / n - InGaN / p - AlGaN / p - GaN$  layered pattern shown in Figure 2.13a. The n-GaN and p-GaN form the p-n structure essential to feed charge carriers into the well. The low bandgap energy of the n-InGaN layer forms the base of the quantum well. Finally, the p-AlGaN layer is called an ‘electron blocking layer.’ If its large bandgap was not present, electrons would easily escape the well through the electrodes under forward bias and not perform light emitting carrier recombination. With this structure, carriers are trapped within the InGaN layer, producing light with up to 40 times the intensity under the same forward current [5]. To illustrate this effect, an energy band diagram of this configuration is shown in Figure 2.13b) and c). The band diagram reflects the Anderson model, and while this neglects important polarization effects in the semiconductors, it is advantageous to show how band offsets form the well in the InGaN layer.

The idea of using a quantum well can be extended further. By alternating layers of n-GaN and n-InGaN, many repeating wells are formed, creating a multi-quantum well (MQW) LED (Figure 2.14). Hence, any carriers that would not be confined by a single quantum well alone would likely be trapped by the other wells, increasing the luminosity further. Obviously, this concept cannot be extended infinitely for two reasons. First of all, it has been shown that additional luminosity benefits diminish after each additional well. In [48], an array of MQW LEDs was fabricated and it was discovered that the first quantum well produces 1.5 times the luminosity of the next three combined. Secondly, the thin potential barriers that result from trying to create too many wells are easy to tunnel through and create non-radiative energy states due to the strain of the  $GaN - InGaN$  interfaces. So while creating a fine structure of repeating layers is beneficial, a

single quantum well (SQW) LED may still provide adequate illumination.

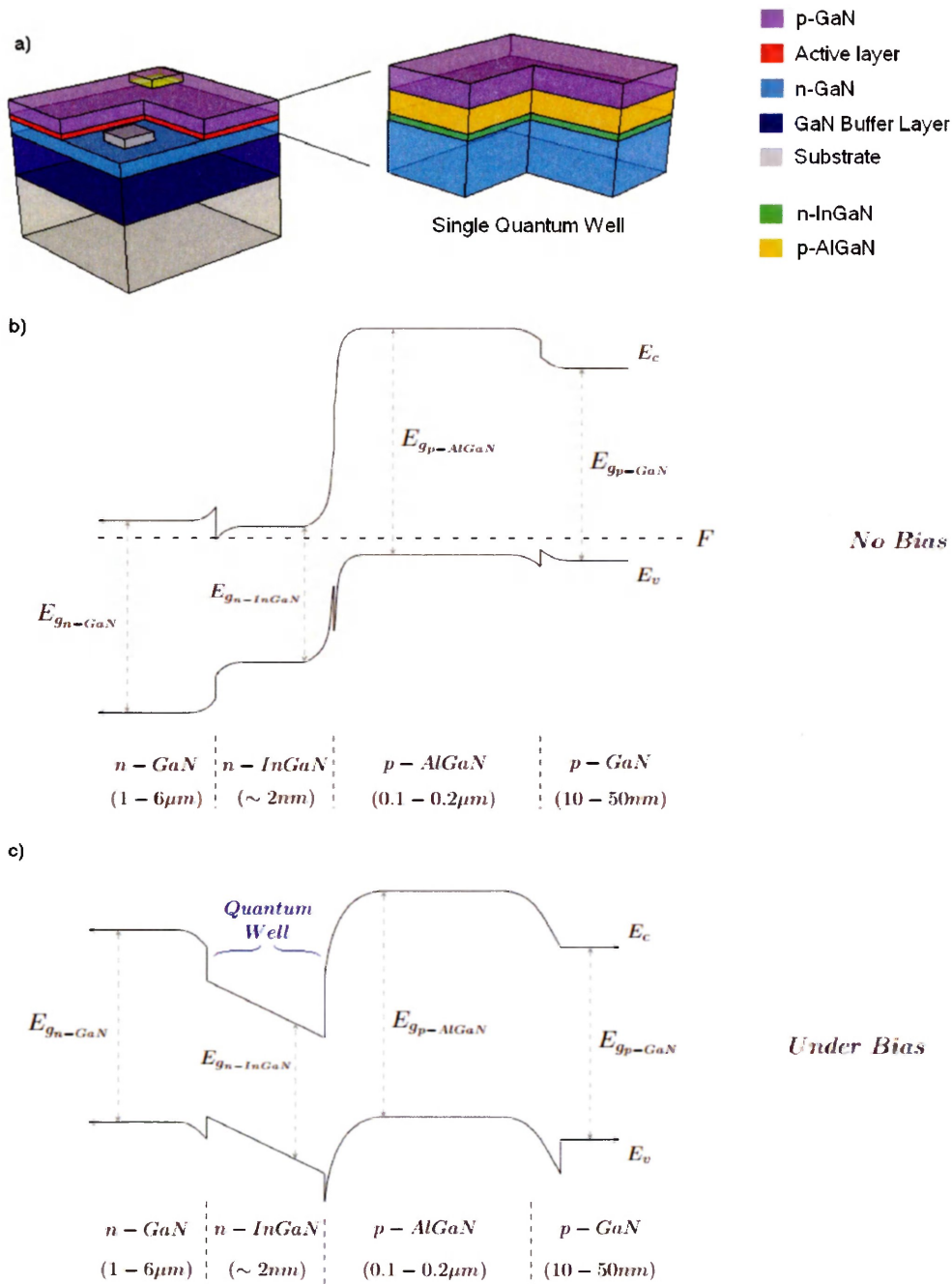
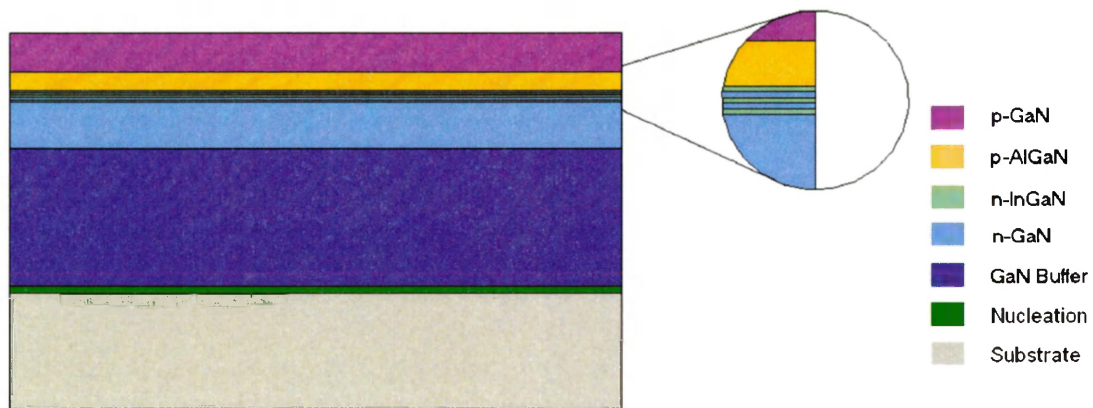


Figure 2.13: The single quantum well and it's a) physical structure, b) band diagram, and c) band diagram under forward bias. Band structure reflects the Anderson model to demonstrate the offsets between each material. Material thicknesses were obtained from reports in [14] for the leftmost three materials, and the p-GaN thickness is derived from observation in the lab.



*Figure 2.14: The Multi Quantum Well structure (MQW). Here, any carriers that would not be trapped within a single quantum well would likely be confined by the other wells.*

### 2.5.2 LED Packaging

This QW structure can be fabricated into a device using the Mesa configuration described in the previous chapter. Exposed pads will reveal the film, allowing for the forward current to be applied. However, when light is produced from the film, it can emit in all directions. Since LEDs are often directional devices, there must be a mechanical solution to use all the light, especially if viewed from one side only. By attaching the LED to a flip chip package (Figure 2.15), a reflector back plane ensures the light exits in one semi plane. Further, by flipping the LED upside down, contacts can be formed without leads blocking the light. Hence, this packaging is an effective commercial solution. LED packaging solutions can also be used for novel applications. By removing the film from the sapphire substrate using an excimer laser, the LED can be used in small form factor displays like liquid crystal display backlighting [49]. With these innovations, full colour displays have become commonplace in hand held devices, among other uses.

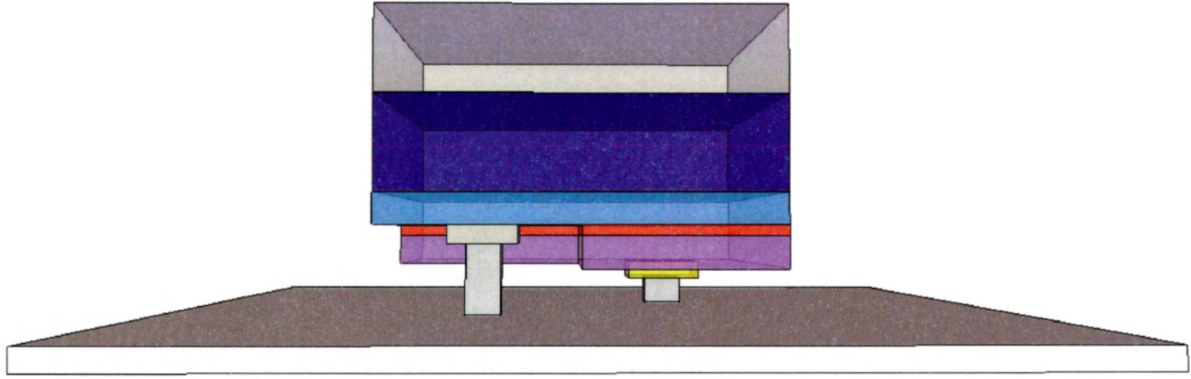


*Figure 2.15: The flip chip configuration. Here, light produced by the active layer reflects off the bottom plane, increasing the luminosity.*

## 2.6 Chapter Summary

Decades ago, two roadblocks, namely island growth and lattice dislocations, prevented the easy adoption of GaN fabrication into existing MBE and CVD technologies. These problems were reduced by introducing nucleation and buffer layers to allow higher quality film growth of the epilayer. Plasma based growth of these epilayers further assisted fabrication in MBE environments and in applications using GaN-InGaN quantum well LEDs by allowing the growth at low temperatures.

Growing p-GaN on top of InGaN at low temperatures preserves the integrity of underlying high indium content films. However, low temperatures will affect the sensitivity of metal deposits from a stoichiometry perspective.

Nitride semiconductor films grown using any architecture exhibit a background electron concentration due to the presence of oxygen during growth, which is an impediment to achieving p-type conductivity. Other challenges to obtaining a high density of holes is the inactivating Mg-H complex; high activation energy of Mg; Mg self compensation at high concentrations, and

Mg solubility limits. The MEAgrow technology was introduced and its benefits - film homogeneity; presence of only excited molecular nitrogen species, and high plasma density - were discussed to motivate its capabilities to produce high quality films. This is especially true for low temperature growth of GaN-InGaN LED structures that confine carriers to improve luminosity, where the p-GaN epilayer must not be grown at high temperatures that desorb or decompose the underlying InGaN.

## Chapter 3

# Feasibility and Characterization of Magnesium Doped GaN Fabrication

*“Measurement is the first thing that leads to control and eventually to improvement. If you can’t measure something, you can’t understand it. If you can’t understand it, you can’t control it. If you can’t control it, you can’t improve it.”*

(H. James Harrington)

The motivation of this study is clear: demonstrate the feasibility of p-type gallium nitride fabrication in the MEAgrow environment to realize the benefits this system has with respect to high indium content GaN-InGaN LEDs. One needs to ask, then, how its p-type conductivity will be confirmed. Further, it is important to see if there is a way to measure its hole concentration as a benchmark for future semiconductor development. To this end, this chapter focuses on methods to verify and characterize p-type GaN films.

Electrical measurement of GaN properties is notably difficult over more established semiconductors. Due to the wide bandgap, electrical measurements suffer from the problem of Schottky contacts. The Fermi level can be positioned anywhere within the  $3.4eV$  bandgap range, and potentially larger, which makes it difficult to find a metal whose work function is close to this level.

As a result, any mismatch can cause contacts to have a rectifying built in potential,  $V_{bi}$ , that skews any presumed relationship between current, voltage, and the parameter at hand. Therefore, one needs to know that the semiconductor’s characteristics are within a specific range to be confident the electrical probes are appropriate. Optical characterization is equally involved. Due to GaN’s direct bandgap, there are many sources of optical emission. Three notable ones are that from a  $3.4eV$  band to band (interband) transition; that from a magnesium to defect transition ( $2.8eV$ ), and that which causes the yellow defect described earlier in Section 2.3.1. Further, impurities like surface oxides and degenerate doping<sup>1</sup> create the phenomena of an Urbach tail and the Moss-Burstein effect respectively, grading the absorption edge of the photonic spectrum [50]. With these confounding effects, the semiconductor sample cannot simply be placed in an optical instrument and be scanned without consideration of the underlying mechanisms.

It is also ill advised to rely on one method of characterization. While it would be ideal to have an all encompassing test, the mechanisms behind the measurement can confound the result, rendering the insight inaccurate. For example, the published magnesium activation energy in GaN varies from  $150 \rightarrow 221meV$  depending on the measurement conditions and whether an electrical or optical measurement is used [14]. Therefore, this thesis will examine many methods of investigating the properties of p-type GaN for LED applications. The approach to do so will be a comparative one. Since this work is the first attempt to grow magnesium doped GaN at low temperatures in MEAglow systems, there is no direct reference for comparison. Therefore, the exploration will use measured characteristics of GaN grown by CVD as a theme for evaluation of GaN produced by MEAglow.

### 3.1 p-GaN Electroluminescence

There is one quick, definitive method to confirm p-type conductivity in a gallium nitride sample. When placed in proximity to a region of n-type GaN, passing current through this p-n

---

<sup>1</sup>So much doping that the Fermi level approaches the conduction band, filling all the lowest available energy states

junction should energize the three emissions sources described above. For carrier recombination in strongly p-type material, the most apparent one, to human eyes, is the blue (magnesium related) emission. If blue light is visible, activated magnesium is present, indicating p-type conductivity. Fortunately, the films need not be fabricated adjacent to an n-type GaN region. A thin n-type oxide readily forms on the surface of GaN due to its reactivity with air, especially when removing hot samples from the reaction chamber. Consequently, the electrodes need only be placed on the surface as in Figure 3.1. The blue light emitted is an important characteristic of p-GaN. Even though GaN has a bandgap whose energy emits UV light, it can be used for blue LEDs on account of the strength of the magnesium energy level transition. That is why this blue light is often present, even when observing other phenomena of the device (Figure 3.2, underneath the right electrode).

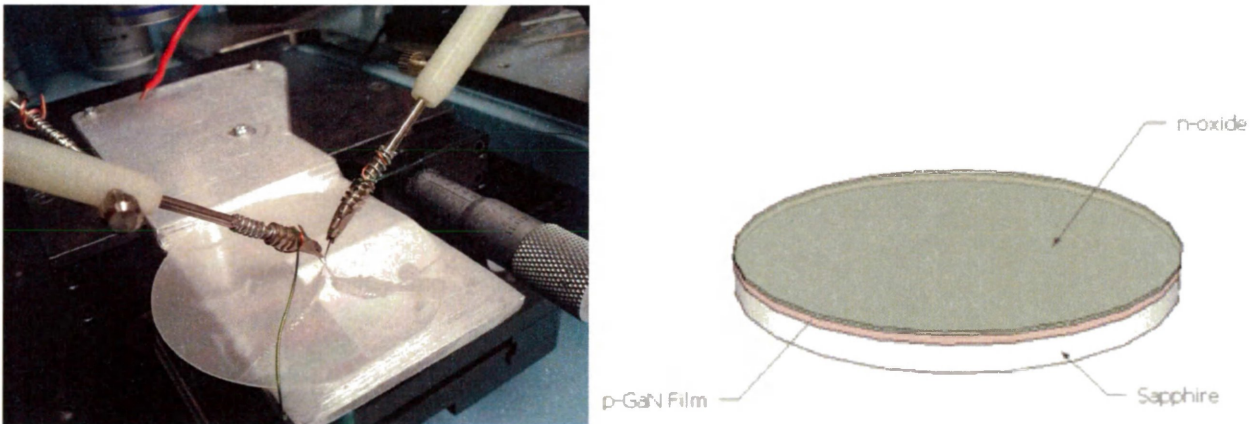


*Figure 3.1: Testing for p-type conductivity by probing the oxide of the GaN sample. Contacts are placed on the surface of the wafer, and thus are touching the n-type oxide. Since this outer layer is highly resistive, current will pass into the p-GaN film, creating the p-n junction regardless of the polarity of current.*

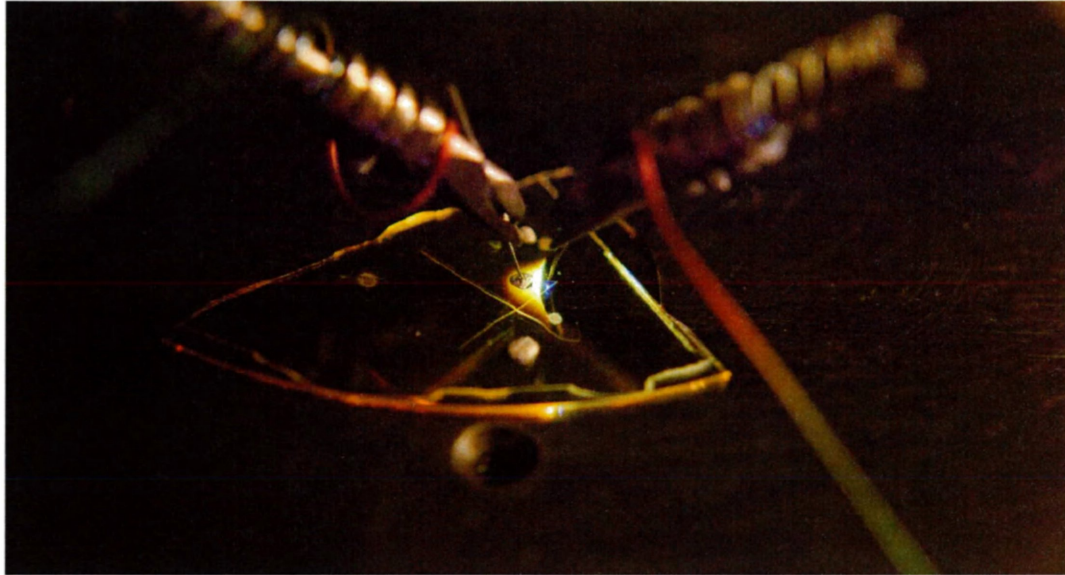


*Figure 3.2: The blue light from the magnesium energy level transition appears often, even when observing the light from a different structure, in this case an orange InGaN LED. Note: Image has been taken with a high exposure time (30s), but this blue light is still visible without a camera capture.*

This very process was tested on commercial p-type GaN as a baseline for comparison to MEAglow samples. A commercially acquired magnesium doped GaN template (MTI XTAL) grown by MOCVD on (0001) axis sapphire (Wurtzite configuration) was placed underneath two electrodes while 10mA of current passed through. Since the template was specified to be p-type, it was no surprise that blue light was easily visible - experimental results are described below.

The same test was then performed on four different magnesium doped GaN samples grown by low temperature MEAglow. The growth parameters will be discussed in the next chapter. Neither one of the samples displayed this blue light; simply, not enough current could pass through the electrodes. The 210 volt power source used for the measurement produced only microamps of current, which is not nearly sufficient to see light; milliamperes are needed. Hence, it was determined the samples were too resistive to perform such a measurement.

Electroluminescence was observed in these samples, albeit with a different approach. Instead

of probing across a highly resistive n-type oxide surface, the films were grown on top of a silicon doped n-GaN template (Oxford Instruments TDI74LS3640). The template was also oriented along the (0001) axis, had a thickness of  $2\mu\text{m}$  and a surface roughness less than  $3\text{nm}$  (RMS<sup>2</sup>). Fortunately, this template was placed in the reaction chamber alongside the bare sapphire measured above, and therefore both the p-GaN on sapphire and p-GaN on n-GaN films had identical characteristics. The n-type template was exposed by placing a cover on a portion of the template during growth, yielding a configuration like that of Figure 3.3. With the highly conductive n-type layer below the p-GaN surface, more current was able to be applied.

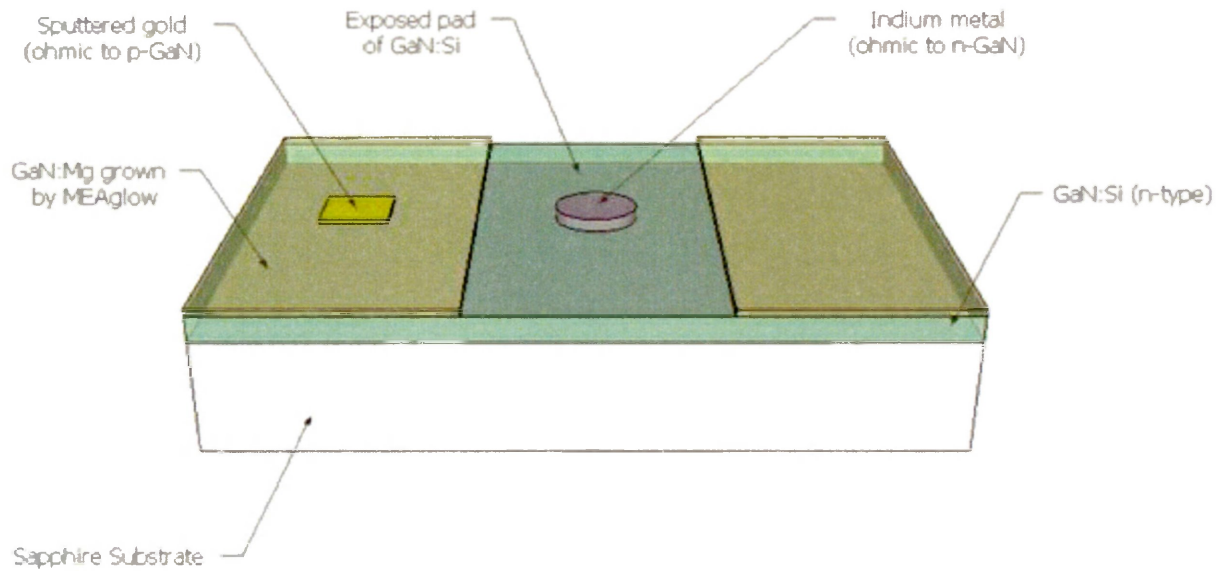


*Figure 3.3: The structure of the GaN:Mg sample grown on a GaN:Si template used for electroluminescence. Here, the GaN:Si layer is exposed to provide contacts to the lower layer.*

Light emission was visible to the naked eye for some samples, hence electroluminescence spectra were obtained to determine which light emitting sources were present. An optical fibre was coupled to an aperture on the base of the testing platform, directly underneath the film, so that light passing through the transparent sapphire base entered this interconnect and was

---

<sup>2</sup>Root-mean-squared

collected by a spectrometer (StellarNet Inc. EPP2000<sup>3</sup>). A spectrum sweeping between 188nm and 851nm at a resolution of 0.5nm was acquired. Due to the dimness of the p-n junction, the forward current applied to the device was set to an impressive 105mA and the acquisition time was set to 50,000ms. Acquisition occurred with minimal ambient room lighting. The results from this measurement are shown in Figure 3.4.

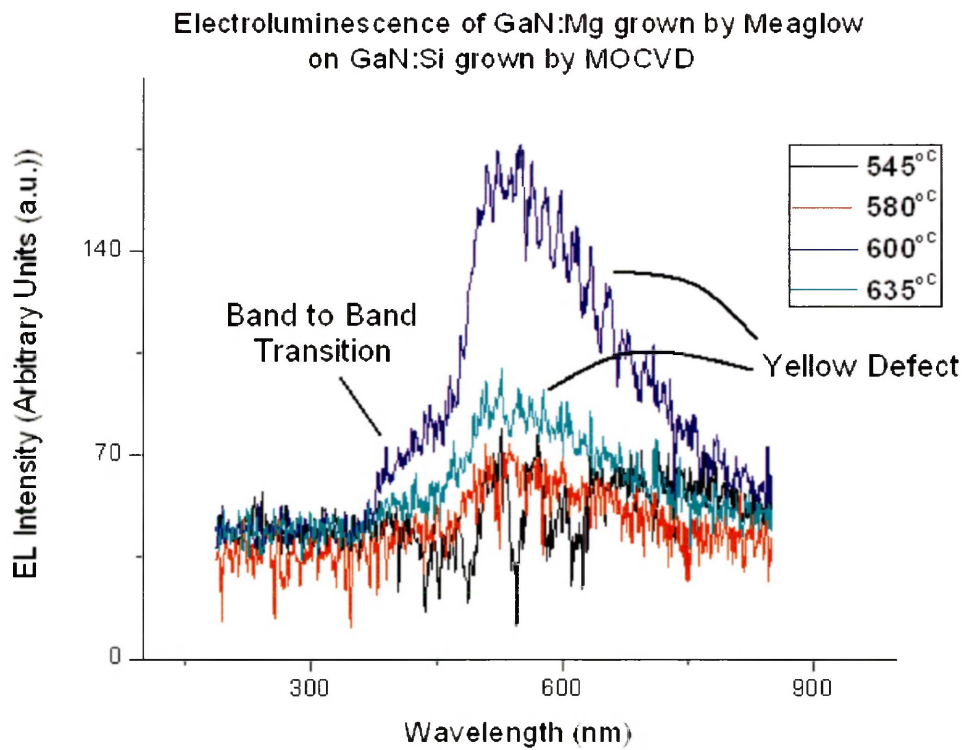


*Figure 3.4: Electroluminescence from GaN:Mg grown using low temperature MEAglow on GaN:Si. Data is shown using arbitrary units (a.u.) because detector gains, coupling efficiencies, acquisition times and resolution may differ between research groups; however, these parameters were kept constant. Growth temperatures are listed in the graph's legend. There is evidence of an emission from the band to band transition and magnesium (370-420nm) for certain samples, although it is weak compared to that from the yellow defect at 580nm.*

<sup>3</sup>CCD based, 200-1100nm range, 16-bit, 30dB SNR

To make a comparison, an electroluminescence spectrum was obtained from the magnesium doped GaN template grown by MOCVD, probing across the n-type surface oxide as done in Figure 3.1. Since the sample had brighter luminescence, the acquisition time was set to 5,000ms instead of 50,000ms. To assess if there was an effect due to the strong stimulus used above (105mA), the forward current applied was varied, starting at a level with barely detectable luminescence, and increasing to a level where damaging dielectric breakdown may occur (10,800 V/cm). The results are shown in Figure 3.5, and are indicative that the emission of samples grown by MEAglow was not adversely affected by large currents.

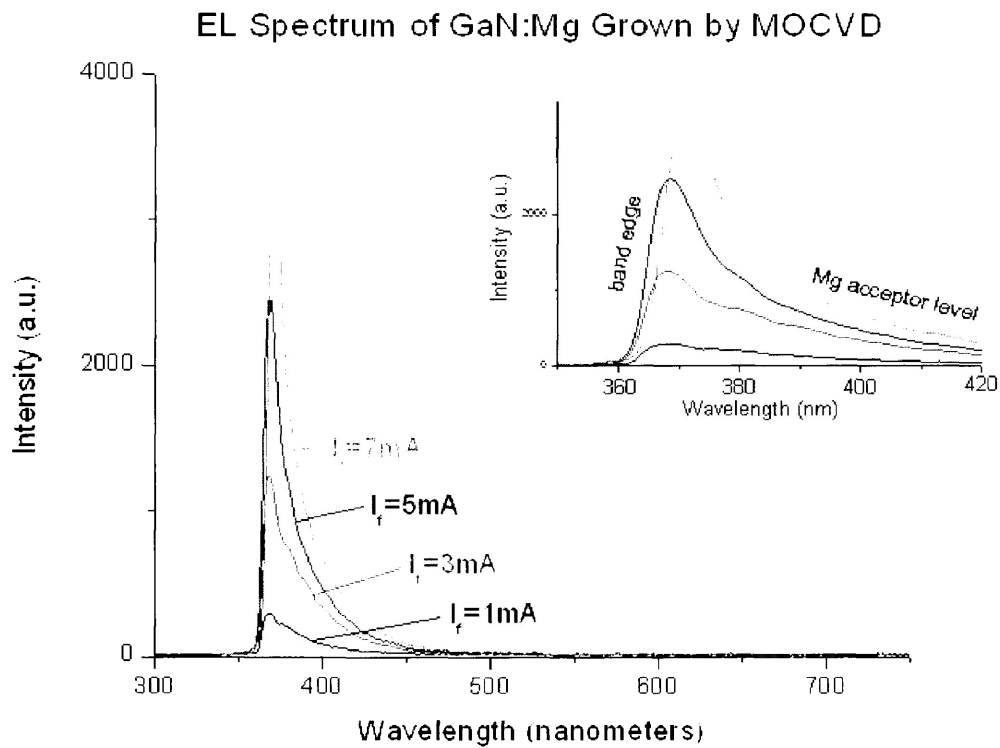


*Figure 3.5: Electroluminescence of commercial GaN : Mg grown by MOCVD measured across the surface oxide. Top right: an enlarged image around the peak luminescence region, attributing parts of the spectrum to different emission sources.*

The EL spectrum of GaN:Mg grown by MOCVD matched that which was expected. A peak

occurred at the band-to-band transition of 375nm, while its prolonged tail extended into the blue region corresponding to the magnesium energy level. As the forward current increased, the emission peak experienced a small redshift toward the magnesium emission.

Emission from the GaN:Mg samples grown by low temperature MEAgrow atop of GaN:Si, on the other hand, was heavily dominated by the yellow emission around 550-600nm. This is consistent with the presence of a yellow defect. However, there still is evidence of band edge and blue emission from two (possibly three) of the four samples probed. This is confirmation that p-type conductivity exists, even though the sample is heavily dominated by defects. For comparison, the p-GaN template grown by MOCVD did not have a yellow defect emission. An enlarged graph of the spectrum of GaN:Mg grown by MOCVD is shown in Figure 3.6. Looking at the noise floor, there is a partially concealed yellow emission at 550nm while another peak at 750nm is likely the harmonic of the main band edge (375nm) generated within the optoelectronics of the spectrometer. Since the yellow peak is about two orders of magnitude smaller than the band edge emission, it is considered to be non-existent.

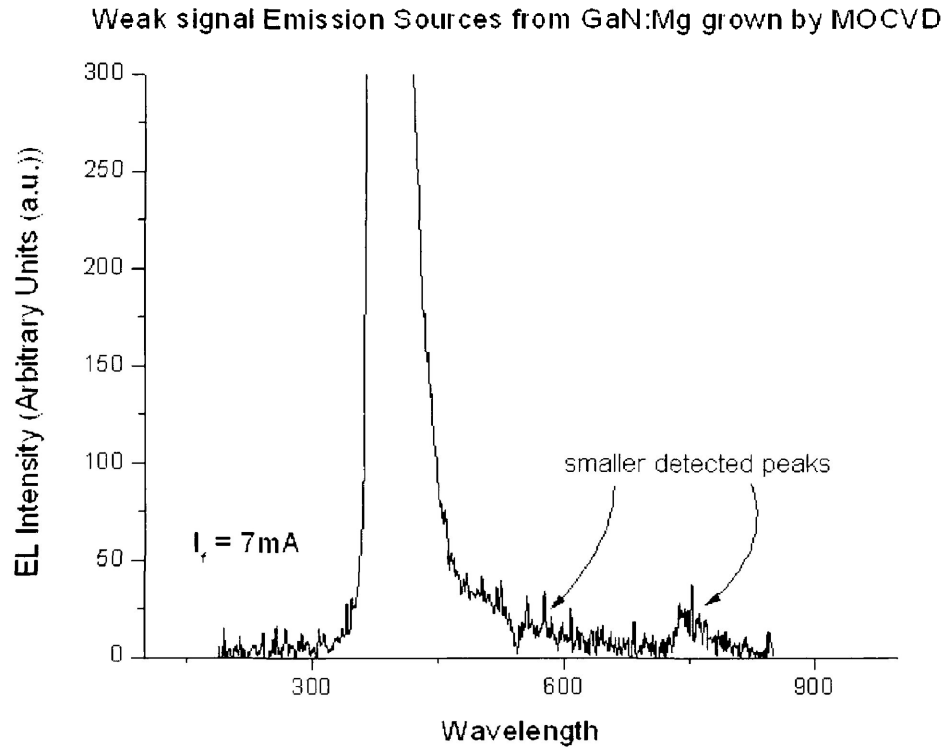


*Figure 3.6: Weak emission sources from current passing through two terminals placed on the surface of GaN:Mg grown by MOCVD. There is an evident harmonic at 750nm, and a questionable source at ~580nm (yellow).*

The UV and blue emission from MEAglow samples is evidence that p-type conductivity is present. No other known mechanisms other than a band-to-band transition can be attributed to these wavelengths. Hence, electron-hole recombination is occurring, and is evidence of the first p-type samples grown by MEAglow. The presence of the yellow defect, on the other hand, does not yield definite insight into the nature of the semiconductor; its source is highly debated. Some hypothesized causes are energy level transitions between a gallium vacancy ( $V_{Ga}$ ) and a carbon atom [51], a nitrogen atom in the place of a gallium one, iron impurities, lattice dislocations or an isolated gallium vacancy [32]. The last source,  $V_{Ga}$ , has gained partial acceptance because of its ready formation with oxygen donors as previously discussed, and also because of positron annihilation experiments that show a correlation between  $V_{Ga}$  and the yellow emission [32].

The implications of the presence of the gallium vacancies, if that is even the cause of the yellow defect, are numerous. First, it can be indicative of nitrogen rich conditions. The lack of gallium to cause its vacancy is an obvious consequence. Even though gallium flux may be sufficient, the yellow defect may be indicative of the amount of atoms that actually incorporate in the lattice. Second, the yellow band could indicate the presence of oxygen. There is a possibility of the correlation between the emission strength and the oxygen concentration<sup>4</sup> [32]. Further, anecdotal evidence notes the suppression of the yellow defect in magnesium doped GaN [52, 53] and the increase of the band under higher n-type doping [51]. Hence, the yellow defect is seen as a compensating centre, or at the very least, an unwanted emission peak.

## 3.2 Electrical Properties Measured by Hall Effect

### 3.2.1 Introduction to the Hall Effect Measurement

The Hall effect is a very common electrical measurement technique that, when using the Van der Pauw configuration, provides the semiconductor’s carrier concentration, carrier type (n or p), mobility and resistivity [54]. In principle, a magnetic field is used to force current in an orthogonal direction to its primary flow, allowing its perturbation to be probed using an additional pair of electrodes (Figure 3.7). Since the Lorentz force will cause charge to accumulate on the side walls of the sample, the intensity of the resulting voltage is indicative of the charge density present. In this configuration, carrier type is easily determined. Since the “right hand rule” dictates that both electrons and holes will accumulate on the same surface, the majority carrier in the semiconductor will determine the net polarity between the probes. Therefore, in the case of Figure 3.7, p-type semiconductors will yield a positive voltage. To obtain the carrier concentration, however, one needs to know the sample geometry. Since the measured voltage across the probes is a result of the electric field and the separation, if the sample width is smaller, so too should the measured voltage be. Therefore, by using electrostatic relationships and the

---

<sup>4</sup>The energy equivalence of the  $V_{Ga} - O$  complex to  $V_{Ga}$  alone is only presumed theoretically, so there may not be a direct link.

sample geometry, one can arrive at an expression for the carrier concentration. To obtain the resistivity and mobility, on the other hand, a four point probe must be used. By pumping current through two terminals and measuring the resulting voltage across an extra pair of high impedance probes, the reading is not influenced by the potential of the measurement electrodes. This way, if the electrodes are placed in the optimal configuration, the resistivity can be better determined.

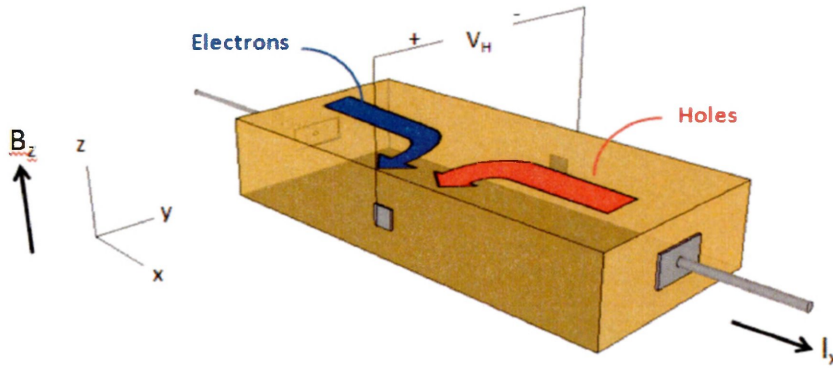


Figure 3.7: The Hall measurement of a bar sample. Here, current pumped in the  $x$  direction is curled toward the terminals located on the  $x$ - $z$  surfaces to generate a detectable Hall voltage.

### 3.2.2 Derivation of Carrier Concentration

The voltage across the probes, known as the Hall voltage, is a result of a steady state balance between electrostatic and Lorentz forces. As the Lorentz force causes charge to redirect and accumulate on one surface, the resulting electric field inhibits any further charge curl. Therefore, the following equilibrium is achieved:

$$F = q \left[ E_y + \vec{v} \times \vec{B}_z \right] = 0 \quad (3.1)$$

where  $E_y$  is the electrostatic field resulting from charge accumulation,  $\vec{v}$  is the charge velocity,  $q$  is the elementary charge magnitude, and  $\vec{B}_z$  is the applied static magnetic field. This equation

is traced to the Hall voltage by using two relations. Firstly, the drift velocity scales with the applied current,  $I_x$ , via:

$$v = \frac{J}{q(p-n)} = \frac{I_x}{q(p-n) \cdot Wd} \quad (3.2)$$

where  $J$  is the current density assumed homogeneous at any point within the sample, and  $W$  and  $d$  are the width and thickness of the sample respectively. The second relation is that the electric field induced by surface charge accumulation is assumed homogeneous along the cross section transverse to the current flow, and thus the linear relation,

$$V_H = -E_y W \quad (3.3)$$

holds. After combining and rearranging (3.2) and (3.3), the following equation for the carrier concentration is obtained:

$$p - n = \frac{IB}{qdV_H}. \quad (3.4)$$

These equations are usually simplified by defining the Hall resistivity,  $R_H = \frac{V_H W}{IB}$ , yielding

$$R_H = \frac{1}{q(p-n)} \quad (3.5)$$

Usually, the semiconductor at hand is doped to have a majority carrier concentration many orders of magnitude larger than that of the minority. Effectively, the relation becomes either

$$\left\{ \begin{array}{l} R_H = \frac{1}{qn} \\ R_H = \frac{1}{qp} \end{array} \right. \quad (3.6)$$

for p and n-type semiconductors respectively. Therefore, given an adequately doped semiconductor, and knowing the instrument and sample geometry, the linear relation between  $R_H$  and  $V_H$  indicates that a given pump current can determine the carrier concentration.

### 3.2.2.1 Four point resistivity and the Van der Pauw Method

Semiconductor resistivity is most accurately measured by a four point probe. Since the Van Der Pauw method [55] is such a measurement, its use is motivated here. Conversely, if only a two point probe were used, the low impedance of the source electrodes would force one of the contact points to ground potential, skewing the results. The resistivity measured would then be that of the semiconductor film, plus an extra contact resistance. While this contact resistance can be calibrated through multiple measurements, in contrast a single four point probe measurement immediately gives the true resistivity. For instance, if the contacts are equally spaced on the surface as in Figure 3.8, the voltage measured across the probes will be equal to

$$V = \frac{\rho}{2\pi l} \cdot I \quad (3.7)$$

where  $\rho$  is the sample resistivity,  $l$  is the separation distance between electrodes, and  $I$  is the applied pump current [56]. With this in mind, the four point resistivity is determinable, provided the right geometrical analysis is used.

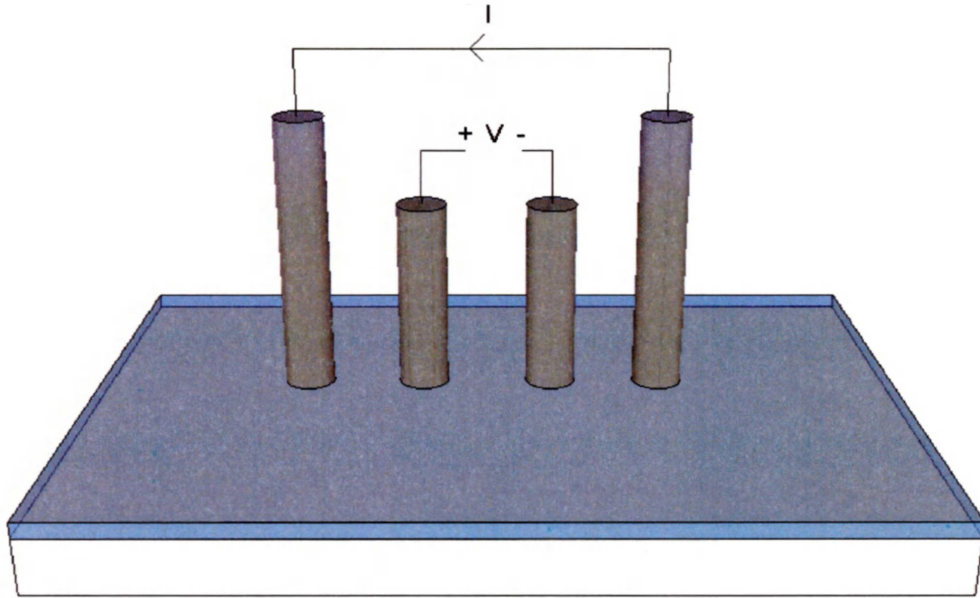


*Figure 3.8: The four point probe setup. Equally spaced contacts are placed sufficiently far from any edges. Current is passed through the outer terminals and the voltage is measured between the inner two.*

As far as four point measurements go, the configuration shown in Figure 3.7 is rather impractical. Epitaxy technology does not lend itself to have contacts placed on the sides of the wafer. Most often, the metal deposited for these connections is placed on the top surface. If the contacts are spaced around the edges of a thin disk (Figure 3.9), however, all Hall parameters listed above can be measured in one configuration. Known as the Van der Pauw method [55], it was shown that the Hall voltage, equal to

$$V_H = q \int_c (\vec{v} \times \vec{B}_z) \cdot d\vec{r} \quad (3.8)$$

where  $\vec{r}$  is a path along  $c$  connecting the two voltage probes, is invariant to the positioning of the electrodes, provided they are at the sample edge. To that end, a thin layer of GaN grown on an insulating sapphire substrate is exactly what this method is intended to measure. The

resistivity of this configuration is easily determinable, even if the geometric positioning of the electrodes is arbitrary. Van der Pauw showed that the following relation holds:

$$\exp\left\{-\frac{\pi R_{ABCD} \cdot d}{\rho}\right\} + \exp\left\{-\frac{\pi R_{BCDA} \cdot d}{\rho}\right\} = 1 \quad (3.9)$$

where  $R_{ABCD}$  is the four point resistivity of the voltage measured across terminals  $AB$  divided by the current passed through  $CD$ . By making these measurements, and knowing the thickness,  $d$ , of the film, the resistivity is calculated.

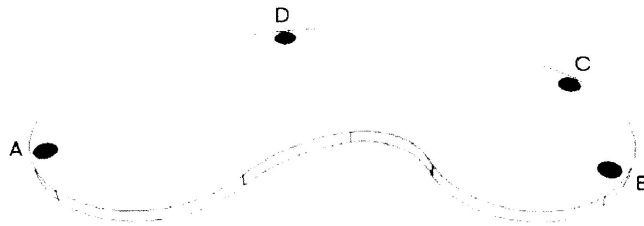


Figure 3.9: Contact positioning on any hypothetical thin disk as per the Van der Pauw method.

By taking additional measurements with and without the externally applied magnetic field, the carrier concentration can be determined. Through the relation described in [55], the Hall resistivity, and thus by definition the carrier concentration, can be found by:

$$R_H = \frac{1}{q \cdot p} = \frac{d(\Delta V_H)}{B \cdot I} = \frac{d}{B} (\Delta R_{BDAC}) \quad (3.10)$$

where  $\Delta R_{BDAC}$  is the change in four point resistance across diagonal pairs when adding the magnetic field, also known as the magnetoresistance. This assumes p-type conductivity, hence for n-type semiconductors,

$$R_H = \frac{1}{q \cdot n} = \frac{d(\Delta V_H)}{B \cdot I} = \frac{d}{B} (\Delta R_{BDAC}) \quad (3.11)$$

Therefore, determining the change in four point resistance due to an external magnetic field directly correlates to the carrier concentration.

Since the Hall effect is a small signal phenomenon, and since the semiconductor should be an isotropic medium, a multiplicity of equivalent measurements can improve the detection capability. For instance,  $R_{ABCD} = R_{BADC}$ , which says that if you reverse the polarity of the current, the same voltage appears across the probes, but in a different polarity. This technique is especially useful to counter any small rectifying behaviours at the probes. Furthermore, the Complementary V-I Reciprocity theorem holds ( $R_{ABCD} = R_{CDAB}$ ), indicating that if you switch the pair that pumps the current, the same voltage is measured [57]. Therefore,  $R_{ABCD}$  is usually measured in four ways (original, reverse polarity, reciprocal, and reciprocal with reverse polarity) and averaged to obtain a more accurate result.

Lastly, from the determination of carrier concentration, the mobility is found. Ohm's law states,

$$J = \sigma E = q\mu_p E \quad (3.12)$$

for p-type semiconductors where  $\sigma$  is the sample conductivity and  $E$  is any electric field. For n-type semiconductors,

$$J = \sigma E = qn\mu_n E \quad (3.13)$$

Since  $\sigma = 1/\rho$ , the expression for the mobility becomes

$$\begin{cases} \mu_p = \frac{1}{qp \cdot \rho} = \frac{R_H}{\rho} \\ \mu_n = \frac{1}{qn \cdot \rho} = \frac{R_H}{\rho} \end{cases} \quad (3.14)$$

To that end, knowing the resistivity from the four point probe and the Hall resistance from the application of a magnetic field, the mobility can then be determined.

### 3.2.3 Isotropy, Ohmic and Schottky contacts

The ability to make multiple measurements assumes the material at hand is isotropic, i.e. its behaviour will be the same in all directions. As a result, the current flowing through the material follows Ohm's law ( $V = I \cdot R$ ) and thus the reverse polarity measurements should equal that of the forward one. Usually for a bulk semiconductor in a macroscopic view, that is the case. However, when two different materials are in contact, electrochemical potentials must be matched in order for this to be true, yielding what is called an Ohmic contact. If they are mismatched, rectification occurs. In an extreme scenario, the same voltage applied in both polarities across a p-n junction would yield very different current flows. To a smaller extent, the same can happen with the metal-semiconductor junctions used to interface electrodes to the film shown in Figure 3.10. Here, the bands bend to maintain continuity of the Fermi level with respect to the vacuum level, rendering what is called a Schottky contact. Even appropriately chosen metals can exhibit a built-in potential of perhaps  $\sim 10mV$ . As a result, the averaging process becomes skewed. The built-in potential is greater for wide bandgap materials like GaN than for small ones. It is less likely there will be a match between metal work functions and semiconductor Fermi levels compared to small bandgap semiconductors. Therefore, the barrier height tends to be larger.

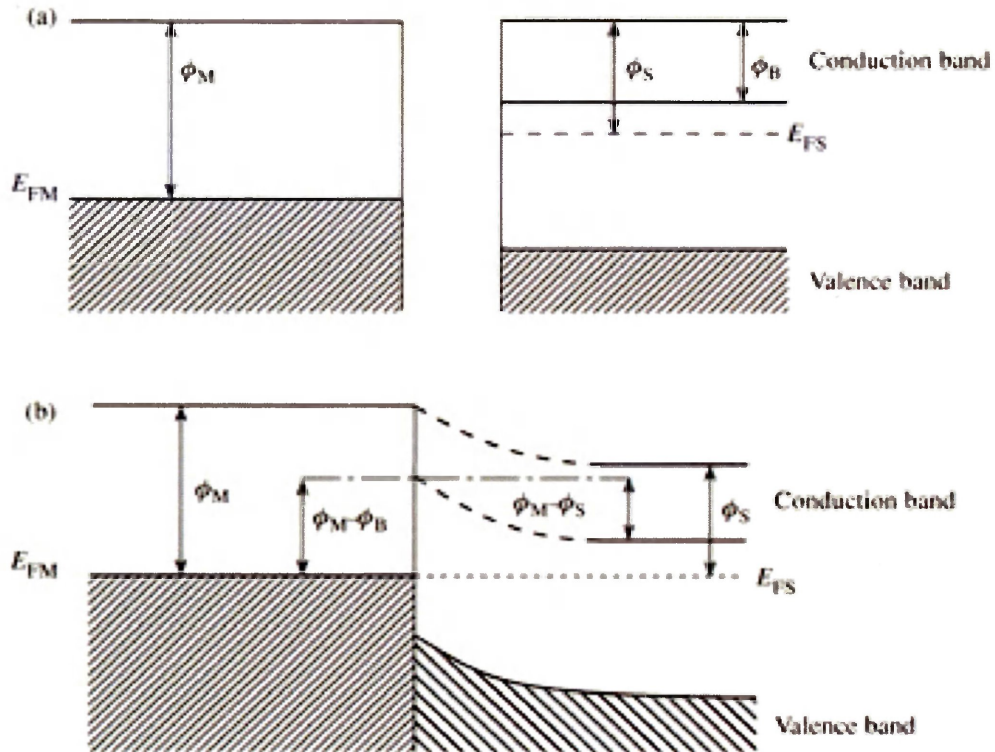
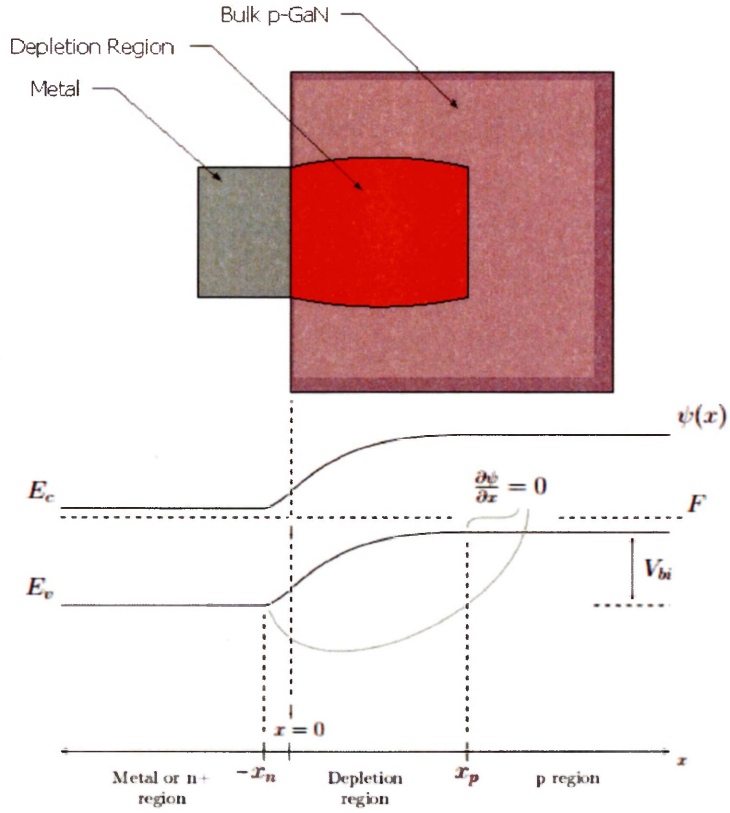


Figure 3.10: A Metal-Semiconductor junction and its resulting band deformation upon contact. Figure taken from [58]. a) Before contact is made. Each material has their own Fermi level or metal work function, and hence the bands are horizontal. b) Upon junction, these levels equate, and their difference is approximately equal to the potential difference between the two individual levels.

The effect of this potential mismatch can be reduced if the carrier concentration is high enough. The depletion region (Figure 3.11), where no charge surplus exists, decreases as the carrier concentration increases. This is due to the charge neutrality principle,  $x_n \cdot n = x_p \cdot p$ , in that no new charges are created. With higher concentrations, the depletion width is smaller, and therefore quantum tunneling can occur, reducing the effective barrier height. Other mechanisms can reduce the potential barrier. Thermionic emission across the junction, allowable energy states inside the bandgap at the metal surface and the presence of an equal image charge distribution along the metal surface all serve to lower the actual barrier height [58]. Therefore, instead of

referring to theoretical calculations of work functions and Fermi level mismatches to judge the appropriateness of a metal-semiconductor junction, it is easier to confirm the ohmic nature of contacts experimentally, as is done in the next section.



*Figure 3.11: A simplified depiction of the metal, p-GaN and depletion regions of a Schottky contact. Underneath is the resulting band diagram. Within the region proximal to the interface, a depletion region exists, bending the bands. The depletion edge is marked by where the band potential becomes horizontal (i.e.  $d\psi/dx = 0$ ). At this point, a built-in potential,  $V_{bi}$ , is formed due to the establishment of a common Fermi level,  $F$ .*

### 3.2.3.1 Experimental verification of ohmic contacts to GaN

The ohmic characteristic was verified for n and p-type GaN by observing their current-voltage (I-V) curves. Indium-tin (95:5 %) alloyed metal was placed on the four corners of a 1x1cm prepared sample of silicon doped GaN (n-type) grown by HVPE. The sample was then placed on a test board (Figure 3.12) and its I-V characteristics were measured using a current source capable of producing small currents ( $< 1nA$ ) and a voltage sensor with a resolution of  $1\mu V$  (Ecopia HMS-3000). The curves (Figure 3.13) show there is not a visible built-in voltage, indicating it is small ( $< 10mV$ ). Therefore, indium is a good choice of metal for n-type GaN contacts.

For p-type GaN, the semiconductor was etched in an HCl:H<sub>2</sub>O solution (1:3 parts) for 5 minutes and rinsed in deionized water for 2 minutes thereafter. This procedure was used to remove any surface oxides. Gold was then sputtered onto the semiconductor surface using a DC plasma source. A mask was in place during this application to ensure that the metal was only deposited on the corners as in Figure 3.14. The sample was then annealed at  $560^{\circ}C$  and  $10^{-4} Torr$  for 60 minutes. It was determined from multiple anneals at 560, 610 and  $660^{\circ}C$  that the annealing temperature had no effect on the contact quality or magnitude of rectification. I-V curves were taken in the same way as it was for n-GaN, and a linear relationship was shown. Investigating further, assuming a built-in potential did exist but was rather small, a span of weak currents ( $\pm 1.2\mu A$ ) was applied to measure this characteristic. Figure 3.15 shows that a small rectifying behaviour exists at the graph's origin, but its magnitude is  $10^{-4} Volts$ . Hence, the gold used was, for the purposes of this research, appropriate for ohmic contacts on p-type material. To conclude, based on these results, and the I-V response taken before every Hall measurement performed in this thesis, indium-tin metal is ohmic for n-type GaN, while gold is ohmic for p-type GaN.

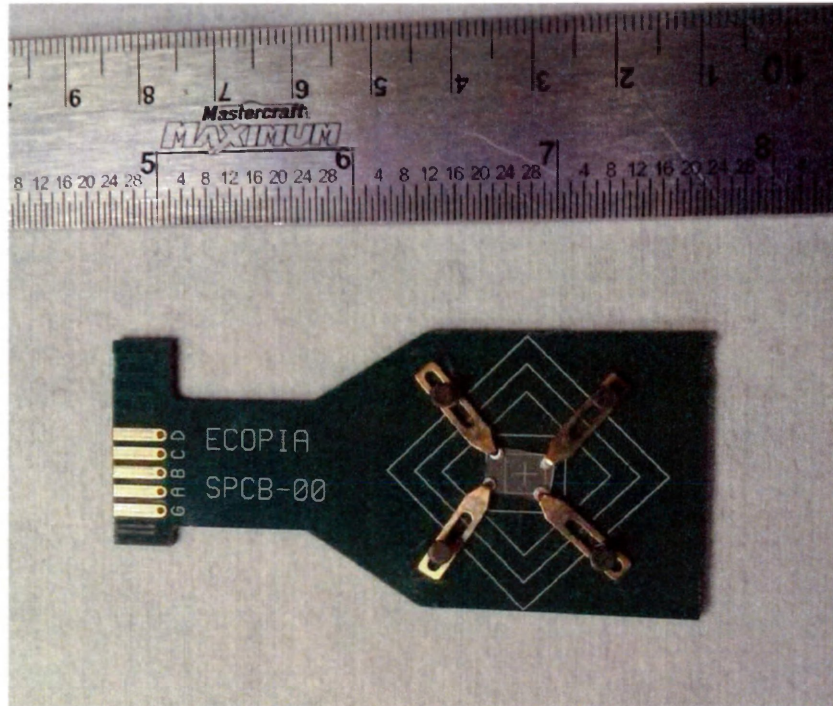


*Figure 3.12: The test board for I-V characterization. The semiconductor with four contacts is placed on the circuit board. Each of the four clips are connected to the contacts and traces within the circuit board interface with the instrument. A ground plane is used for better signal integrity.*

### I-V Characteristics of Indium on GaN:Si grown by HVPE

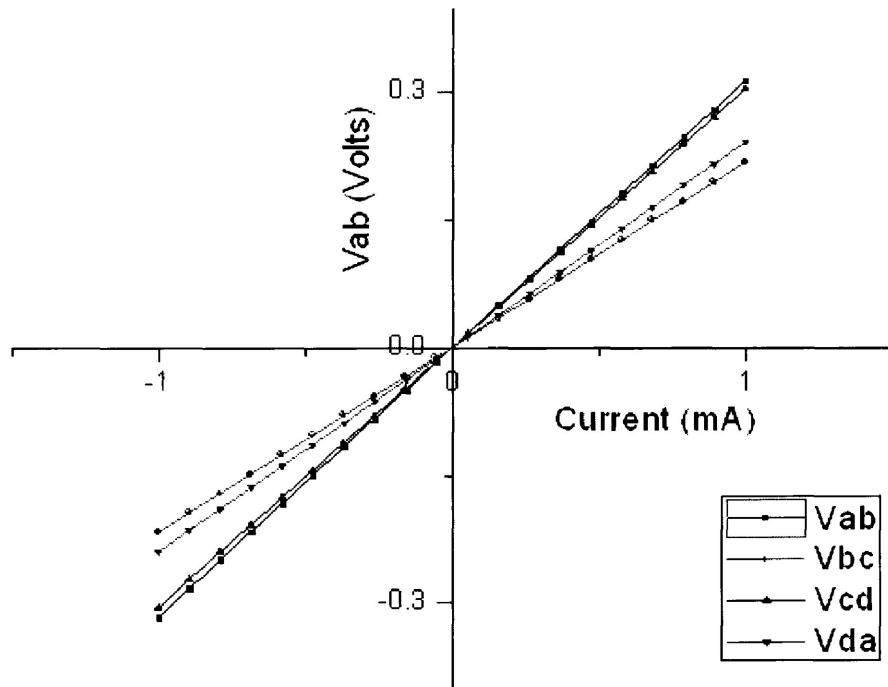
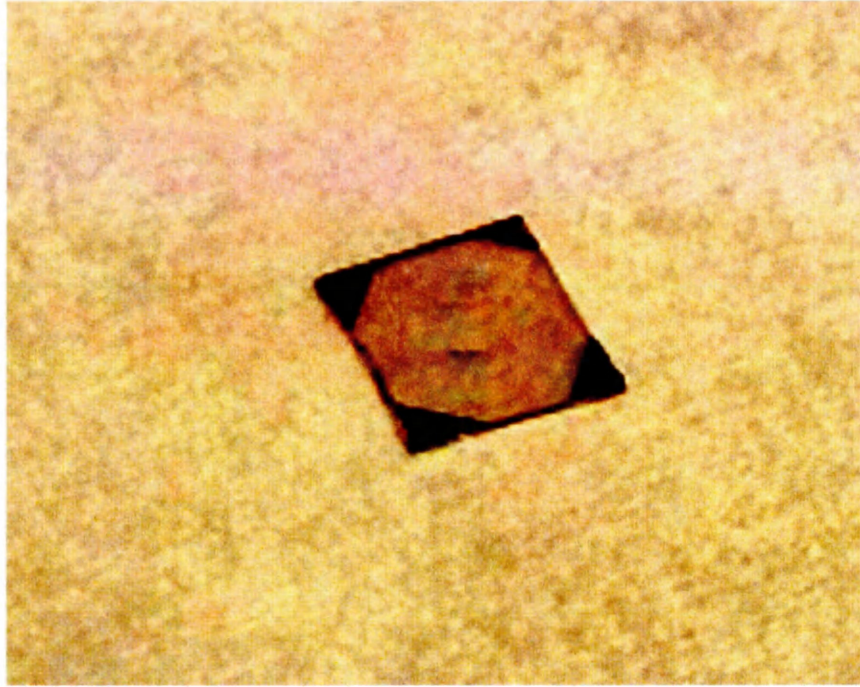
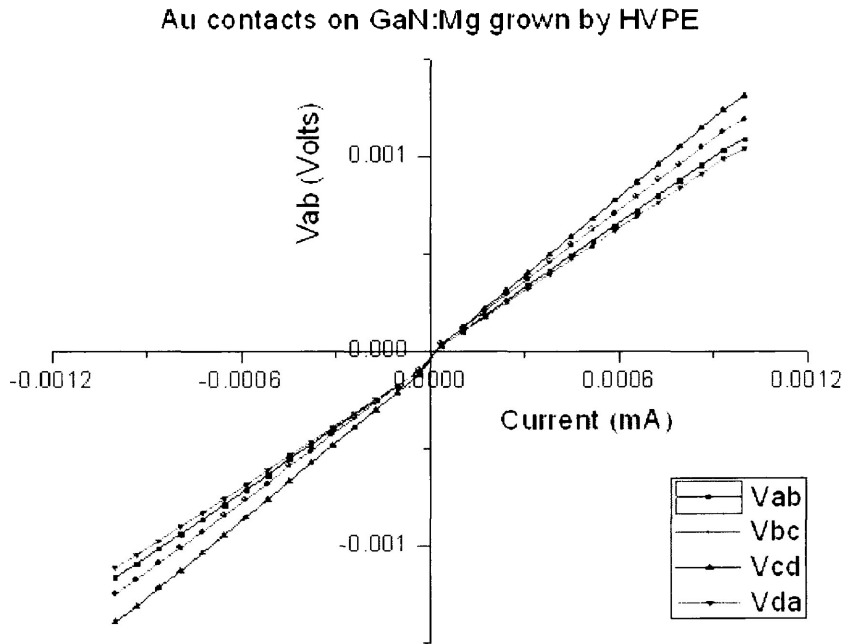


Figure 3.13 Investigation of the ohmic nature of indium contacts on n-GaN. IV curves show no built in potential for the range of currents used, and therefore it is smaller than about 0.03Volts, or 10% of the visible y-axis scale.



*Figure 3.14: : Preparation of a magnesium doped GaN sample for Hall measurements. First the section is annealed in  $H_2O : HCl$ , then gold is sputtered on the corners of the section, and finally it is annealed in a vacuum for 60 minutes.*



*Figure 3.15: Small signal measurement of the I-V response of gold contacts on GaN:Mg. A small,  $\pm 1.2\mu\text{A}$  sweep of current exposes even small rectifying behaviour. As is visible from the slight nonlinearity near the origin, the contacts had a built-in potential of around  $0.1\text{mV}$ , which is small enough for any measurement in this work.*

### 3.2.4 Hall Measurements on GaN

The Hall effect experiment was performed on GaN grown by HVPE, MOCVD and low temperature MEAgrow and followed the following protocol. Since the samples could be placed on the test board, an automated instrument (Ecopia HMS3000) measured all necessary parameters, provided the 1.0 Tesla permanent magnet was in place when necessary. The applied current was chosen to be such that it almost maxed the detector range of 2.0 Volts so that the Hall signal could be as large as possible. The delay before acquisition was set such that it was much smaller than the presumed time constant,  $\tau = R \cdot C$ , assuming a generous  $10\text{nF}$  capacitance and using the resistance measured in I-V characterization. This way, enough time was given for all the charge to accumulate to a steady state. Lastly, the sample thickness obtained from

scanning electron microscopy or Fabry P erot interferometry was specified and the measurements were subsequently made.

The results from samples of all three growth types are shown below in Table 3.1. The results did not match what was expected. Particularly, while all samples deemed n-type showed the appropriate carrier type, most of those deemed p-type also were measured to be n-type. Moreover, many magnesium doped samples had a higher electron density than the n-type, silicon doped samples. Another confounding observation was that the films grown by MEAglow were often too resistive to measure with the Hall effect system. While two samples had impressive resistivities of  $0.414$  and  $0.703\Omega \cdot cm$ , three others had such a large resistance between the terminal that feeding even a nanoampere of current to the sample would rail the  $2.0$  Volt detector. Two others had moderately high resistances that made the signal to noise ratio (SNR) small. If the sample is resistive, only a small amount of current (say,  $i = 1\mu A$  or less) can pass without clipping the detector. Since the added resistance from the magnetic field, magnetoresistance ( $\Delta R_{ABCD}$ ), is fixed, the Hall signal is only as large as this product,  $i \cdot \Delta R$ . When the sample is fairly resistive like this, sometimes the Hall signal is less than the noise of the detector, measured to be<sup>5</sup>  $0.52mV$ . As a result, the carrier concentration (and even the carrier type) is noisy.

---

<sup>5</sup>N=7, performed at room temperature. The noise comprises mainly of flicker noise ( $1/f$  noise) because it is a DC measurement ( $0 \rightarrow 1kHz$ ) and the thermal noise spectral density at room temperature is only  $10^{-20}V/\sqrt{Hz}$ .

Table 3.1: The carrier concentration, mobility and resistivity for GaN samples grown by HVPE, MOCVD, and various low temperature MEAglow samples. A positive carrier concentration implies a p-type sample, whereas a negative value reflect n-type. Stated accuracy is the greater of either the technical error in measurement ( $N=5$ ), or the percent variation in film thickness.

HVPE Sample	Carrier Concentration ( $cm^{-3}$ )	Mobility ( $cm^2/(V \cdot s)$ )	Resistivity ( $\Omega \cdot cm$ )
<i>GaN : Mg</i>	$-(1.71 \pm 0.03) \times 10^{18}$	$29.8 \pm 0.6$	$0.122 \pm 0.002$
<i>GaN : Si</i>	$-(4.1 \pm 0.08) \times 10^{17}$	$210.9 \pm 4$	$0.072 \pm 0.002$

MOCVD Sample	Carrier Concentration ( $cm^{-3}$ )	Mobility ( $cm^2/(V \cdot s)$ )	Resistivity ( $\Omega \cdot cm$ )
<i>GaN : Mg</i> Sample 1	$-(1.58 \pm 0.07) \times 10^{18}$	$10.3 \pm 0.2$	$0.04 \pm 0.01$
<i>GaN : Mg</i> Sample 2	$+(1.12 \pm 0.20) \times 10^{17}$	$12.15 \pm 2.1$	$4.66 \pm 0.02$

MEAglow Sample	Carrier Concentration ( $cm^{-3}$ )	Mobility ( $cm^2/(Vs)$ )	Resistivity ( $\Omega \cdot cm$ )
<i>GaN</i>	$-(1.03 \pm 0.1) \times 10^{19}$	$0.8 \pm 0.1$	$0.703 \pm 0.07$
<i>GaN : Mg</i> Sample A	$-(9.3 \pm 0.5) \times 10^{18}$	$16.1 \pm 0.2$	$0.414 \pm 0.04$
<i>GaN : Mg</i> Sample B, C	N/A	N/A	Resistive ( $> 10M\Omega$ )
<i>GaN : Mg</i> Sample D, E, F	N/A	N/A	Insulating ( $> 1G\Omega$ )

The results of the Hall experiment put the technique's suitability in question. If the device cannot properly measure the carrier type, how could it be confidently used to measure its concentration? Further, it also puts the experiment's execution in question. It is appropriate to ask if any wires were crossed, or if the magnetic field was in the right orientation. To address these concerns, the Hall experiment was performed on a sample of p-type germanium. Germanium is a nonpolar semiconductor whose drift is dominated by acoustic and nonpolar optical scattering [59]. Because these mechanisms are relatively simple, the carrier concentration can be determined *a priori* from the measured resistivity using a reference table, even without the

application of an external magnetic field. Therefore, instead of completely relying on the Hall method to determine the carrier concentration, a second approach is available for verification.

Contacts were placed in the corners of a p-type germanium sample. An indium-tin (95:5 %) alloy was used as shown in Figure 3.16. Even though the sample preparation was problematic in that cleaving the material did not result in a square sample, it was approximately rectangular and hence there was still sensitivity to the magnetoresistance. The choice of using indium metal was well founded. Indium has been published to be ohmic to p-type germanium [60, 61], and the I-V curves, measured here, between contact points showed the metal formed ohmic connections, having a built-in potential of less than  $30mV$  and possibly lower. The contacts were annealed in a vacuum at  $10^{-4} Torr$  and at a low temperature. The literature listed above suggests that an ambient much over  $400^{\circ}C$  would cause too much metal diffusion into the sample, thus the sample was annealed at<sup>6</sup>  $410^{\circ}C$ . The next parameter to specify was the sample thickness. Germanium is a bulk semiconductor, and hence Vernier calipers placed across the entire wafer were used to determine the sample thickness ( $0.55mm \pm 0.03mm$ ). The resistivity was specified by the manufacturer to be  $10.0 \rightarrow 10.4\Omega \cdot cm$ , and using a reference [62, 63, 64], the expected mobility and carrier concentration were then determined (Table 2).

---

<sup>6</sup> $400^{\circ}C$  was the target, but there was some overshoot

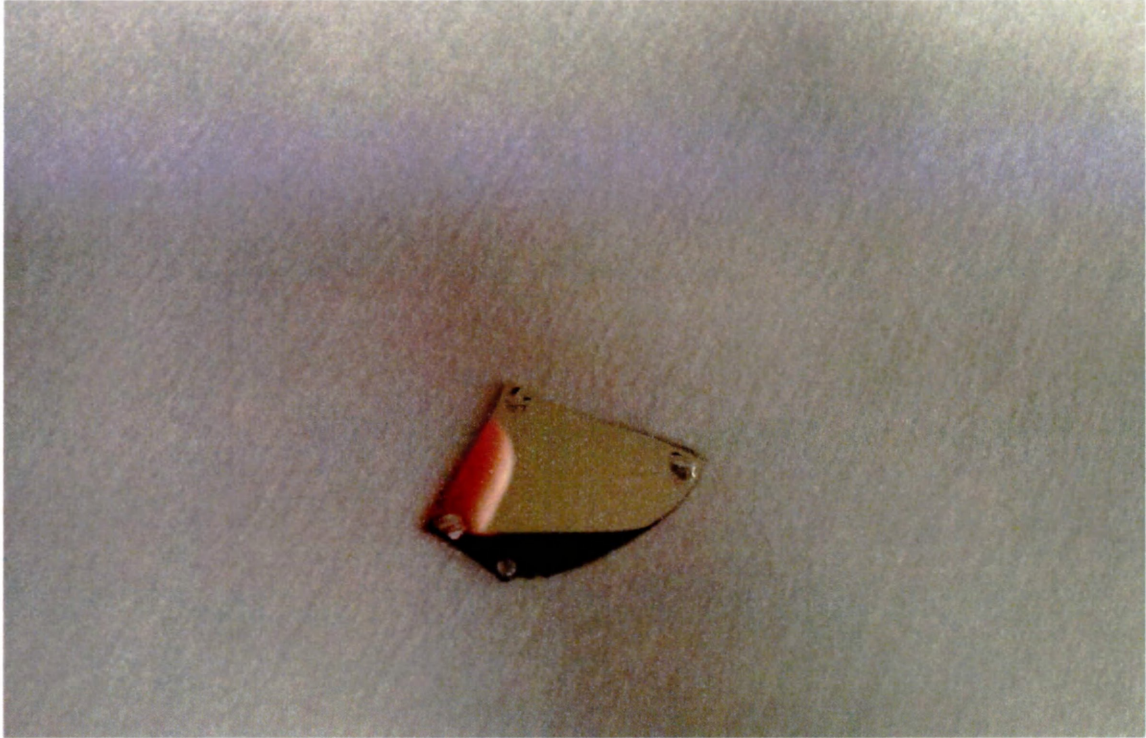


*Figure 3.16: p-type germanium Hall sample with annealed indium-tin contacts.*

*Table 3.2: The results of a Hall measurement of p-type germanium. Values were compared to those expected as obtained by manufacturer's specifications and resistivity-concentration reference tables. A positive carrier concentration implies an excess of holes. Sample error was mainly due to that from measuring the germanium thickness.*

Parameter	Measured	Expected
Carrier concentration ( $cm^{-3}$ )	$+(2.8 \pm 0.1) \times 10^{14}$	$+3.2 \times 10^{14}$
Hall mobility ( $cm^2/(V \cdot s)$ )	$2180 \pm 30$	2300
Resistivity ( $\Omega \cdot cm$ )	$10.2 \pm 0.2$	$10 \rightarrow 10.4$

The results of the measurement matched exceptionally well with the expected values. The characteristic with the largest discrepancy between expected and measured values was the carrier concentration, with a 14% mismatch. Having confirmed the correct operation of the Hall system,

the question of why the GaN measured in this research had such unexpected results remains unanswered. The first explanation could be a concept called the Hall scattering factor. Hall measurements are usually not exact, so a correction factor is used. The expressions for Hall resistivity and mobility found in equations (3.6) and (3.14), respectively, become:

$$\left\{ \begin{array}{l} R_H = \frac{r}{q \cdot p} \\ R_H = \frac{r}{q \cdot n} \end{array} \right. \quad (3.15)$$

$$\left\{ \begin{array}{l} \mu_p = \frac{R_H}{r \cdot \rho} \\ \mu_n = \frac{R_H}{r \cdot \rho} \end{array} \right. \quad (3.16)$$

While this factor is between 1.0 and 1.2 for silicon and is often ignored [65], it can be as high as  $1.6 \rightarrow 1.8$  for GaN [66, 67]. Therefore, up to 80% of error is inherent in the measurement of GaN. The inaccuracy arises from the energy dependence of scattering processes. There is a thermal distribution in drift energy, and the carrier's mean time to scattering,  $\tau$ , is higher for higher energy particles, making measurements that are usually under or overrepresented. Therefore, a further investigation into the scattering mechanisms and how it applies for each of the GaN samples measured could yield insight as to why n-type GaN showed weaker electron concentration than that of p-type GaN.

What could better explain most of the surprising measurements made in Table 3.1 is that the semiconductor film could be compensated. The fact that the Hall measurements are n-type make this an obvious conclusion, but this is not in agreement with the electroluminescence experiments. Band edge emission was detected on magnesium doped GaN grown by both MOCVD and low temperature MEAglow. Logically, then, one presumes the material is in fact p-type. What would explain how magnesium doped GaN measures a plethora of electrons is if the films were partially compensated and the effect of the electrons on the Hall system was emphasized over the holes. The equations in (3.6) and (3.14) for carrier concentration and mobility, respectively, reflect that of a semiconductor whose majority carriers greatly outweigh that of the minority. This is often

the case in doped semiconductors, and the Hall instrument assumes this property in yielding a measurement value. However, a more accurate expression for the resistivity of the semiconductor is

$$\rho = \frac{1}{\sigma} = \frac{1}{q(\mu_n n + \mu_p p)}. \quad (3.17)$$

If this expression were to be used in the derivation of the Hall parameters, the expression for the Hall resistivity becomes [27]:

$$R_H = \frac{r}{q} \frac{\mu_p^2 p - \mu_n^2 n}{(\mu_p p - \mu_n n)^2} = \frac{1}{q n_H} \quad (3.18)$$

where  $n_H$  is a pseudo electron concentration determined by the Hall system and can be replaced by the pseudo hole concentration,  $p_H$ , if necessary. The issue of this relationship is that electron mobility is generally higher than hole mobility. Usually, hole mobility varies around  $10 \rightarrow 100 \text{ cm}^2/(V \cdot s)$  and that of electrons is  $100 \rightarrow 1000 \text{ cm}^2/(V \cdot s)$  [62]. Supposing the hole concentration was  $10^{18} \text{ cm}^{-3}$  as is common in literature described earlier, the background electron concentration was  $10^{17} \text{ cm}^{-3}$ , and the hole and electron mobilities were 20 and  $100 \text{ cm}^2/(V \cdot s)$  respectively, the Hall concentration would be  $n_H = -1.6 \times 10^{17} \text{ cm}^{-3}$  of electrons<sup>7</sup>. So even though, in this hypothetical situation, there was a much greater surplus of holes, the higher electron mobility rendered the result of the Hall measurement as n-type. The switching of carrier type happens easily. The numerator of equation (3.18),  $\mu_p^2 p - \mu_n^2 n$ , tends to change signs often since the mobility difference is amplified by its square. Therefore, even a weakly compensated material whose electron density is  $(\mu_n/\mu_p)^2$  times smaller than the hole concentration could still measure n-type.

To determine the degree of compensation, experimenters use a variable temperature Hall effect system. By cooling with liquid nitrogen or by electrical heating, the donor or acceptor

---

<sup>7</sup>assuming a unity Hall scattering factor

impurities can be activated or inactivated individually as per the equations [27]:

$$p = N_A \cdot \exp\left(-\frac{E_a}{k_b T}\right) \quad (3.19)$$

$$n = N_D \cdot \exp\left(-\frac{E_d}{k_b T}\right) \quad (3.20)$$

Magnesium has an electrical activation energy around  $150\text{meV}$  and the compensator oxygen has one around  $32\text{meV}$  [34]. Transitioning the ambient around the temperatures corresponding to these thermal energies ( $1445^\circ\text{C}$  and  $97^\circ\text{C}$  respectively) should affect the impurities' performance.

An attempt to determine the amount of compensation was made. First, the effect of the donor impurities was probed. The ratio  $p/n$  as per equations (3.19) and (3.20) is very small at low temperatures, and is equal to 0.2% if the ambient temperature is at, say<sup>8</sup>,  $-78^\circ\text{C}$ . So provided the compensation is adequate, the measured result should reflect that only from the donors. To that end, the entire Hall apparatus containing the semiconductor film was first refrigerated for two hours to prevent thermal shock, and then placed inside an insulating styrofoam container (Figure 3.17) with approximately 500mL of dry ice for one hour. A sample of magnesium doped GaN grown by HVPE whose carrier concentration measured n-type at room temperature ( $-1.71 \times 10^{18}\text{cm}^{-3}$ ) was the film in question. A thermometer was held beside the permanent magnet and measured well below its limit of  $-20^\circ\text{C}$ , so it was assumed the ambient temperature was in between that and  $-78^\circ\text{C}$ . The Hall effect proceeded as per the above protocol. Next, on a different day, the entire apparatus was heated in a dry furnace to  $82^\circ\text{C}$  for 105 minutes and subsequently placed in the container for testing. Higher temperatures would have been used, but the plastic components in the magnet holder could have been damaged by the heat. To maintain ambient temperature when opening the container, a heat gun was applied prior to its resealing. After the experiment, the container was sealed for 15 minutes to equilibrate the temperature and a Type K thermocouple measured the ambient to be  $55^\circ\text{C}$ . A summary of the measurements is

---

<sup>8</sup>the sublimation temperature of dry ice

listed below in Table 3.3.

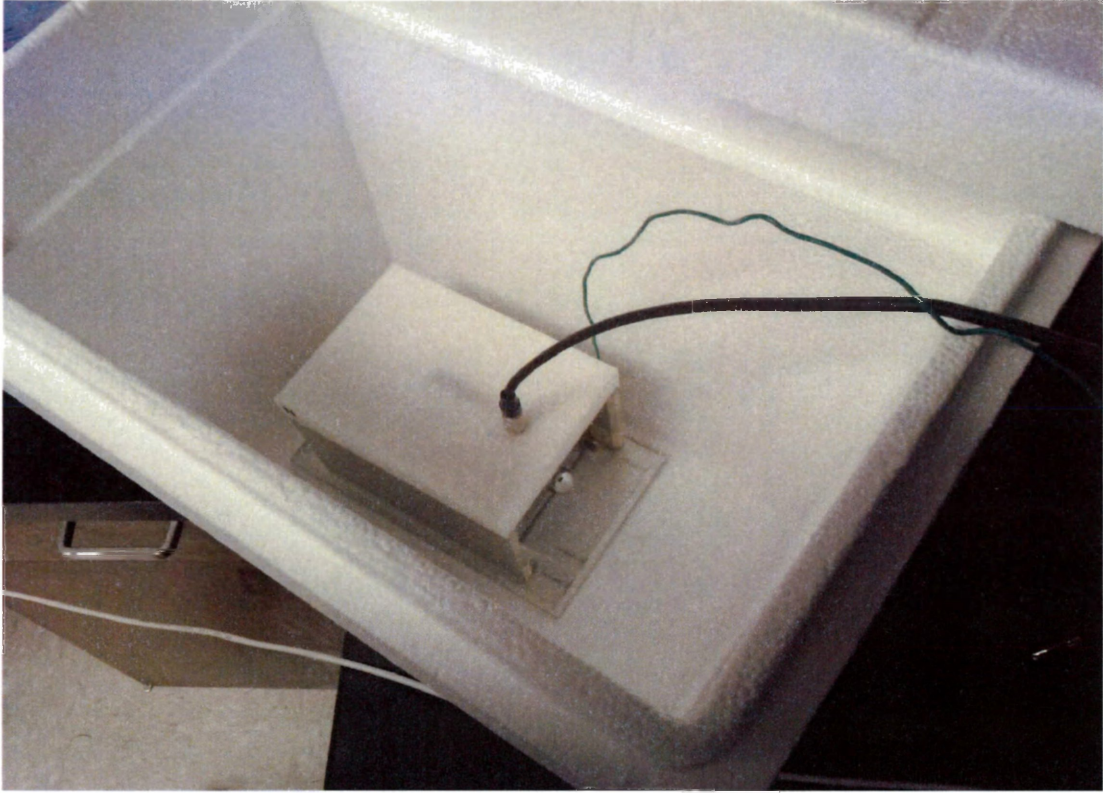


*Figure 3.17: The placement of the Hall system in a thermally insulating styrofoam container.*

*Table 3.3: The carrier concentration of GaN:Mg grown by HVPE measured at high and low temperatures in a thermally insulating container. Negative carrier concentrations imply a surplus of electrons.*

Temperature	Carrier Concentration
Room temperature (21°C)	$-1.76 \times 10^{18} \text{cm}^{-3}$
Low temperature (-50°C)	$-1.65 \times 10^{18} \text{cm}^{-3}$
Higher temperature (55°C)	$-2.04 \times 10^{18} \text{cm}^{-3}$

The experimental results showed a decrease in carrier concentration as temperature increased, even though the change was small. Nevertheless, it was still statistically significant. The data acquisition's standard deviation was recorded to be  $\sigma = 2.2 \times 10^{16} \text{cm}^{-3}$ , or 1.3% of the nominal

value ( $N = 9$ ), and with that the  $2\sigma$  statistical interval<sup>9</sup> with respect to the room temperature measurement was small ( $-1.71 \times 10^{18} \text{cm}^{-3}$  to  $-1.81 \times 10^{18} \text{cm}^{-3}$ ). Hence, the effect was due to the changing of temperatures, and not random processes ( $p < 0.0001$ ). The increase in electron concentration as temperature increases could be explained simply by the further activation of the donor species. Figure 3.18 shows calculations of the net carrier density as temperature is increased for a semiconductor with both magnesium and oxygen impurities having activation energies of  $150 \text{meV}$  and  $32 \text{meV}$  respectively. Depending on the degree of compensation, it is not until temperatures greater than  $600^\circ\text{C}$  that magnesium dopants strongly make the sample p-type. Hence, increasing the temperature a meagre  $30^\circ\text{C}$  only serves to activate the oxygen donors.

Since, for all intents, only the donors are present, its impurity concentration was then calculated. At the dry ice temperatures, only 17% of the donors were thermally activated on account of equation (3.20). Thus, the low temperature measurement must be divided by a factor of 0.17 to obtain the final result. Through this method, the total donor impurity concentration was found to be  $9.47 \times 10^{18} \text{cm}^{-3}$ . At room temperature, 27% of these donors are expected to be activated. Therefore, the HVPE sample shown in Table 3.1 contains  $-2.58 \times 10^{18} \text{cm}^{-3}$  of electrons.

Normally, the measurement made at high temperatures would be used to determine the magnesium impurity concentrations. Extremely hot environments would fully activate both impurities, and by knowing the electron concentration found above, the density of activated magnesium could be calculated. At the temperatures achieved in the above experiment, however, not many more holes are being activated. In fact, the hole concentration is expected to increase by a factor of only 1.5 according to equation (3.19). Hence, it is deemed that this change is too small to accurately determine the magnesium concentration, and that careful study of this property should be reserved for instruments with very wide temperature ranges.

---

<sup>9</sup>95.45% of the population

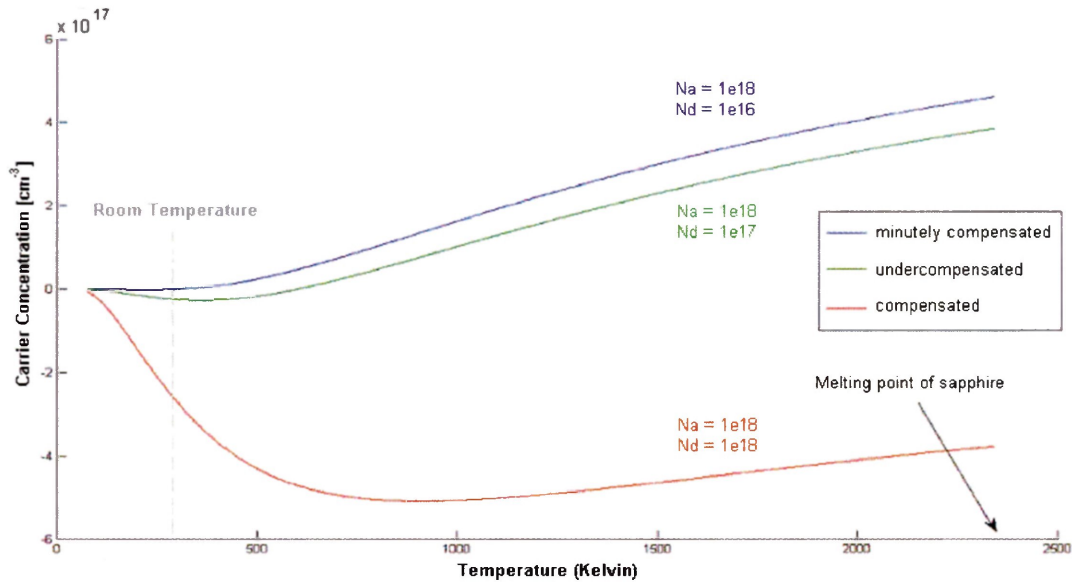


Figure 3.18: A simulation of the net carrier concentration of magnesium doped GaN compensated by oxygen as a function of temperature. Here, Boltzmann statistics are assumed, using activation energies of 150meV and 32meV for magnesium and oxygen respectively.

### 3.3 Fermi Level Measurement through I-V Characteristics

The last phenomenon studied in this work that could provide insight into the carrier concentration of the p-type layer is the built-in potential when the layer is in contact with another material. By determining the position of the p-side Fermi level relative to that of a well studied n-side, the absolute built-in potential can be determined, thus yielding information about the carrier concentration. The choice of the ‘well studied’ material is critical. For instance, if the built-in potential came from a Schottky contact, it would reflect a smaller energy difference on account of the surface states, thermionic emission etc. described earlier, rendering the analysis more complicated. Hence, the accuracy of this approach is limited by the true knowledge of the n-type layer.

A layer of silicon doped n-type GaN grown by HVPE, used in the electroluminescence experiments<sup>10</sup> was the template for MEAgrowth. It should not be a compensated material

<sup>10</sup>The GaN:Si was the template for p-GaN grown by MEAgrowth

since no magnesium is present and since background impurities in GaN grown by this technique are predominantly n-type. Thus, its Hall concentration ( $-(4.10 \pm 0.08) \times 10^{17} \text{cm}^{-3}$ ) should accurately determine its Fermi level. Four p-GaN films were produced on top by first applying a nucleation layer, then growing the film using a metal modulation technique, and finally thermally activating the magnesium. Each sample, however, was grown at different temperatures to observe how low a temperature GaN could be grown if it were placed atop an InGaN layer to prevent indium desorption. The temperatures used were  $545^{\circ}\text{C}$ ,  $580^{\circ}\text{C}$ ,  $600^{\circ}\text{C}$  and  $635^{\circ}\text{C}$  for samples labeled #1, #2, #3 and #4 respectively.

By using Boltzmann statistics,

$$n = N_C \cdot \exp\left(-\frac{E_C - F_n}{k_b T}\right) \quad (3.21)$$

where  $N_C$  is the conduction band's effective density of states ( $2.3 \times 10^{18} \text{cm}^{-3}$  [62]),  $E_C$  is the conduction band energy and  $F_n$  is the material's Fermi level, the Hall concentration was used to determine that the Fermi level was  $43.8 \text{meV}$  away from the conduction band of the GaN:Si template. The built-in potential between GaN:Si and GaN:Mg, measured by I-V characterization, was used to determine the p-GaN Fermi level relative to  $F_n$ . Two electrodes contacted both sides of the p-n junction as in Figure 3.3. Again, gold was used as the ohmic contact for the p-type layer and indium for the n-type layer. Finally, the hole concentration was calculated.

The resulting I-V curves are shown below in Figure 3.19. Here, it is not immediately evident what the built-in potential is. The rectifying behaviour is being drowned out by the series resistance between the contacts. The slope of the curve in the resistive region - where the flatband condition is undoubtedly obtained - was measured to obtain the series resistance,  $R_s$ , and the resulting voltage across it ( $I \cdot R_s$ ) was removed from the data. The graphs then show more clearly what the built-in potential is (Figure 3.20). Specifically, the potential difference is  $0 \text{eV}$ ,  $0.55 \text{eV}$ ,  $3.1 \text{eV}$  and  $2.0 \text{eV}$  for Sample 1, 2, 3 and 4 respectively.

These graphs may be slightly erroneous. The curves past the knee point sometimes do not

reflect the exponential nature a p-n junction should, and sometimes bends back on themselves. This could be due to the measurement of the series resistance, where too much of a voltage drop was attributed across the bulk. Nevertheless, if the resistance was slightly different, the built-in potential would still be visually similar as determined by extrapolating the flat band condition and hence not much error is obtained.

As planned, these built-in potentials were then used to determine the carrier concentrations. First, the energy separation from the valence band was determined via:

$$E_v - F_p = E_C - F_n - V_{bi} \quad (3.22)$$

where  $E_v$  is the valence band energy. Using the definition of the bandgap energy,  $E_g = E_C - E_v$ :

$$F_p = E_g - (F_n - V_{bi}) \quad (3.23)$$

and the hole concentration can be found through the Boltzmann relation,

$$p = N_v \cdot \exp\left(-\frac{F_p - E_v}{kT}\right) \quad (3.24)$$

where  $N_v$  is the effective density of states in the valence band ( $4.6 \times 10^{19} \text{cm}^{-3}$  [62]). Using their measured bandgaps,  $3.05 \text{eV}$ ,  $3.2 \text{eV}$ ,  $3.3 \text{eV}$ , and  $3.18 \text{eV}$  for samples 1, 2, 3 and 4 respectively (see Chapter 4), the differences in energy levels between the valence band and that of the Fermi level is  $2.81 \text{eV}$ ,  $0.16 \text{eV}$  and  $1.14 \text{eV}$  for samples 2, 3 and 4 respectively. Sample 1 showed no built-in potential. The proximity of the Fermi level in the p-GaN side to the valence band for sample three is very encouraging, and its carrier concentration was calculated to be  $9.9 \times 10^{16} \text{cm}^{-3}$ . While sample 4 has a Fermi level closer to the valence band than that of the conduction band, it was very distant and yielded a net hole concentration of  $1.48 \times 10^0 \text{cm}^{-3}$ . In other words, it was highly compensated by the background electron concentration and would be too insulating to

measure. In fact, a measurement of this small a value is so unstable that accuracy issues could change its result by several orders of magnitude. The Fermi level of sample 2 did not pass the midband, and again, sample 1 showed no built-in potential.

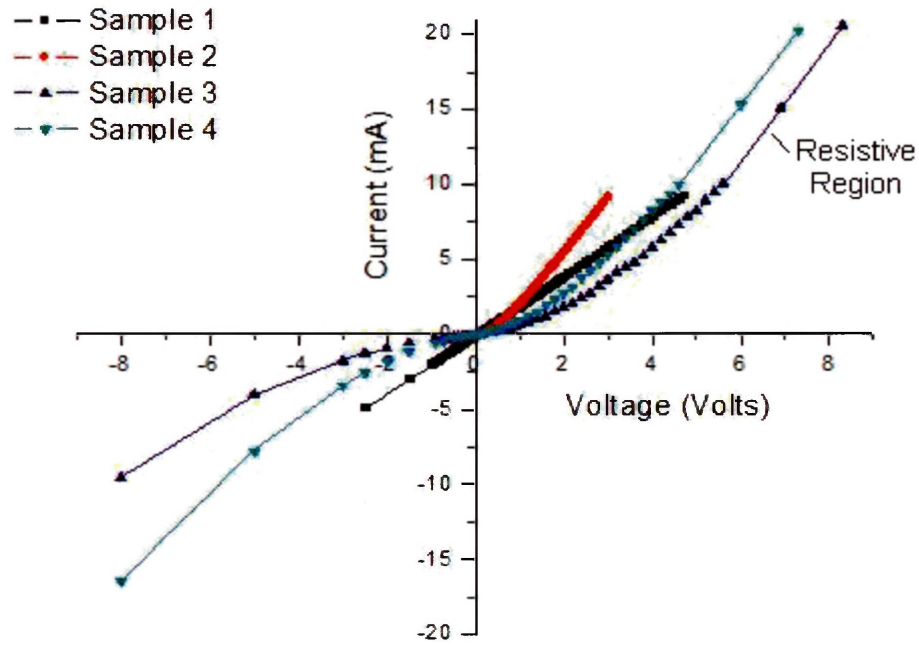


*Figure 3.19: I-V response of four samples of GaN:Mg grown by MEAgrow on GaN:Si grown by HVPE. Here, electrodes contacted the ohmic gold pad on the p-side and the ohmic indium-tin pad on the n-side. Characteristics were heavily dominated by series resistance, especially sample 1 which showed no rectification.*

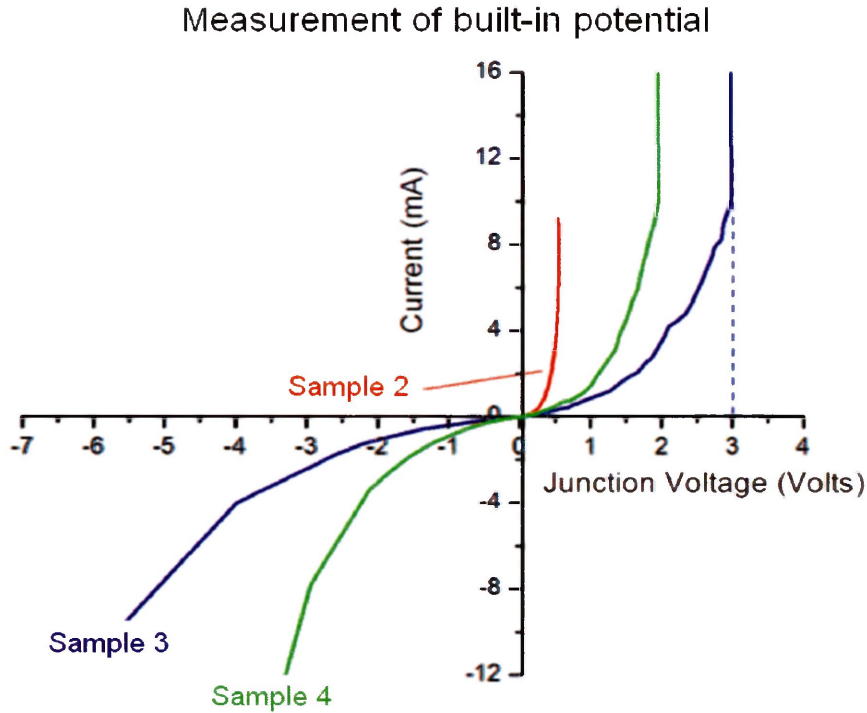


*Figure 3.20: I-V characteristics of GaN:Mg grown by MEAglow on GaN:Si grown by HVPE with respect to the junction voltage only. The voltage across the series resistance has been removed by calculating the resistance and multiplying it by the forward current. This way, the ‘knee point’ of the curve is exposed.*

This is the first definitive electrical measurement that yielded a potentially accurate p-type result for films grown by low temperature MEAglow. Even though EL measurements showed the samples at hand were p-type, a reliable carrier concentration was not found. Further, Hall measurements were reflective of compensated material, and hence its measured carrier density was unreliable. Therefore, this approach is the most useful in the characterization platform at hand.

A hole concentration of  $9.9 \times 10^{16} \text{cm}^{-3}$  is a significant result. It is on the order of that found in the literature. Therefore, it shows the viability of MEAglow as a method to produce p-type materials. Furthermore, the charge concentration determined was combating the background

electron concentration. Since its magnitude was determined to be  $-2.58 \times 10^{18} \text{cm}^{-3}$  of electrons through low temperature Hall experiments, even sample 4, which has virtually no net holes, had enough to combat the electrons.

Finally, it is satisfying to note that the proximity of the Fermi level to the valance band correlated with the intensity of the electroluminescence. Sample 3 had the highest peak in both the band edge and yellow emissions, sample 4 had the next largest source, sample 2 had a noticeable yellow defect with a barely detectable band edge, and sample 1 had no emission at all. These results corroborate the carrier concentration determined by the I-V curves here.

### 3.4 Chapter Summary

The carrier concentration was investigated by probing three different phenomena: electroluminescence, carrier drift and current rectification. Each of these interactions are directly influenced by the carrier concentration. Specifically, EL from the band edge indicates the presence of both electrons and holes in their respective regions, the Hall voltage scaled with carrier concentration and the built-in potential in a p-n junction has a logarithmic (Boltzmann) relation to carrier concentration. It was found that the Hall experiment was not suitable to measure these sorts of samples since a compensated material has a tendency to overemphasize the electron drift over that of the holes due to the former's higher mobility. This was found not only in samples grown in the MEAglow system, but the commercially acquired films as well, indicating the tendency for oxygen to also codope these materials grown in MOCVD or HVPE systems. The concentration of background electrons was found, in one sample, to be  $-2.58 \times 10^{18} \text{cm}^{-3}$  as measured by low temperature Hall effect. EL determined the carrier type and I-V measurements determined the carrier concentration without ambiguity. There were no other known sources that could produce the band edge emission detected during EL, and the I-V experiments placed one of the samples' Fermi level very close to the valance band, indicating high carrier concentration p-type material. The EL measurement showed a bright band edge and blue luminescence, indicating the presence of magnesium in the p-type GaN template grown by MOCVD. There was also the same lumi-

nescence in samples grown by MEAglow at low temperatures, however the emission was heavily dominated by the yellow defect. The I-V experiment showed one sample had a net carrier concentration of  $9.9 \times 10^{16} \text{cm}^{-3}$ ; one was completely compensated; one was over compensated, and the last was too resistive to measure. Therefore, for the development of future GaN films, EL and I-V characterization is necessary.

## Chapter 4

# p-type GaN Film Development

High indium content InGaN is as a material solution for green emission in LEDs and laser diodes. More indium is conducive to changing the material's bandgap from one which corresponds to ultraviolet light to that which emits green. As a result, its emission is a candidate for the next generation of LCD backplanes and laser diode based projectors. As argued previously, with increasing indium content, GaN capping layers that preserve longer wavelength emission have to be grown at progressively lower temperatures. However, low temperature growth has the problem of lower quality p-GaN layers. Stoichiometry issues cause either gallium droplets or nitrogen rich conditions as depicted in Figure 2.4.

The attributes of low temperature grown GaN and how it affects the performance of LEDs and laser diodes is not common knowledge to the industry. Currently, most lighting devices are grown at high temperatures using MOCVD or HVPE, where any excess gallium would easily be desorbed as previously argued. Since metal rich conditions are not common, the effect of stoichiometry mismatches on LED quality is not well studied. Nevertheless, there are indications of the implications of these semiconductor imperfections on device performance. For instance, a gallium rich film has been shown to decrease the energy bandgap size in GaN [68]. Supposing the same holds true for InGaN, the emission wavelength of a QW LED is ultimately affected. Strongly gallium rich conditions are also undesirable when trying to grow smooth films. Any

layers placed atop a Ga rich film would be equally as rough due to the droplets below it. For the devices where low temperature grown GaN is not the final capping layer, this would be especially problematic. Therefore, the smoothest conditions, which happens to occur for only slightly gallium rich conditions, are usually sought.

With the confirmation of p-type conductivity in films grown ‘in house,’ and with the attainment of measurement methodologies to characterize the semiconductors, the film quality should then be assessed for the above aspects. The quality of the p-type layer will ultimately determine the viability of MEAgrow technology for these applications. For instance, when it was first presented that indium nitride could be grown using MEAgrow, the improved crystallinity and low surface roughness were emphasized to facilitate this method’s adoption [18]. Under this perspective, this chapter focuses on the development of higher quality p-GaN films for LED applications. First, it is determined how low of a temperature can be grown using the MEAgrow system. A set of growths were performed while varying the temperature to a sufficiently low level. Next, films in question were assessed both qualitatively and quantitatively using various instruments. Characteristics like material bandgaps; surface morphology; film thickness, and crystallinity were observed. Finally, a first attempt at optimizing the film quality is made to determine which parameters are important.

## 4.1 MEAgrow growth technology and conditions

One characteristic that differentiates one growth method from another is the source of each atomic species. HVPE uses halides such as  $\text{GaCl}_3$ , whereas MOCVD uses TMG. The unique characteristic of MEAgrow is its nitrogen source, the hollow cathode plasma source. As mentioned in section 2.4.2, nitrogen plasma can arrive at the semiconductor in either atomic or molecular form, and the latter is present in MEAgrow systems. The chamber pressure ensures there are many kinetic collisions, reducing the density of ionic species. Therefore, depending on one’s point of view, growth may benefit from this species type.

Even though the metal sources are the same as that found in MOCVD, their characteristics

are no less important. Gallium arrives at the reaction chamber as a TMG precursor molecule; indium comes as a trimethylindium (TMI) precursor, and magnesium does so attached to  $CP_2Mg$ . The flow of these, and also that of the nitrogen to the plasma source, is adjusted using mass flow controllers (MFC). These devices control the volumetric flow rate of each molecular source, and using the gas density allows the proportions to be specified. The advantage of the MEAgrow technique is that the MFC's are placed proximal to the output of the bubblers - the containers used to store and provide the metal vapours - and on the nitrogen tank line, allowing for individual control of source flows. See Figure 4.1 for a detailed diagram of the gas delivery system. Direct vapour injection can be used for TMG and TMI with the pressures in the chamber being  $\sim 1.0 Torr$ , while  $CP_2Mg$  is introduced with a nitrogen carrier gas flow to control the smaller source fluxes required. With these mechanisms, the proportions of TMG, TMI,  $CP_2Mg$  and nitrogen can be specified.

Equally as important as the flow system, the reaction chamber also exhibited a certain amount of control. The temperature was monitored using three sensors: a thermocouple placed below the sample holder, an infrared pyrometer measuring the sample holder temperature and another thermocouple in the main body of the chamber above the sample. The first of these was used in a feedback controller to maintain desired temperatures, and its value, when corrected using a calibration table, reflected the actual temperature of the sample substrate holder. Therefore, with this monitoring in place, an approximate substrate temperature during growth could be intentionally set and varied. Before gas begins to flow and growth occurs, the chamber pressure was brought to a low value ( $10^{-6} \rightarrow 10^{-8} Torr$ ) using a turbopump. As flow into the chamber begins, this chamber pressure will increase as a result, achieving a steady state balance with the turbopump. By using a bleed valve on the exhaust of the reaction chamber connected to a feedback control system, the chamber pressure can be maintained to a specification during growth, exerting some influence on the incorporation or desorption of atomic species in the semiconductor.

Procedures were in place to maintain the purity of the system. For one example, the sample is loaded using a load lock chamber that is also evacuated by a turbo pump before it is introduced in the chamber. This way, oxygen is practically evacuated so that it cannot contaminate the chamber upon loading. The metalorganics are also supplied in the purest form available. This in combination with a gas purifier ensures contaminants present in the chamber are mainly in the form of chemical reaction byproducts, not external species. If impurities build up over time, the system can be purged of contaminants. Particularly, this system is capable of growing InGaN, and the indium used rests on the walls and sample holder in the form of metal deposits. By flowing inert nitrogen or nitrogen plasma for several hours, the contaminants can be removed before growth. Lastly, the sample is placed on a rotating platform. If there are any spatial variations of the gas flow, its effect can be averaged over the entire film. With an eye for these implementation concerns, high quality films can be grown in the laboratory.

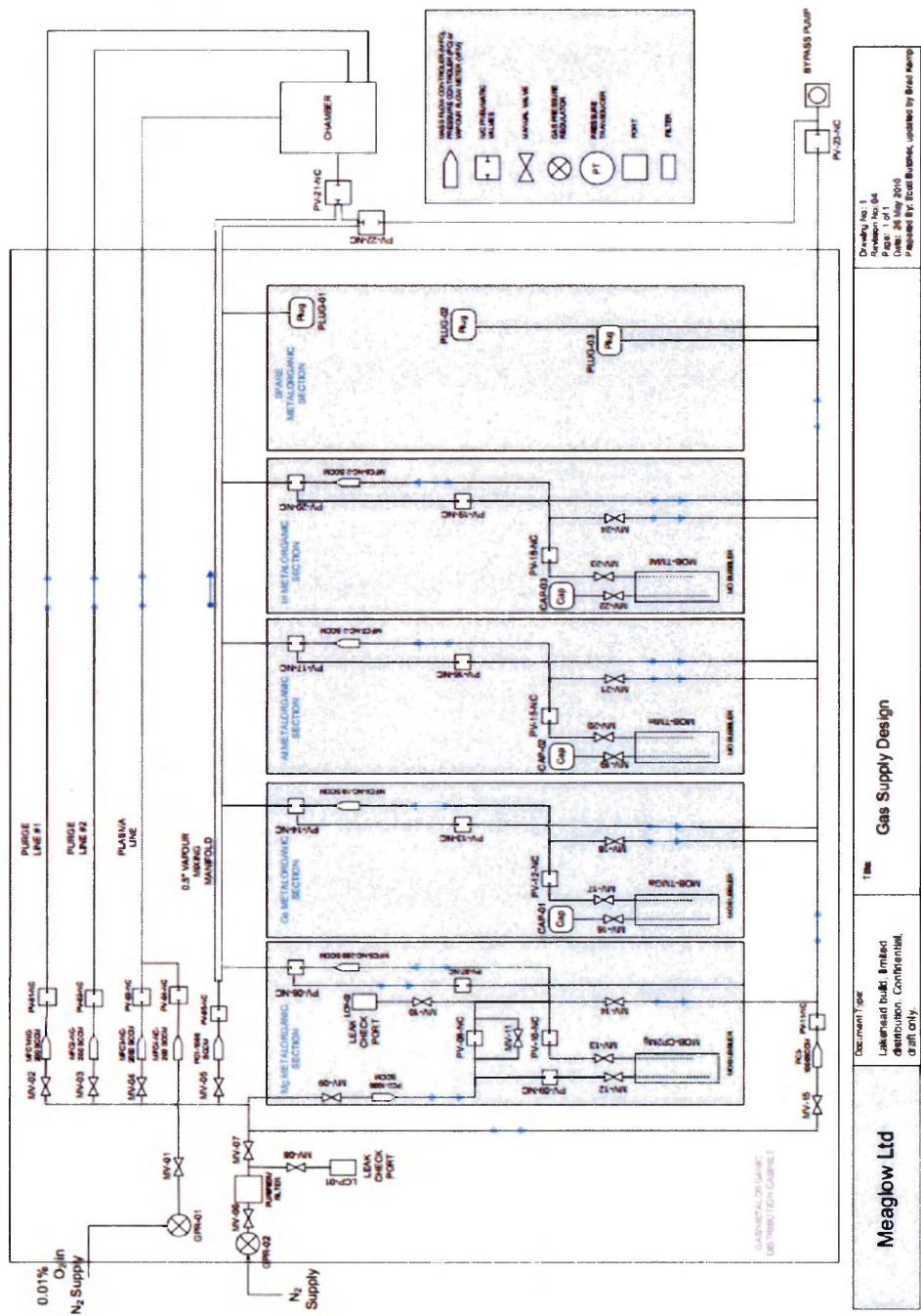


Figure 4.1: The gas flow system of the MEAglow reactor. Delivery systems for magnesium, gallium, indium and aluminum are in place with their flow constrained by the MFC. These gases are combined in a vapour mixing manifold before delivery to the chamber. A separate nitrogen plasma line provides the group-V species and two inert nitrogen “purge” lines alter the reaction chamber pressure or clear the metal organic lines before the start of growth. To ensure that none of the purging sends gas into the reaction chamber, a bypass line is used that does not flow through the growth environment.

### 4.1.1 Growth Procession

The parameters listed above (nitrogen, plasma, TMG and CP<sub>2</sub>Mg flow rates, pressures, temperatures, etc.) are carefully chosen. They control stoichiometry, growth conditions and manufacturing equipment related operation. However, as indicated in chapter 2, growth of GaN does not occur in one state for the entire time. A nucleation step, a metal modulation step and a magnesium thermal activation step are all incorporated in the growth procession. Therefore, there are a multitude of parameters at different times to be set. Those used for the growth of the low temperature magnesium doped GaN, studied in this work, are shown in the timing diagram of Figure 4.2.

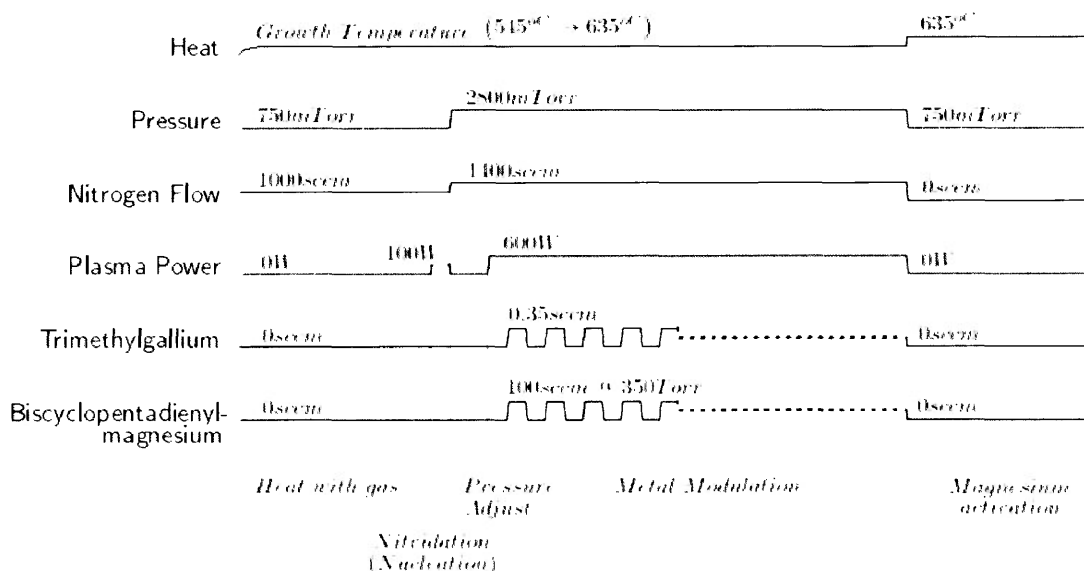


Figure 4.2: The timing sequence for the growth of low temperature magnesium doped GaN (time axis not to scale). The growth recipe involves a heating stage, a nucleation period, a pressure adjust stage where time is given for chamber stabilization, the metal modulated growth of the GaN film, and a magnesium thermal activation period. Except for the activation stage, nitrogen flows through the plasma line at all times, but plasma is present only when the plasma RF voltage is applied.

To begin, a heating stage brings the temperature of the sample to the desired level. Meanwhile, inert nitrogen gas flows to clear the surface of the sapphire substrate from any contaminant molecules such as water vapour or hydrocarbons from prior atmospheric exposure. After the system reaches thermal equilibrium, the sapphire is nitrogenated with a weak plasma for one minute to form the aluminum nitride seed layer. Afterward, the plasma is turned off and the system is adjusted to the desired pressure for growth. Since this is the stage where temperature feedback control is initiated, a generous three minutes is given for stabilization. Metal modulation then begins. A cycling between a period of 12.5 seconds of nitrogen plasma only and a 15 second period of plasma, TMG and  $\text{CP}_2\text{Mg}$  flow occurs. This is done for four hundred cycles, marking the end of film growth. Afterward, the semiconductor is exposed to heat at  $630^\circ\text{C}$  for one hour to remove the hydrogen bonds from the magnesium, activating the acceptors. The total growth time is exactly 5 hours.

## 4.2 Experimental Fabrication of Magnesium Doped GaN for Analysis

The ability to grow p-type layers for QW LEDs that do not cause decomposition of the indium underneath was assessed. Indium significantly decomposes from InGaN around  $600^\circ\text{C}$  as previously mentioned. In this regard, four different films were grown, each at a different chamber temperature ( $545^\circ\text{C}$ ,  $580^\circ\text{C}$ ,  $600^\circ\text{C}$  and  $635^\circ\text{C}$ ). This selection reflects the temperature at all periods of the film growth except the stage of thermal magnesium activation at the end. Two extra p-GaN films were grown as preliminary experiments to gauge and optimize the experiment, one at  $545^\circ\text{C}$  and the other at  $635^\circ\text{C}$ . Since it was determined that the growth parameters were adequate as a starting point for further optimization, these samples had the same growth parameters as those above, and hence extra data points were present. Finally, one sample acting as a control experienced the same growth parameters, but the magnesium flow was set to zero. Thus, the effect of magnesium addition could be gauged.

The substrates used were 1/4 sections of a sapphire disk having a 2 inch diameter. This sapphire was  $0.33\text{mm} \pm 0.03\text{mm}$  thick and was oriented along the (0001) axis. GaN grown on

this orientation should have Wurtzite (hexagonal) crystal habit. Prior to loading in the growth system, the sapphire was baked at  $1050^{\circ}\text{C}$  for 20 minutes to remove hydroxides, reduce polishing damage by the manufacturer and to remove surface hydrocarbons. The substrate was placed on the sample holder within an alumina disk and adjacent to sapphire covers used to lower the local surface temperatures of the sample holder and prevent previously deposited atomic species on the otherwise hotter sample holder from affecting the sample edges (Figure 4.3).

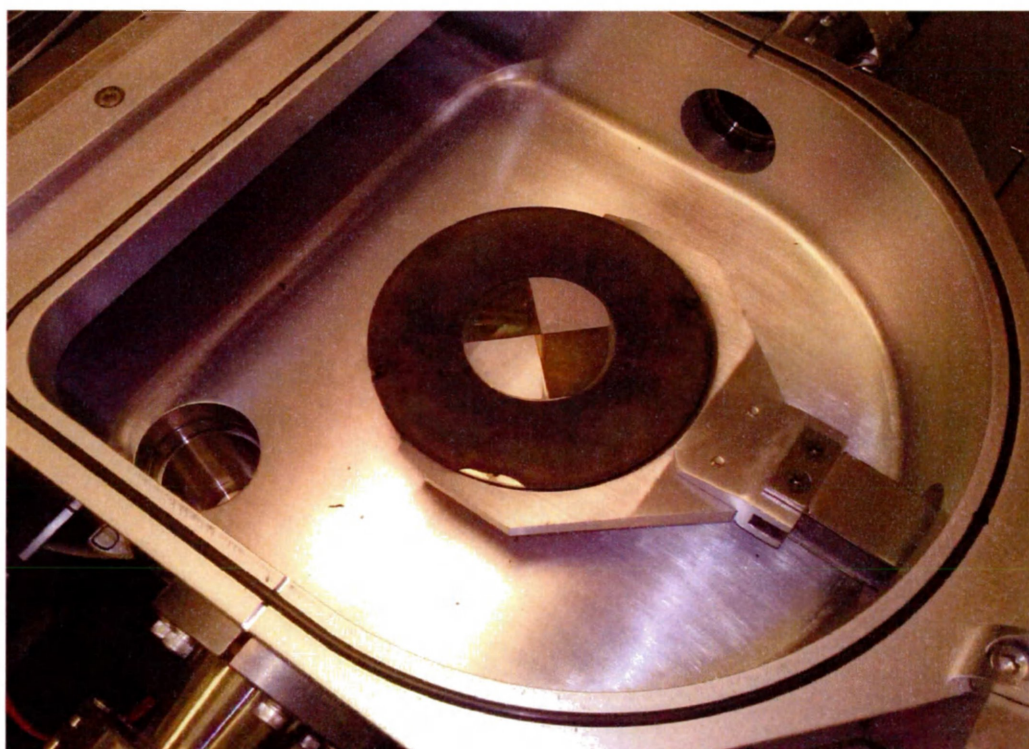


*Figure 4.3: The placement of the sapphire substrates (clear  $\frac{1}{4}$  wafer sections) in proximity to the surrounding aluminum disk and extra sapphire covers (discarded GaN samples, dark  $\frac{1}{4}$  wafer sections). The configuration is expected to act to lower temperature and prevent atomic deposition from the sample holder.*

The flow rate of the nitrogen through the plasma head was 1000sccm (standard cubic centimeters per minute<sup>1</sup>) during the nucleation stage and 1400sccm during the growth, with an

---

<sup>1</sup>Standard cubic centimeters per minute is the flow rate under standard conditions,  $0^{\circ}\text{C}$  and  $1\text{atm}$ .

applied plasma power of 100 and 600 Watts respectively. Given the density and molecular weight of molecular nitrogen gas ( $0.00125g/cm^3$  and  $28.02g/mol$  respectively), this corresponds to a molecular flow rate of  $62.5 \times 10^{-3}mol/min$ . The flow rate of TMG was 0.35sccm, whose density ( $0.385g/min$ ) and molecular weight ( $114.83g/mol$ ) resulted in a molecular flow rate of  $3.35 \times 10^{-3}mol/min$ . Although the molecular flow rates are not equal, not all nitrogen that flowed from the plasma source was in the form of chemically active species. In previous experiments growing undoped GaN, this excess of nitrogen delivery was found to provide an approximate 1:1 stoichiometric ratio between the two.

The magnesium flow rate was calculated as follows.  $CP_2Mg$  partial pressure is a strong function of the temperature, and adheres to the relationship

$$\text{Log}_{10}(P_{CP_2Mg}) = 10.452 - \frac{3522}{T} \quad (4.1)$$

where  $P_{CP_2Mg}$  is in Torr and  $T$  is in Kelvin. The temperature of the gas line is set to  $40^\circ C$ , thus the partial pressure becomes  $0.158 \text{ Torr}$ . Since the carrier gas,  $N_2$ , is set to  $350 \text{ Torr}$  and is flowing at 100sccm, the resulting volumetric flow rate is scaled by the proportion of partial pressures,

$$\dot{M}_{CP_2Mg} = \frac{P_{CP_2Mg}}{P_{N_2} + P_{CP_2Mg}} \cdot \dot{M}_{line} = 4.53 \times 10^{-3} \text{ sccm} \quad (4.2)$$

where  $\dot{M}_{CP_2Mg}$  is the mass flow rate of  $CP_2Mg$  and  $\dot{M}_{line}$  is the mass flow rate of the  $N_2 - CP_2Mg$  mix set to 100sccm by the MFC. Using the density and molecular weight of  $CP_2Mg$  ( $1.1g/cm^3$  and  $154.49g/mol$  respectively), its molecular flow rate is then  $0.322 \times 10^{-3}mol/min$ , or 10.4% that of TMG.

### 4.3 Film Investigation through Scanning Electron Microscopy (SEM)

To better understand the qualitative growth characteristics of the film, visualization is helpful. However, since some of the film structures of interest are small, possibly less than 10nm, optical

microscopy has an insufficient resolution because of the limits inherent to the aperture size of lenses. Though other modes of imaging are possible to obtain a finer resolution, most commonly an electron microscope is used. A scanning electron microscope (SEM) image most commonly represents the secondary electrons collected by a detector from an incident electron beam. The mechanisms behind this secondary electron generation is from electron excitation of large energy orbitals ( $<50\text{eV}$  [69]); electron sources larger than this are filtered out. The image formed is different from that of optical microscopy. In SEM, atoms a few hundred nanometers from the incident surface emit electrons, which are accelerated toward the detector. Therefore, the electron microscope images presented here reflect the electron absorption and reemission properties of the materials at hand, and not necessarily their optical brightness as in photography - although, the contrast between structures is usually large enough to look like the material itself.

The grown films were sectioned and placed on a sample holder designed for use in the scanning electron microscope. The newly broken edge of the film was placed toward the imaging secondary electron sensor as depicted in Figure 4.4. A small amount ( $\sim 0.1\text{mL}$ ) of conductive carbon paint provided an electrical connection to the grounded holder so that incident electrons do not become trapped in the film, causing surface charging effects. In order to determine the film thickness, the sample was scanned in a region which visibly exposes the interface between the sapphire and semiconductor. Afterwards, the sample was placed such that the detector was in line with the (0001) axis (the film side). Images of the cross sections and film surfaces are shown below in Figure 4.5 and 4.6, and the measured film thickness from the former figure is shown in Table 4.1.

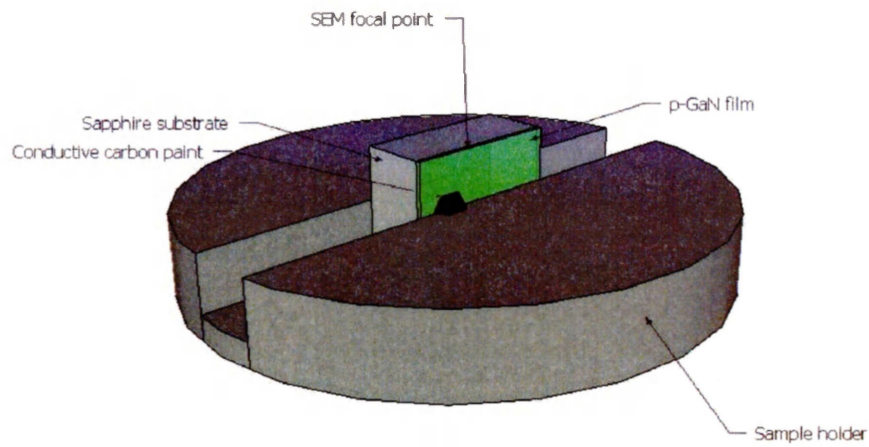


*Figure 4.4: Preparing the sample in its holder for SEM scanning of the film's edge. A small section of the substrate and film are placed in between two circular plates, holding the edge of the film toward the secondary electron detector.*

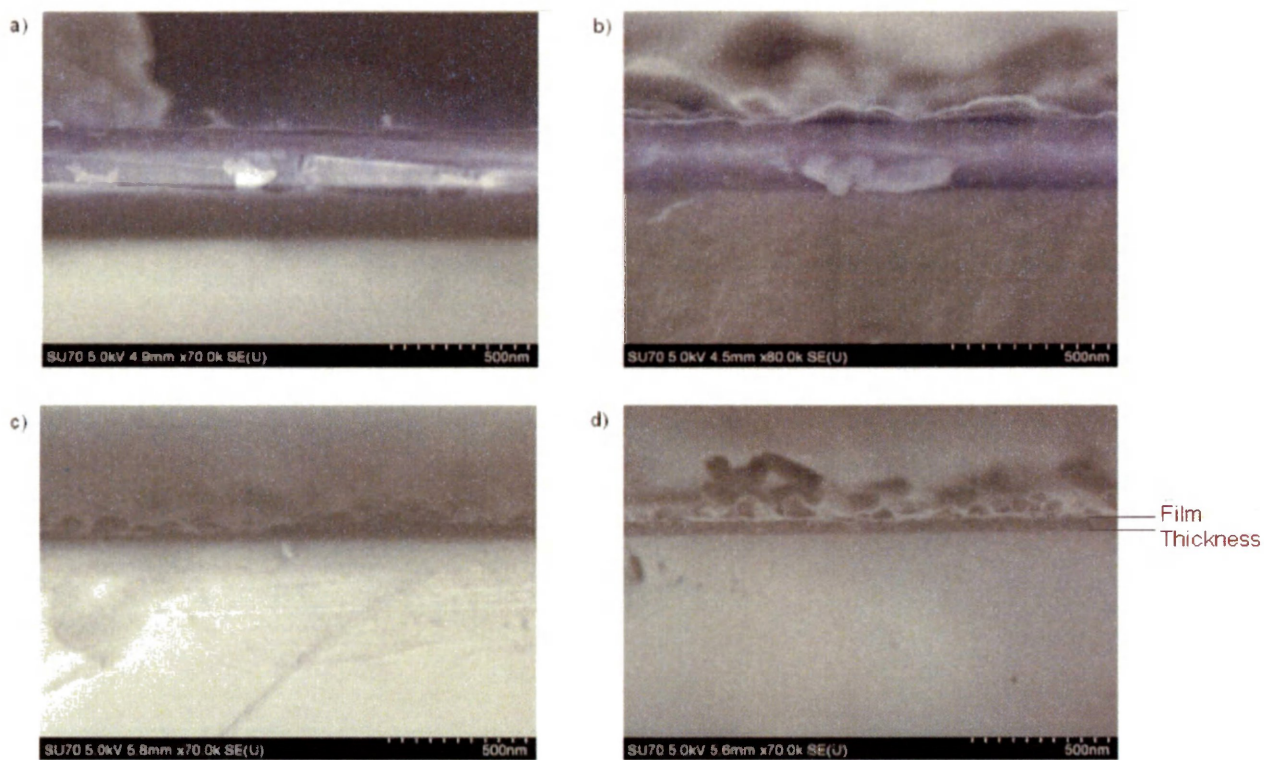


*Figure 4.5: Cross sectional scanning electron microscope images. Films were grown at a) 545°C, b) 580°C, c) 600°C, and d) 635°C. Each image was taken at approximately the same magnification, but the film thicknesses were different. In profile, films look continuous rather than columnar.*

Table 4.1: Film thickness of magnesium doped GaN grown by low temperature MEAgrow.

Growth temperature ( $^{\circ}\text{C}$ )	Film thickness (nm)
545 ( <i>sample 1</i> )	325
545 ( <i>sample 2</i> )	145
580	270
600	120
635 ( <i>sample 1</i> )	80
635 ( <i>sample 2</i> )	65
<i>Undoped</i> (580)	47

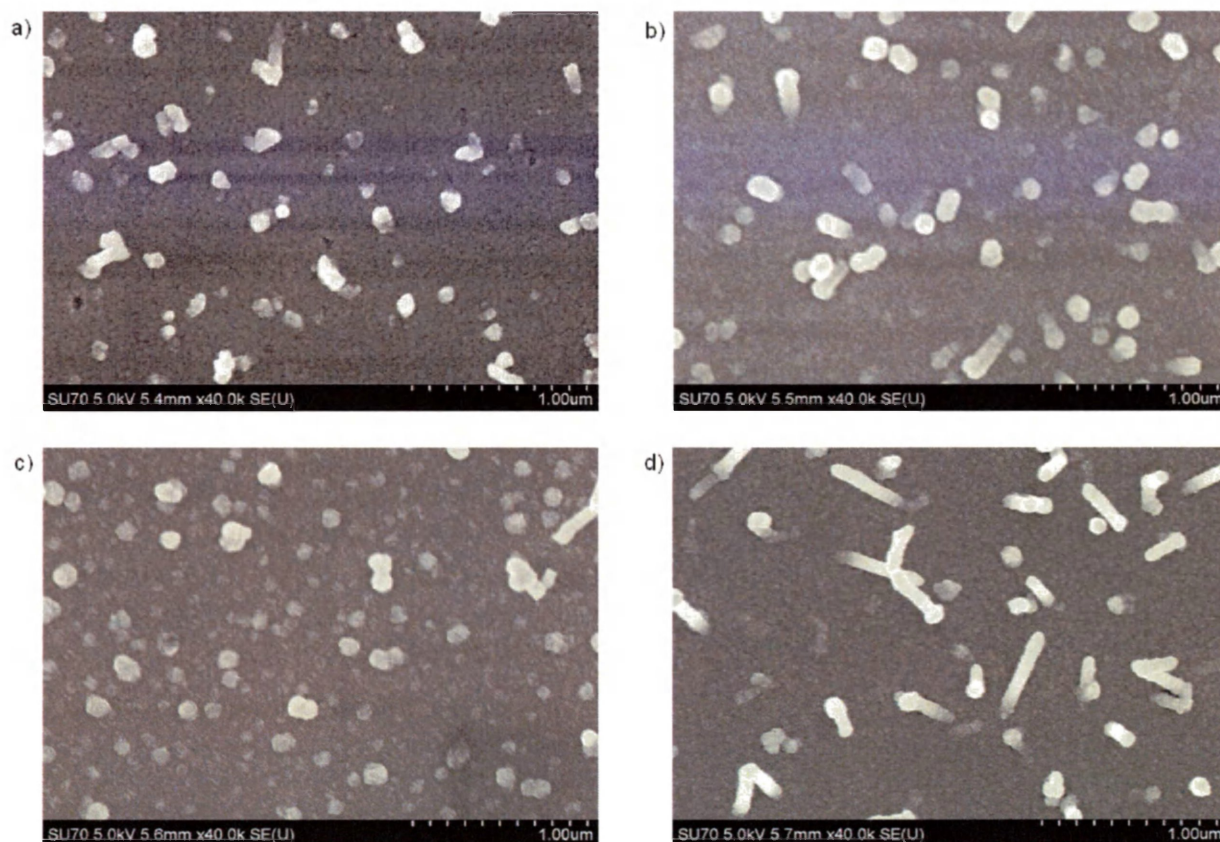


*Figure 4.6: Surface SEM images of magnesium doped GaN samples grown by low temperature MEAgrow. Films were grown at a) 545<sup>o</sup>C, b) 580<sup>o</sup>C, c) 600<sup>o</sup>C, and d) 635<sup>o</sup>C. In addition to metal droplets, there is the presence of nanowires.*

The cross-sectional images from Figure 4.5 showed smooth films with the presence of nanostructures on top. Since many of these entities were not in the images focus, the surface images (Figure 4.6) are better for showing that nanowires are present. Nanowires form from a seed of metal that is nitrated while additional gallium diffuses to the apex to form a longer structure. Since no seed was intentionally placed on the film, the growth conditions are such that these wires form spontaneously.

The film thickness decreased as the temperature increased. This is consistent with gallium desorption occurring inside the vacuum, and since all growths lasted for the same length of time, this indicates that growth rates suffered at higher temperatures. Under this desorption model,

if growth was desired at higher temperatures, different growth conditions, like an overpressure of source molecules, would be necessary. A plot of film thickness is shown below in Figure 4.7. The estimated error as observed by the images is included in the figure, however the film thickness could vary depending on the focal point along the long film edge, adding extra variability. Some data points were omitted from the plot. One of the samples grown at  $545^{\circ}\text{C}$  had an uncharacteristically low film thickness. By observing its surface image (Figure 4.8a), it was found this outlier had a high density of large nanowires. Since spontaneous formation of nanowires happens by metal diffusion away from the film, the thickness suffers, and hence the sample was removed from the plot. On this note, the second sample grown at  $635^{\circ}\text{C}$  also had a high density of nanowires compared to the first sample (Figure 4.8b) and had a slightly lower film thickness. Being consistent, this second sample was omitted as well.

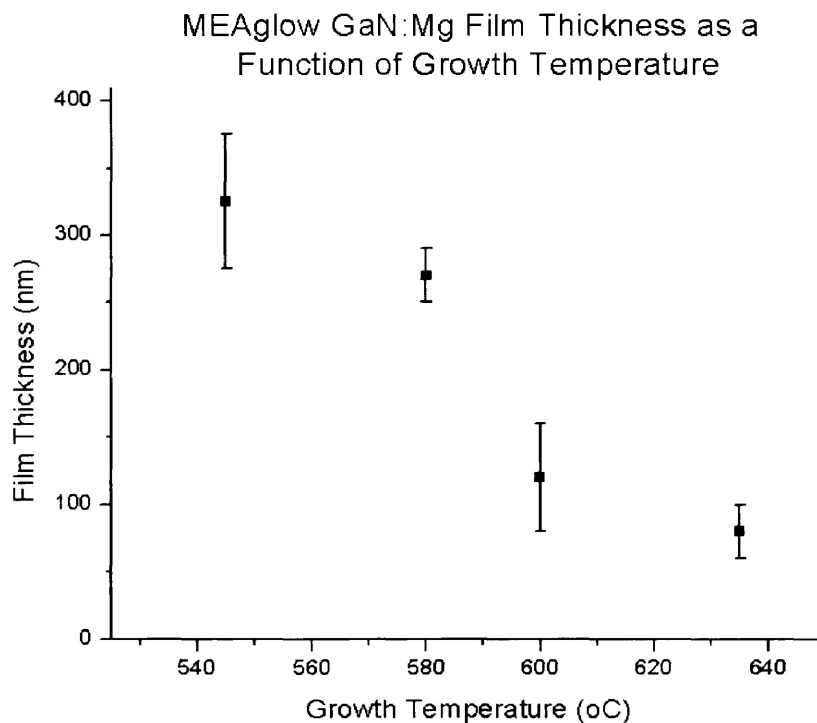


*Figure 4.7: A plot of the film thickness versus the growth temperature. The graph shows a downward trend. Error bars were estimated from the individual images themselves.*

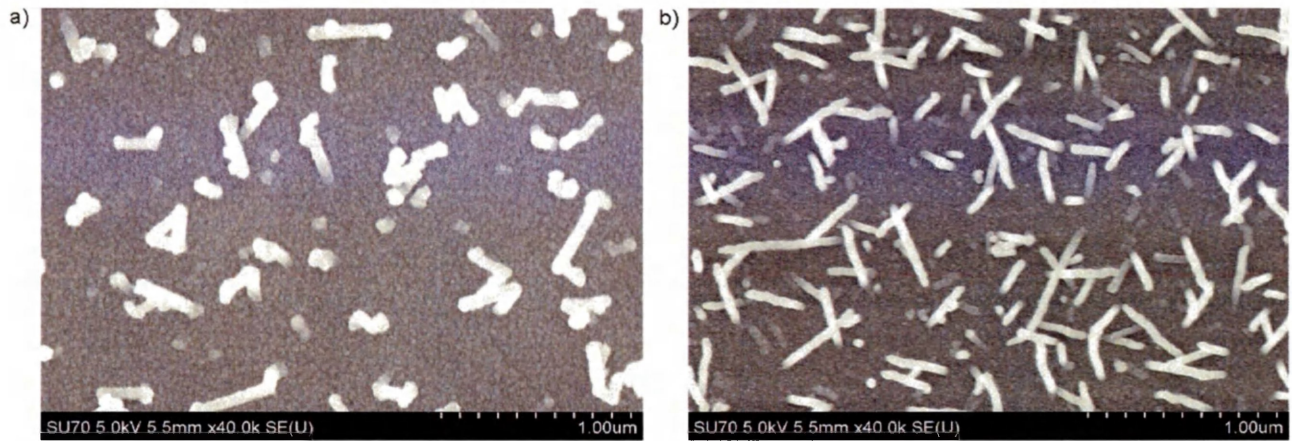


*Figure 4.8: Surface SEM images of two samples that had uncharacteristically large densities of nanowires as compared to their counterpart samples, grown at the same temperature: a) Sample grown at  $545^{\circ}\text{C}$  and b) sample grown at  $635^{\circ}\text{C}$ . The counterpart samples in question are Figure 4.6a and 4.6d respectively.*

The cross-sectional SEM images show films that are very smooth. GaN has a tendency to have a columnar structure like that of Figure 4.9. At low temperatures, GaN usually grows according to the Stranski-Krastanov growth model, incorporating both layered and island growth [26]. The result is a cross section that is not as smooth. These films, on the other hand, have relatively pristine cross sections, which would do well in device integration; they would be good base layers for additional epitaxy. Ironically, while the nanowires present would hamper the growth of an epilayer, they do have some peculiar optical properties, for instance their low defect crystalline structure provides waveguides, optical confinement and lasing emission [70]. So, even though the nanowires are not desired in quantum well LED applications, they still may be useful.

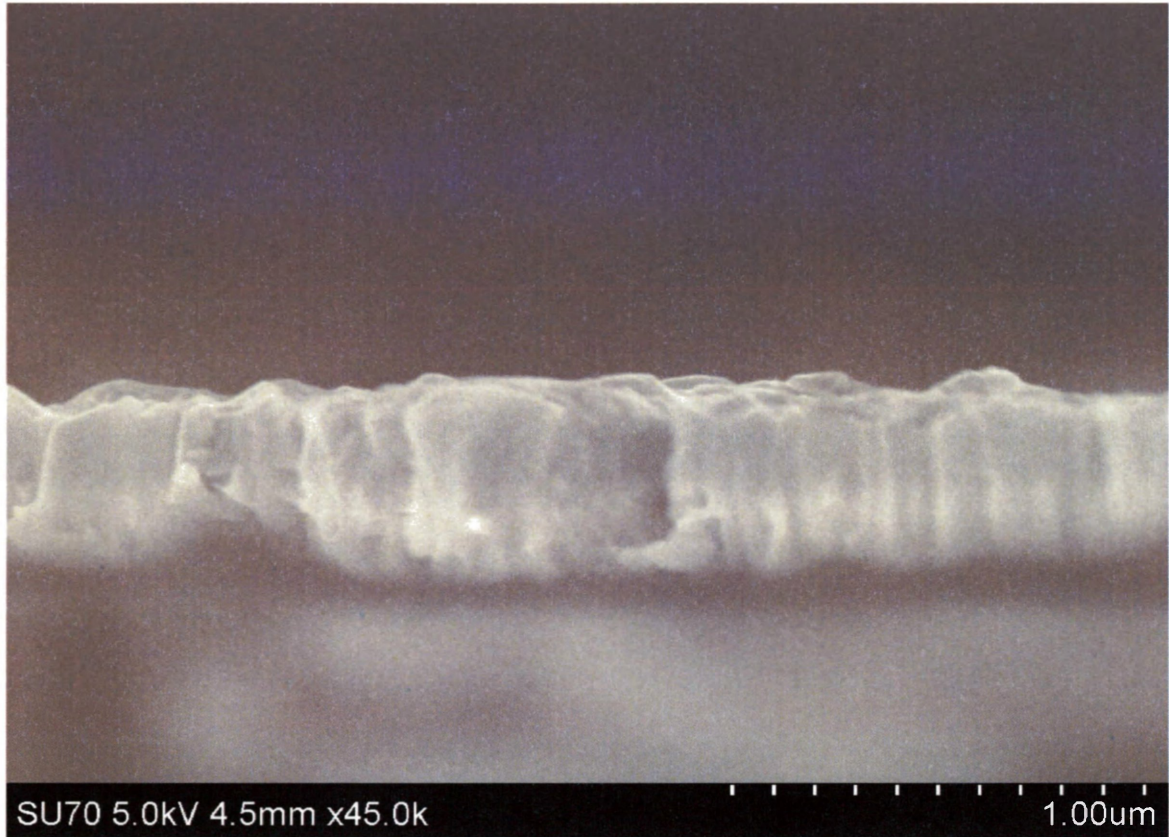


*Figure 4.9: SEM image of InN grown by MEAglow. Here, the vertical columnar structure is evident.*

#### 4.4 Film Investigation through Atomic Force Microscopy (AFM)

Atomic force microscopy measures the deflection of a probe placed close to the semiconductor surface due to Van der Waals forces. A laser aimed at the probe will reflect in different directions depending on the degree of probe deflection. As the probe traverses the sample in a rectilinear fashion, the detector records the amount of deflection at each point, generating an image in the process (Figure 4.10). Films were scanned in such a system (Nanosurf 'Easyscan 2') using an ACL-A probe<sup>2</sup> in non-contact imaging mode. The system was placed in a sound proof chamber with a vibrational isolating stage to dampen outside disturbances. To make imaging faster, the probe is allowed to undergo free vibration at its resonance frequency. Known as Dynamic Force

<sup>2</sup>225 × 40 × 8.5 μm dimensions with a vibrational frequency of about 190 kHz

imaging as opposed to Static Force, a probe more proximal to the surface vibrates with a lower amplitude. By sampling this amplitude at a regular interval, the probe can move constantly, increasing the scanning speed. A caveat to this, however, is that imaging parameters then become more important. The probe is controlled to be a certain distance from the surface using a PID<sup>3</sup> device. If these parameters are not stable given the scan speed and surface morphology, the image may not reflect the true surface.

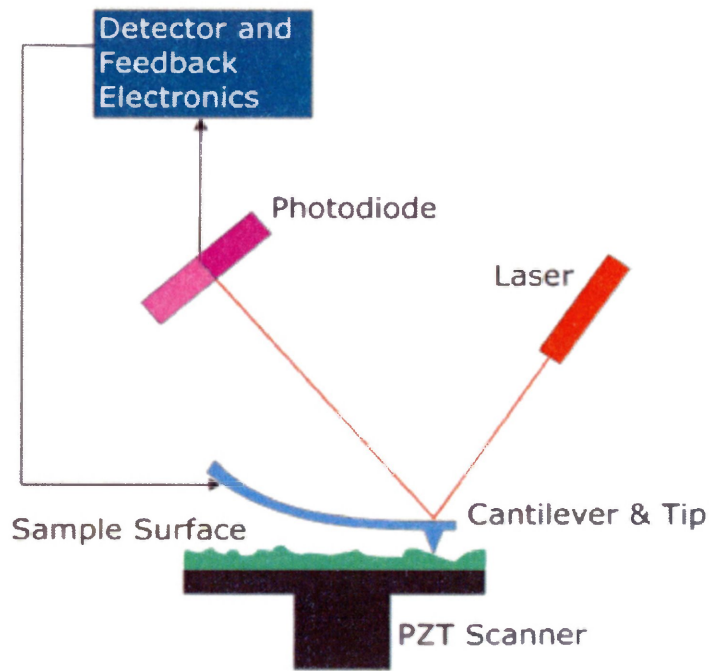


*Figure 4.10: Diagram of the functional setup of the atomic force microscopy operation. Probe proximity to the sample surface deflects the probe, and the deflection detected indicates the surface height. Figure taken from [71].*

Measurements taken here have revealed much about the growth of GaN. Below in Figure 4.11 are three AFM images of commercially available magnesium doped, undoped and silicon doped GaN grown by HVPE. Images were  $8 \times 8 \mu\text{m}$  large at a resolution of  $512 \times 512$ . The probe was

<sup>3</sup>Proportional, Integral, Differential controller

set to vibrate at an amplitude 50% of its 100mV free vibration as determined by the detector, giving an optimal range on both sides of the set point. Two prescan lines were made, one in the x direction and one in the y to gauge the average slope of the surface; a linear amplitude removal technique was employed to account for the offset. The probe moved across the surface at a speed of  $2\mu\text{m}/\text{s}$ . A  $6 \times 6\mu\text{m}$  region of interest (ROI) was placed at the centre of the image and the average roughness of the surface amplitude, measured root-mean squared (RMS) was 4.67nm, 1.37nm and 1.24nm for the magnesium doped, undoped and silicon doped samples respectively.

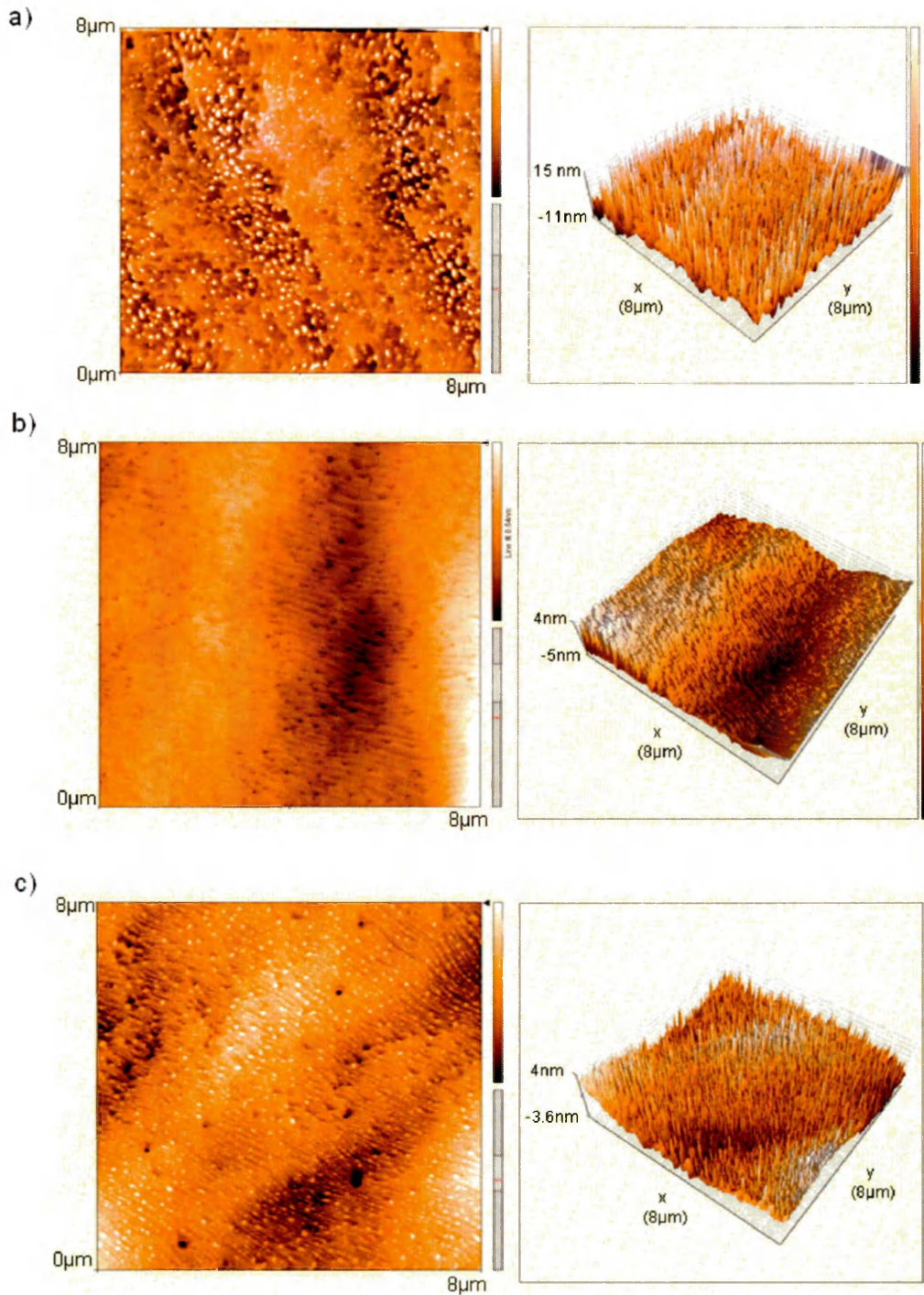


Figure 4.11: AFM images of a) magnesium doped, b) undoped, and c) silicon doped GaN grown by HVPE. Samples doped (with either silicon or magnesium) showed many surface defects, whereas the undoped sample showed terracing.

Figure 4.11 shows two phenomena about GaN surface morphologies. Those doped (by either magnesium or silicon) showed many defects on the surface. The height of these formations are small, not exceeding 20nm in scale, allowing the surface to be relatively smooth as given by the RMS surface roughness. On the other hand, the predominant feature of the undoped sample is surface terraces. Atoms to be incorporated in the lattice often times need to diffuse across the surface to fill the monolayer adjacent to it. These terraces are indications that lateral, 2D growth is occurring rather than 3D island growth. For examination, AFM images of the films grown by low temperature MEAgrow were acquired. These are shown below in Figure 4.12.

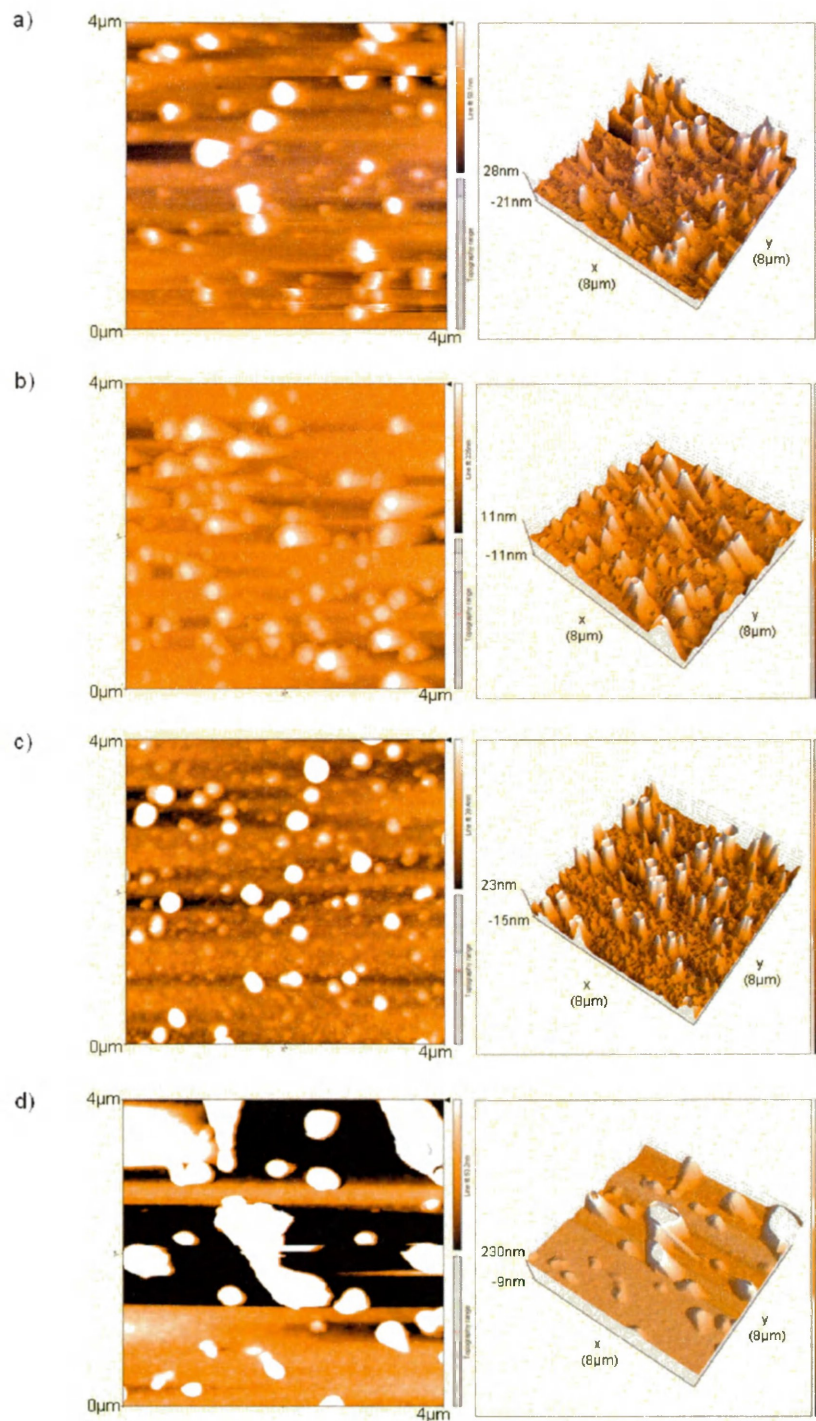


Figure 4.12: AFM images of the magnesium doped GaN films grown using low temperature MEAgrow. Films were grown at a)  $545^{\circ}\text{C}$ , b)  $580^{\circ}\text{C}$ , c)  $600^{\circ}\text{C}$ , and d)  $635^{\circ}\text{C}$ . There is evidence of metal rich structures including the large pillared structures.

What is evident is the plethora of surface defects. There are surface defects that can be larger than 400nm in width and  $1\mu m$  (the range of the detector) in height. This may be due to gallium droplets forming on the surface, which is commonly experienced for this type of film growth. Further, the shadow region - the area in the x-direction scanned immediately after the defects - show irregular readings. This could be because the probe tip gets momentarily wetted. Gallium is a liquid at room temperature, and if the probe touches this, its vibration would drastically change. To verify this, two samples were etched in a HCl:H<sub>2</sub>O mixture (1:3) for five minutes and rescanned. The etching should remove all liquid gallium from the surface, reducing the surface defects. Contrariwise, the surface did not change after etching. One possible explanation could be that these droplets have been nitrided, and are not liquid. Instead, their structure would remain after etching. This explains the surface structures observed in SEM images.

The surface roughness for these samples is displayed in Table 4.2. The surface morphology shows a weak correlation with luminosity in LED applications. The p-GaN sample with the highest electroluminescence had the highest roughness. As the surface becomes rougher, there is less total internal reflection of the light, allowing more extraction. Therefore, this type of surface may have facilitated brighter EL. Root-mean-squared surface roughness, however, may not be the best parameter to gauge. Nanostructures and nanowires increase the RMS value, but do not necessarily increase light extraction. Therefore, surfaces like that shown in Figure 4.6d may still be smooth and retain light, but still have rough features. It is evident that these growths were not optimized for higher surface roughness. The surface of the undoped sample (with zero magnesium flow) had a higher RMS roughness than the magnesium doped samples. While no insight can be given as to why this is, this high number indicates that the conditions were not fully optimized for GaN growth, let alone p-GaN fabrication.

Table 4.2: The surface roughness of magnesium doped GaN samples grown by low temperature MEAgrow.

Growth Temperature ( $^{\circ}C$ )	Surface Roughness ( $nm$ , $RMS$ )
545	15
580	11
600	17
635	9
Undoped (580)	23

## 4.5 Gallium Nitride Bandgaps

The bandgap of GaN in the Wurtzite configuration is well reported as  $3.42\text{ eV}$  [44]. This is the distance between the conduction and valence levels of the  $\Gamma$  point in the Brillouin zone, as seen in Figure 4.13, and can be measured using a transmission spectrophotometer. As the wavelength of the photon decreases, its energy approaches the bandgap energy, resulting in a photoelectric interaction with the semiconductor. Hence, the bandgap energy should correspond to where the optical spectrum abruptly changes. Transmission spectra were obtained using a UV-Visible-Infrared spectrophotometer (Varian Cary5e). A spectral sweep between 190nm and 3300nm was performed at a resolution of 1nm. Baseline scans of 0% transmission (light blocked) and 100% transmission (sapphire substrate only) were performed prior to measuring the film to determine the expected range of intensity at the detector. Samples were then placed in the enclosed spectrophotometer to be probed as shown in Figure 4.14, and the transmission vs. wavelength relation was obtained.

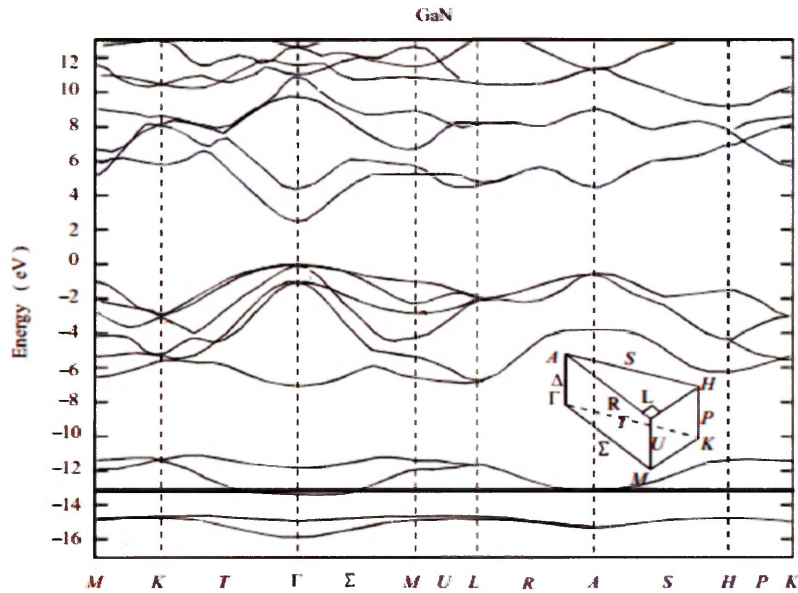


Figure 4.13: The calculated band structure of gallium nitride. The minimal energy transition between the  $\Gamma$  apexes is known as the bandgap (3.42eV). The Brillouin zone used for the calculation is also included. Figure taken from [44].

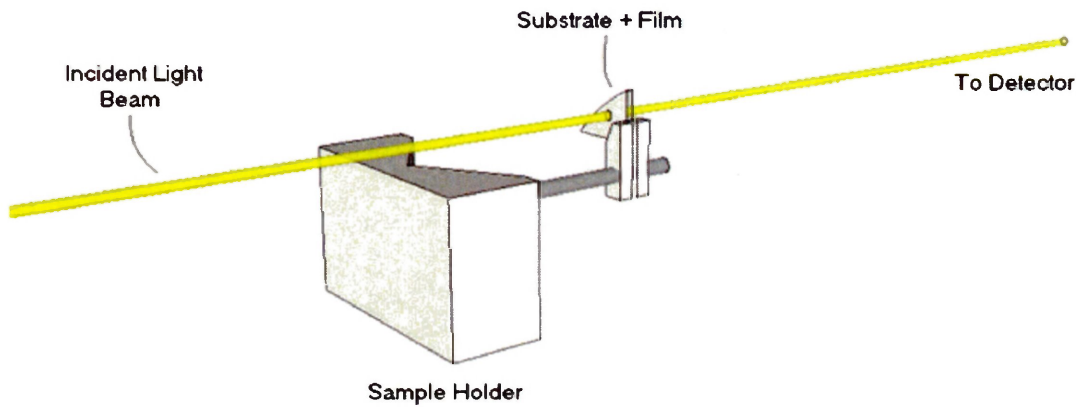


Figure 4.14: The probing of the spectrophotometer. A sample holder places the film toward the light beam and the detector measures the attenuated beam.

An example of the transmission spectrum from magnesium doped GaN grown by HVPE is

shown in Figure 4.15. Here, there is an abrupt transition at around 360nm, which corresponds to the 3.4eV bandgap energy. The change at 800nm is an instrumental effect resulting from the transition between infrared and optical detectors. It is noted that the transmission was recorded to be larger than 100%. To explain why, a blank sapphire sample was used as a calibration tool so that the effect of the semiconductor only is shown. A thin enough sample of blank sapphire was not available, thus more light was detected when scanning the film than when acquiring the baseline calibration. Finally, the spectrum contains an oscillation. This is due to the Fabry-Pérot cavity in the film itself, whose structure is shown in Figure 4.16. A standing wave is formed within the GaN film, and if the incident beam and reflected ones are half wavelength multiples of each other, constructive interference will occur and a large amount of light transmits. Conversely, if they are odd multiples of quarter wavelengths, destructive interference occurs. Hence, the following relationship holds for the transmission coefficient,  $T$ :

$$T = \frac{1}{1 + F \cdot \sin^2(\delta/2)} \quad (4.3)$$

where  $F = 4R/(1 - R)^2$  is the finesse of the resonator,  $R$  is the assumed equal reflection coefficient at the film boundaries,  $\delta = \frac{2\pi}{\lambda} \cdot 2nl$  is the optical path length difference in number of wavelengths between the two coincident reflections,  $n$  and  $l$  are the order of the wave and the cavity length respectively. By performing calculations on the spacing, the film thickness can be obtained. Choosing two adjacent maxima,  $m$  and  $m + 1$ , the difference in their optical path length is

$$\delta_{m+1} - \delta_m = 4\pi l \cdot \left[ \frac{m+1}{\lambda_{m+1}} - \frac{m}{\lambda_m} \right] = \frac{1}{2} \quad (4.4)$$

which yields the result for the film thickness:

$$l = \frac{1}{8\pi} \left[ \frac{\lambda_{m+1}\lambda_m}{(m+1)\lambda_m - m\lambda_{m+1}} \right]. \quad (4.5)$$

This approach was used to determine the film thickness of the sample scanned in Figure 4.15. By averaging four different pairs of maxima, the film thickness was determined to be  $1.89\mu m$ , which is close to the manufacturer specified value of  $2\mu m$ .

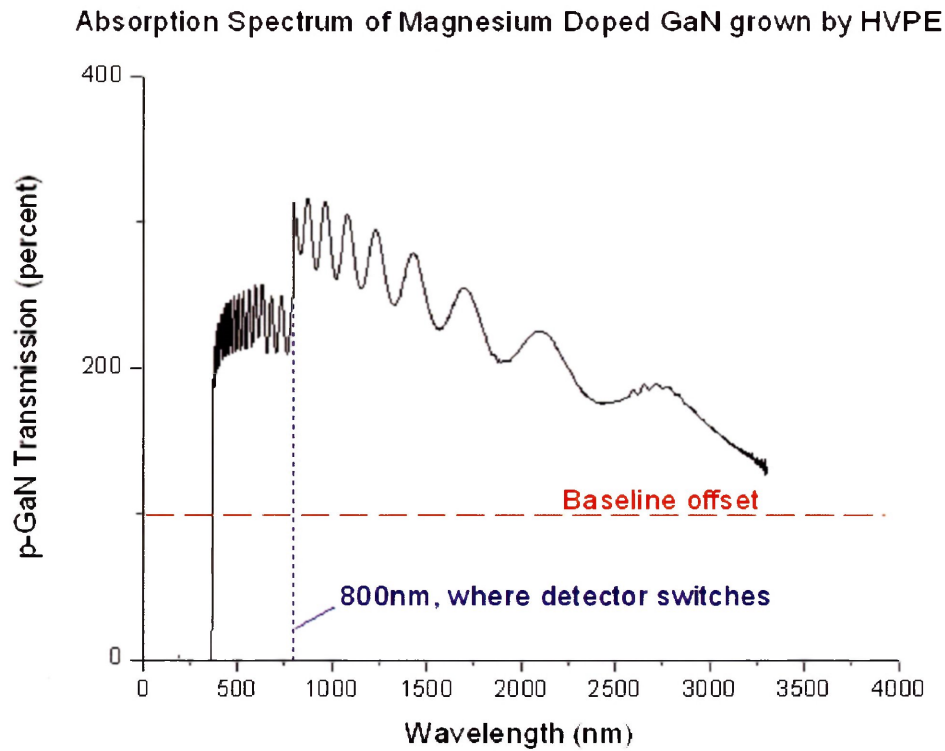


*Figure 4.15: Transmission spectrum of magnesium doped GaN grown by HVPE. Here, the band edge happens around 360nm, indicating the appropriate bandgap energy. Transmission was measured to be greater than 100% because the sapphire substrate was smaller than that used for calibration.*

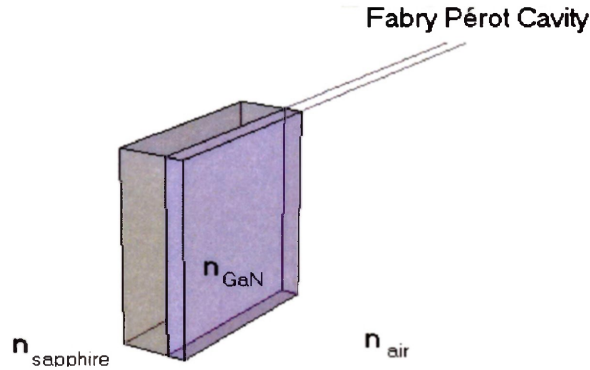


*Figure 4.16: The formation of a Fabry-Pérot cavity from the GaN film. Light passing through the sapphire and then the GaN film resonate between their boundaries, forming interference fringes.*

It is important to know the band edge transition is not abrupt, and different processes can confound the result. First of all, the absorption of direct bandgap semiconductors follows a square root law<sup>4</sup>, as per [72]:

$$\frac{\alpha}{\alpha_o} = (h\nu - E_g)^{\frac{1}{2}} \quad (4.6)$$

where  $\alpha/\alpha_o$  is the normalized absorption through a semiconductor film, and  $h\nu$  is the photon's energy. The reason why this is not apparent in Figure 4.15 is that the span of the graph is so large that it appears as a straight, vertical line. In fact, the graph needs to be linearized as

$$\alpha^2 \propto (h\nu - E_g) \quad (4.7)$$

and hence the x-intercept of the  $\alpha^2 \leftrightarrow h\nu$  graph gives the bandgap energy. Making things more complicated, one other phenomenon skews the above square root relationship. There is an Urbach tail in the spectrum. This characteristic is associated with impurity defects below the

---

<sup>4</sup>This exponent changes to 2 for indirect bandgap semiconductors, which states that whatever absorption can occur through the semiconductor will happen near the bandgap energy, and decreasing the wavelength will not improve the attenuation much.

band edge. For GaN, a second Urbach region can be associated with the surface oxide, interacting with photon energies slightly above the bandgap as well [50]. As a result, the absorption spectrum is graded as shown in Figure 4.17.

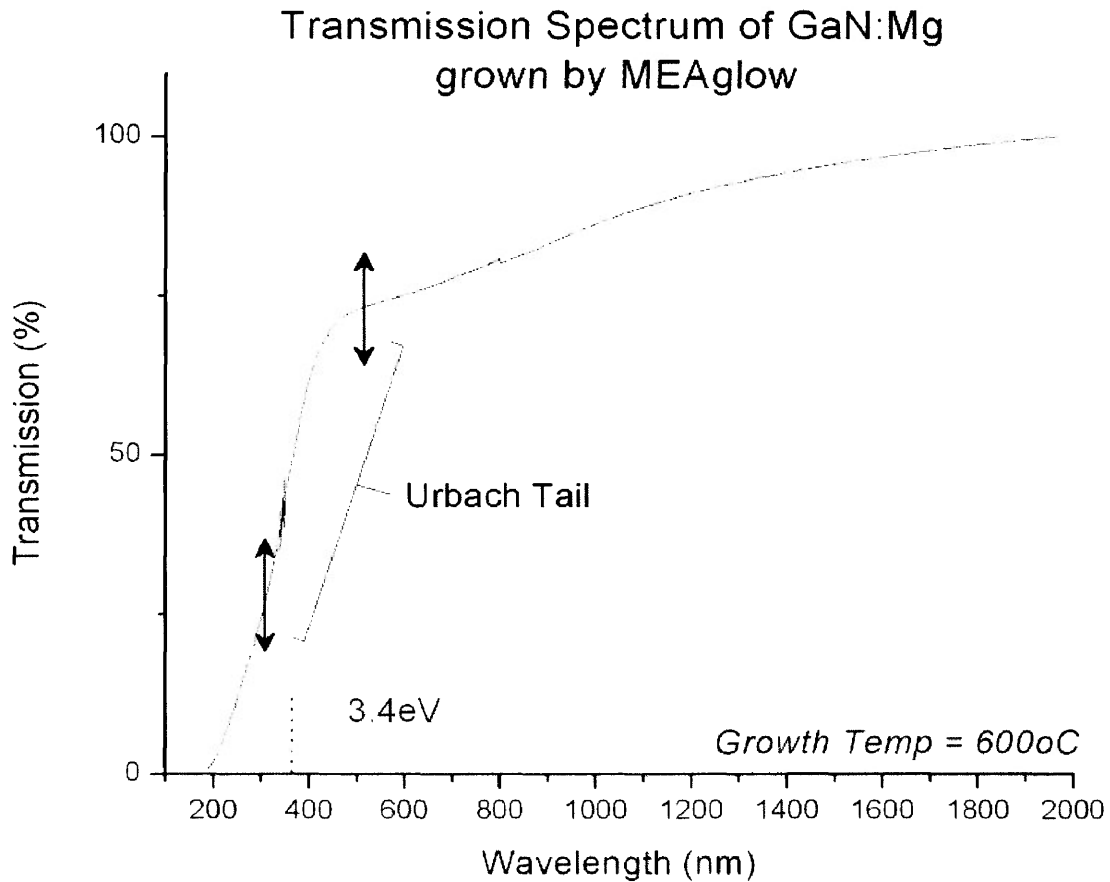


*Figure 4.17: The absorption spectrum of a sample of GaN showing the Urbach characteristic. The surface oxide causes absorption to occur at values not exactly equal to the 3.4eV bandgap.*

Because there is not an abrupt absorption edge, it is unclear what photon energy corresponds to the bandgap. A best practices method is used to yield the most accurate result. Through substituting into equation (4.6) the Beer-Lambert law ( $I = I_o \cdot \exp(-\alpha d)$ ), where  $I$  is the intensity at the detector and  $d$  is the sample thickness, one obtains the logarithmic relation,

$$\left[ \log \left( \frac{I}{I_0} \right) \right]^2 = \alpha_o^2 d^2 (h\nu - E_g) \quad (4.8)$$

which is known as the optical density squared (ODS). By plotting the  $ODS \leftrightarrow h\nu$  in a semi-log fashion, linear regions reflect energy levels where the Beer-Lambert law holds, whereas nonlinear ones reflect the effect of the Urbach tail. When considering linear plots of  $ODS \leftrightarrow h\nu$ , then, a tangent point placed in the Beer-Lambert dominant region area will yield an x-intercept indicative of the band transition, and will not be skewed by the Urbach tail (Figure 4.18).

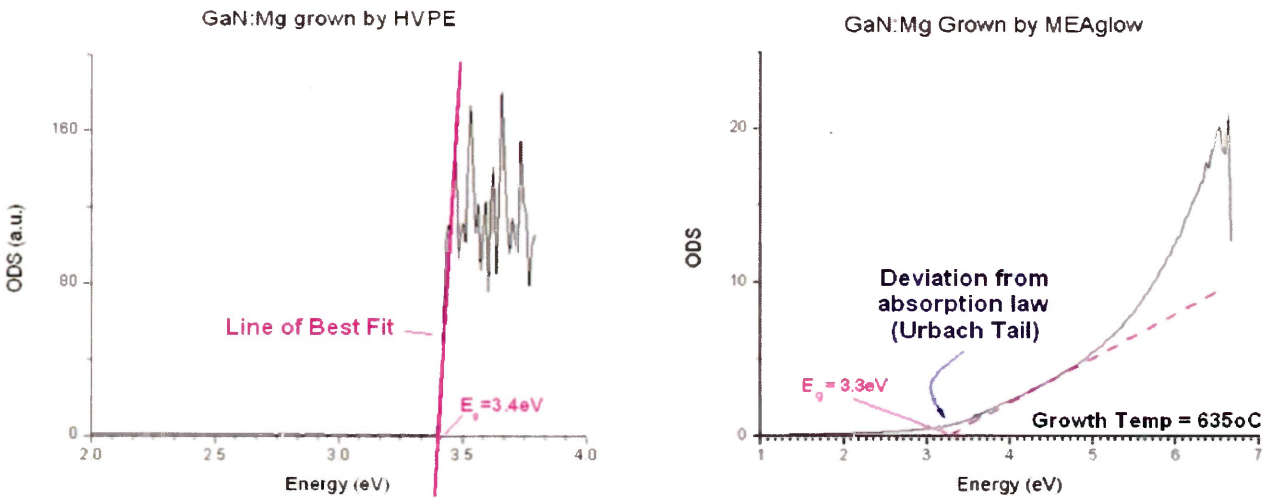


*Figure 4.18: Drawing a line of best fit. Some samples are easy to draw for. Others have the Urbach characteristics, making the line of best fit difficult. When plotted in a semilog fashion, the tangent point can be properly determined, yielding accurate bandgap energy like that from GaN:Mg grown by MEAglow (right).*

The analysis on the transmission spectra for the GaN samples grown by HVPE and MEAglow are shown below in Table 4.3. The most apparent result is that samples grown at low temperatures by MEAglow exhibited a lower bandgap than those grown at higher temperatures. In fact, the more gallium rich the sample was - indicated by the density of nanostructures on the surface

- the lower the bandgap (more accurately, the absorption gap) was. This is consistent with other experimental observation [68]. The next obvious result is the variability among samples grown by MEAgrow. The absorption gap energy spanned  $3.05eV$  to  $3.3eV$ , and while this was attributed to the gallium content, part of this is due to the technical variation of growth. The conditions inside the reaction chamber can be influenced by extraneous factors. For instance, sometimes the residual indium in the chamber after InN growth needed to be purged before GaN fabrication. Hence, some slight variability can be experienced. The other factor influencing the variability in this test is the drawing of the line of best fit. Even though the data was plotted using the ODS calculation, there may be some user related variability as to where the tangent point is placed, especially in samples with large Urbach tails. It is estimated that the bandgap energy can vary by as much as  $0.10eV$  due to this operator error<sup>5</sup>. These effects contribute to the overall error, however the highest bandgap appears to be for the  $600^{\circ}C$  sample - which appears to correlate with the brightest electroluminescence measurement.

---

<sup>5</sup>To be clear, the graph can be zoomed to accurately determine the x-intercept, however the placement of the tangent line is subject to user judgment.

Table 4.3: Absorption gap energy measured by transmission spectrophotometry, calculated using the optical density squared approach. Samples grown by low temperature MEAglow exhibited a smaller absorption gap energy.

HVPE Sample	Absorption Gap Energy (eV)
GaN:Mg	$3.38 \pm 0.03$
GaN (undoped)	$3.41 \pm 0.03$
GaN:Si	$3.40 \pm 0.03$

MEAglow Sample	Absorption Gap Energy (eV)
545 ( <i>Sample 1</i> )	$3.2 \pm 0.10$
545 ( <i>Sample 2</i> )	$3.05 \pm 0.10$
580	$3.2 \pm 0.10$
600	$3.3 \pm 0.10$
635 ( <i>Sample 1</i> )	$3.18 \pm 0.10$
635 ( <i>Sample 2</i> )	$3.22 \pm 0.10$

It is worth noting that the film thickness could not be determined from the transmission spectra of samples grown by MEAglow. The thickness is much smaller than that of the GaN templates grown by HVPE, and their uniformity is not as good. As a result, the interference fringes were not always visible.

## 4.6 Gallium Nitride Crystallinity observed by X-Ray Diffraction (XRD)

X-Ray diffraction (XRD) is the measurement of lattice spacing within the ordered semiconductor. X-rays are directed at the sample, and much like the Fabry Pérot system, if the ray is angled precisely such that the diffraction from monolayers beneath the surface constructively interfere with each other, a large diffraction signal is measured at the detector. Hence, by knowing the angle of diffraction of the peak signal from the surface, and also the X-Ray wavelength, the

lattice spacing can be calculated. Furthermore, if a sample is to be scanned to check its crystallinity, the resulting peaks can be compared to a reference table to determine what structures are contained within.

Sometimes, multiple signal peaks can be detected and are reflective of the presence of multiple crystal structures. For instance, some GaN samples grown in the Wurtzite (0001) configuration show evidence of cubic (110) structure, with more likelihood in areas with defects [44]. The samples examined here were simpler, however, and only showed diffraction from the Wurtzite (0002) GaN peak and from the sapphire substrate, as shown in Figure 4.19. Therefore, with a copper based X-Ray source, one expects there to be peaks at  $34.605^\circ$  and  $37.671^\circ$  for the (0002) GaN and sapphire crystals respectively.

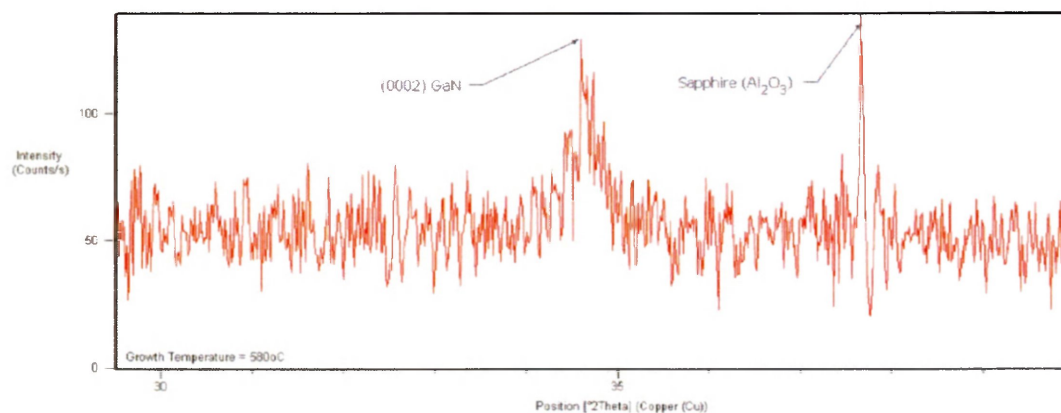


*Figure 4.19: A sample X-Ray diffraction of magnesium doped GaN grown by MEAglow. (0002) GaN and sapphire are the only two detectable structures.*

For each diffraction peak, the detector actually measures multiple peaks in very close proximity to each other. To produce the X-Rays, an electron beam is accelerated toward copper material, and the X-Rays produced stem from the atomic orbital interactions. There are, in fact, two orbitals that emit energies close together, K-alpha 1 and K-alpha 2, and another more distant one, K-beta. Before analyzing the measured data, K-alpha 2 is removed via post acquisition processing. K-Beta is filtered but may still be observed when strong diffraction lines are present.

Samples were placed in the instrument on a flat stage and a quick, 5 minute scan swept a large span of angles, namely  $2\theta = 29.5^\circ$  to  $2\theta = 40^\circ$ . All samples showed post-processed peaks at the (0002) GaN and sapphire positions. Next, the samples were scanned between  $2\theta = 33^\circ$  to  $36^\circ$ . To improve the signal to noise ratio (SNR), the angular sweep rate was slowed such that the entire scan took 79 minutes to complete.

An example of this longer X-Ray diffraction measurement is shown in Figure 4.20. The data is plotted in signal intensity (counts per second) to allow an appropriate comparison between films, and to allow comparison with other measurements made which may not have had the same measurement parameters. The GaN peak looks broad compared to the sapphire and the SNR still looks low, even with the long 79 minute scan. The peaks show some asymmetry, with the left tail extending longer than the right. This is attributed to the presence of nanowires. Due to their dearth of defects, nanowire diffraction exhibits sharp peaks. This response, superimposed on the film's broad peak, may cause this asymmetry; it was noted that samples exhibiting a higher density of nanowires on the film surface observed under SEM correlated to XRD peaks with larger asymmetry.

A measure of the crystal quality of the GaN is made by calculating the sharpness of this peak in terms of the Full Width at Half Maximum (FWHM), and the data is shown for all samples grown by MEAgrow in Table 4.4. The FWHM magnitudes spanned from  $0.27^\circ$  to  $0.47^\circ$ . The sample which showed the best luminosity during electroluminescence had a relatively sharp peak. Its FWHM was  $0.27^\circ$ , which is lower than the average width of  $0.35^\circ$  ( $p = 0.01$ )<sup>6</sup>. However the next brightest sample (temperature =  $635^\circ\text{C}$ ) did not have a relatively sharp peak ( $FWHM = 0.34^\circ$ ). This could be because, while the sample had large nanowires, its density was low, and thus its overall crystallinity is worse compares to the brightest sample. Scans of GaN samples grown by HVPE are also shown in Table 4.4, however the acquisition time was much shorter to prevent overloading the detector. The peak width ( $0.03^\circ$ ,  $FWHM$ ) was an order

---

<sup>6</sup> $p$  is the probability of a false conclusion. Unpaired t-test,  $\sigma_1 = 0.03^\circ$  representing technical variation in measurement, and  $\sigma_{avg} = (\Sigma\sigma_i)^{1/2}$

of magnitude lower than those grown by MEAglow, but this was due in part to their greater thickness ( $2 \rightarrow 4\mu m$ ) which greatly reduces the dislocation density and strain effects related to lattice mismatch with the sapphire substrate.

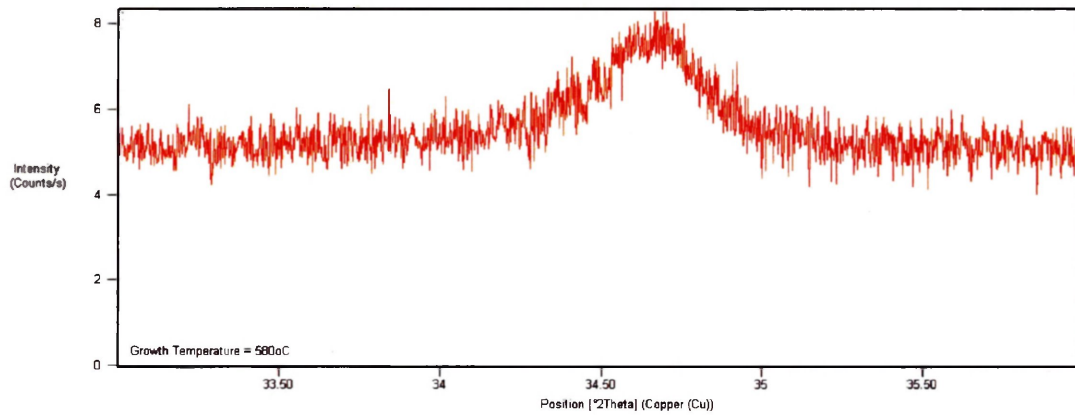


*Figure 4.20: XRD scan of GaN grown by low temperature MEAglow centred around the (0002) peak.*

Table 4.4: X-Ray Diffraction peak widths centred around the (0001) GaN position measured by Full Width Half Maximum (FWHM)

MEAglow sample			
Growth Temperature ( $^{\circ}\text{C}$ )	Peak Centre ( $^{\circ}$ )	FWHM ( $^{\circ}$ )	FWHM ( <i>arc sec</i> )
545 ( <i>Sample 1</i> )	34.71	$0.36 \pm 0.03$	1296
545 ( <i>Sample 2</i> )	34.67	$0.29 \pm 0.03$	1044
580	34.66	$0.38 \pm 0.03$	1368
600	34.64	$0.27 \pm 0.03$	972
635 ( <i>Sample 1</i> )	34.69	$0.34 \pm 0.03$	1224
635 ( <i>Sample 2</i> )	34.68	$0.47 \pm 0.03$	1692
Total Average	34.68	$0.35 \pm 0.07$	1264

HVPE sample			
Sample Doping Type	Peak Centre ( $^{\circ}$ )	FWHM ( $^{\circ}$ )	FWHM ( <i>arc sec</i> )
GaN:Si (n-type)	34.80	$0.028 \pm 0.01$	108
Undoped GaN	34.79	$0.028 \pm 0.01$	108
GaN:Mg (p-type)	34.79	$0.044 \pm 0.01$	158

The effect of the magnesium doping was observed by comparing these results to that from a sample without magnesium. A film of gallium nitride was grown on a sapphire  $\frac{1}{4}$  wafer using the same recipe, with the temperature set to  $580^{\circ}\text{C}$ , however the  $\text{CP}_2\text{Mg}$  flow was set to zero. The sample's bandgap was checked in the spectrophotometer and was found to be  $3.2\text{eV}$ , which is within expected ranges. What was not expected, however, was that the XRD measurement showed a strong diffraction intensity. The peak centred around the (0002) GaN position showed a much better SNR than that from the magnesium doped ones, with the same scanning conditions; the diffraction intensity was 13.7 times higher than the magnesium doped samples, under the same angular resolution ( $0.0067^{\circ}$ ). The peak FWHM was better than that of the magnesium doped samples ( $0.23^{\circ}$  for the undoped sample versus the larger values shown in table 4.4).

The implications of this are clear. The presence of magnesium during growth greatly affected the crystallinity of the sample as observed through X-Ray diffraction. Since doping with magnesium is known to yield material with a poorer film quality, as is seen in the AFM image of semiconductors grown using HVPE (Figure 4.11), it is no surprise that the XRD peak sharpness is compromised. However, the impairment was much greater than that found in samples grown by HVPE. Hence, the use of magnesium in the MEAgrow system is not optimal, and determination of the proper growth conditions should reduce the impairment.

## 4.7 P-GaN Growth Optimization

With the interpretation made from the XRD results, there now are two stoichiometric ratios important in optimizing the film growth: that between gallium and nitrogen, and the one between magnesium and the other elements. The first is implicated in droplet formation, which is known to trap magnesium in pure metal and not the lattice as discussed in section 2.3.2. The second is claimed because experimental X-Ray diffraction evidence suggests magnesium is affecting the quality of the film. Magnesium is known to make self compensating centres when too much is present, and furthermore it can make stacking faults, pyramidal defects, and local inversion domains<sup>7</sup> [19, 21]. It is also possible that direct observation of these defects was not possible with SEM. For instance, unless the magnesium concentration is extremely large ( $> 4.5 \times 10^{20} \text{cm}^{-3}$ ), the pyramidal defects are not detectable by this technique [19], and in this case the defects are best detected by TEM [21] - a highly specialized instrument.

To this end, the first optimization made was to lower the magnesium flow. Still kept at the same partial pressure of  $0.158 \text{ Torr}$ , the flow rate was dropped from  $100 \text{ sccm}$  to  $10 \text{ sccm}$ . Therefore, the proportion of magnesium to gallium changed from  $10.4\%$  to  $1.0\%$  ( $322 \mu\text{mol}/\text{min}$  to  $32 \mu\text{mol}/\text{min}$ ). The growth temperature used was that which produced the greatest electroluminescence,  $600^\circ\text{C}$ . A second growth under the same conditions but with no magnesium flow was performed to be used as a control.

---

<sup>7</sup>Where the polarity of the semiconductor changes to the opposite direction

The reason for the control was imperative. In the time between the growth of all prior magnesium doped samples and the one at hand, the reaction chamber and the plasma system underwent development. With the change in the system, growth conditions could change significantly.

When taken out of the reaction chamber, both samples, the one doped with magnesium and the one with no magnesium, had a powdery appearance. This was found in many indium nitride samples grown intentionally to have a large density of nanowires. Further measurements were carried out to confirm this.

The resistivity measured in the hall configuration was  $(96.3 \pm 0.5) \Omega \cdot cm$  and  $(17.3 \pm 0.1) \Omega \cdot cm$  for the undoped and doped samples respectively. This is slightly-to-considerably higher than the resistivities for other magnesium doped GaN samples grown by MEAglow ( $0.84\Omega \cdot cm$ ,  $8.77\Omega \cdot cm$  and  $16.77\Omega \cdot cm$  for three different samples). What this could be indicative of is a reduction in the background oxygen concentration (i.e. electron concentration). Resistivity inversely scales with the total carrier concentration (and hence doping). Since there is not much magnesium being introduced during growth, the low conductivity is associated with an equally low electron concentration.

The samples were placed in the transmission spectrophotometer to measure the bandgap. Interestingly, there was a large attenuation starting below the bandgap energy (Figure 4.21). This could be due to the visible cloudiness of the sample which could cause scattering of the light. When graphed with respect to optical density squared (ODS), the measured bandgaps were 1.8eV and 1.1eV for the doped and undoped samples respectively. To explain this, the cloudy surface could be skewing the line of best fit, or the GaN lattice could be compromised so much that its bandgap is not 3.4eV.

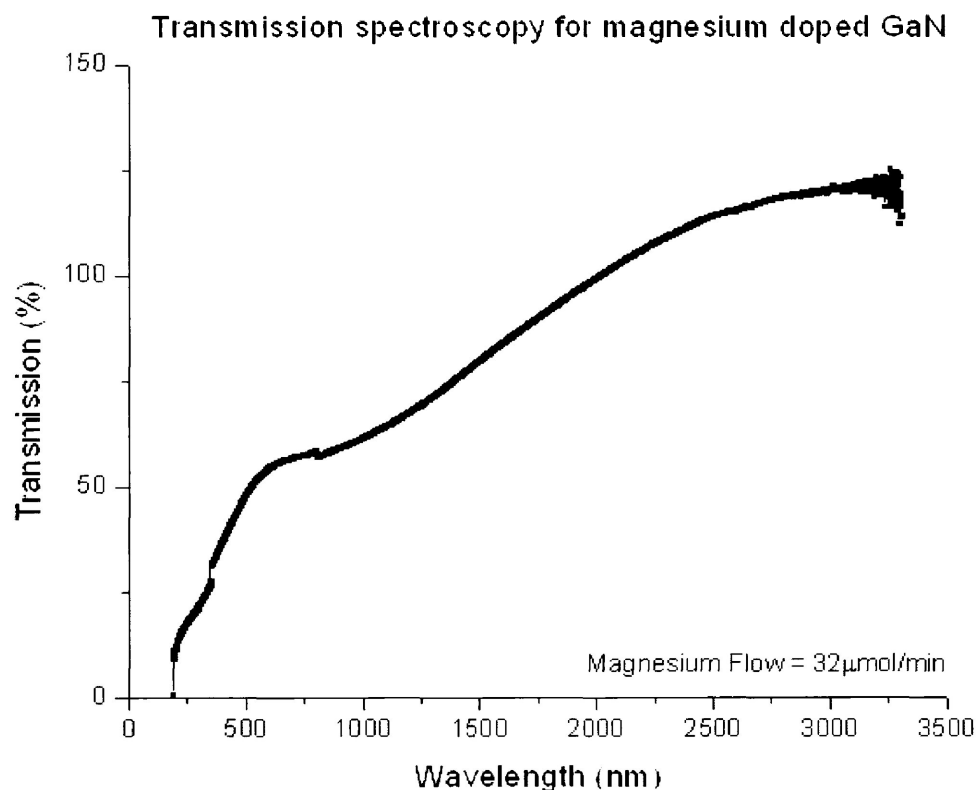


*Figure 4.21: The transmission spectrum of a magnesium doped GaN sample grown by low temperature MEAglow with a smaller CP<sub>2</sub>Mg flow. The change in the system caused sample defects which increased the attenuation, causing the bandgap to be measured incorrectly.*

The samples were then scanned using the AFM. The surfaces showed so much metal that the images became corrupt (Figure 4.22). This result confirms the lack of integrity found in the spectrophotometer measurements.

Lastly, the XRD properties of the samples were acquired. Only the same two peaks from (0002) GaN and sapphire were present. When scanned around the (0002) GaN position, the magnesium doped GaN showed a sharp peak on top of a broad one (Figure 4.23). This is consistent with the observation of nanowires on the surface described earlier, and the small FWHM of 0.11° and 0.14° (for Mg-doped and undoped samples respectively) is indicative of their defect free nature. While the intensity (in counts per second) of the magnesium doped

GaN was similar to the previous growth series, that of the undoped GaN was weaker (Figure 4.23b). Instead of having an intensity an order of magnitude higher as per the previous undoped sample, it was only about twice as high. This is strong evidence that the control did not perform as expected. The only differences between this and the previous growth were  $20^{\circ}\text{C}$  in temperature - which are unlikely to significantly change the growth physics - and the changes to the plasma configuration - which in all likelihood affected the sample morphology. Hence, further growth optimization is required with the new plasma source configuration.

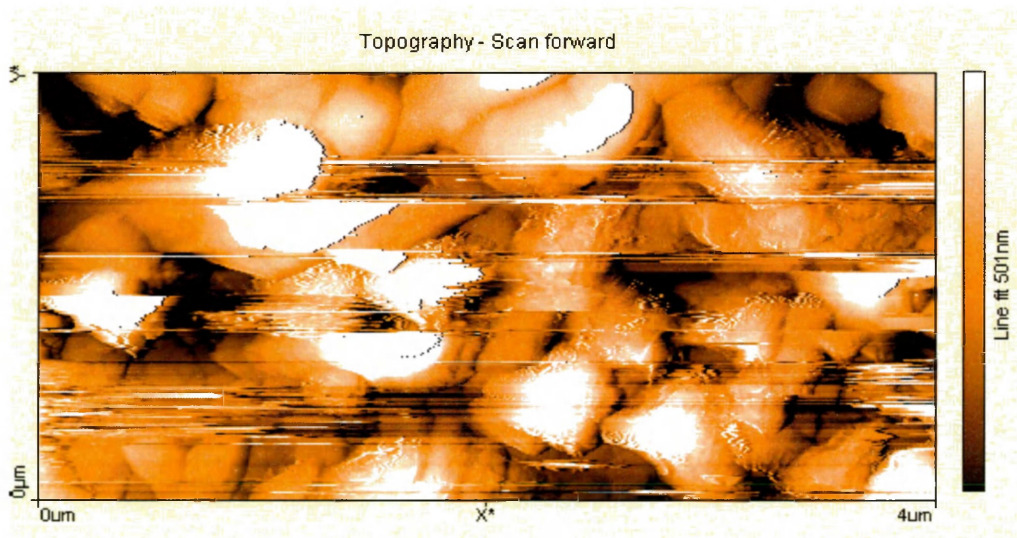


*Figure 4.22: Atomic force microscopy image of undoped GaN grown with new changes to the system. The large density of nanostructures caused the instrument to yield many measurement problems.*

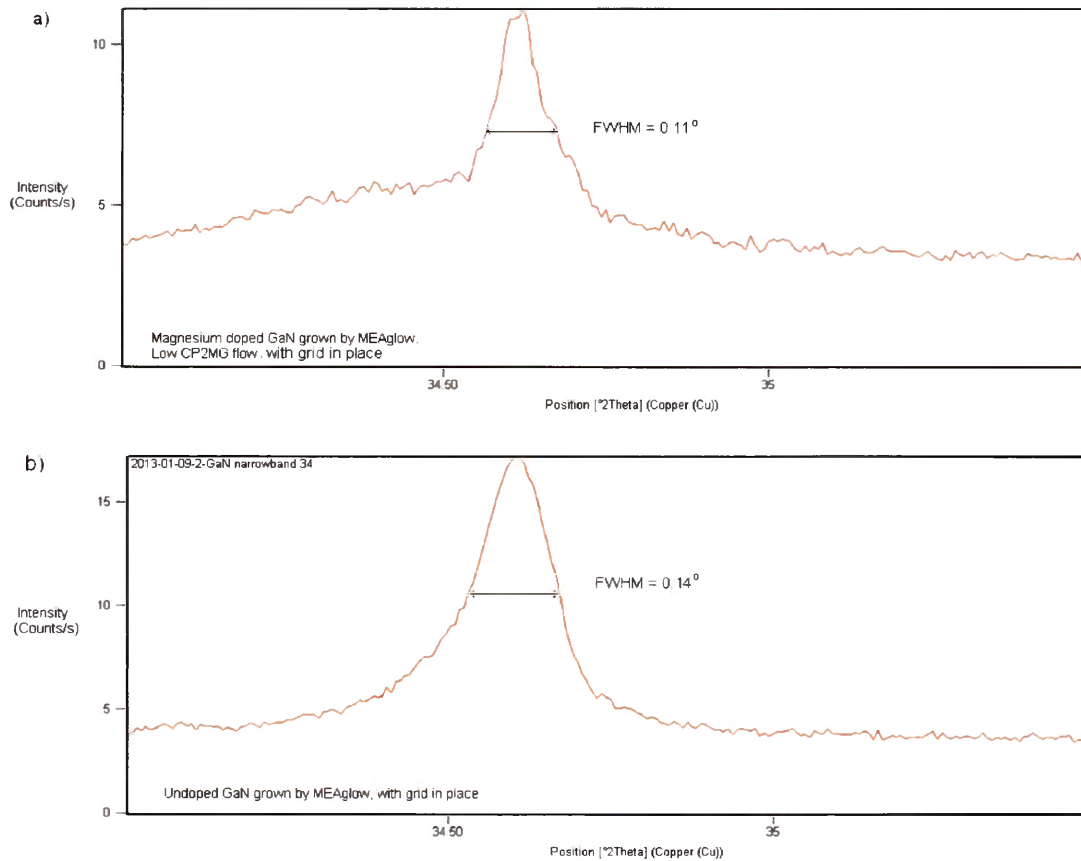


Figure 4.23: X-Ray diffraction measurements of a) magnesium doped GaN grown at  $600^{\circ}\text{C}$  with lower CP2Mg flow and the reconfigured plasma source, and b) undoped GaN grown at  $600^{\circ}\text{C}$  with no CP2Mg flow and the reconfigured plasma source. Both show the presence of a sharp peak due to GaN nanowires. The diffraction intensity for the magnesium doped sample was close to that found from samples grown without the RF shield, however the undoped sample had a lower intensity.

## 4.8 Chapter Summary

P-type GaN films were fabricated using MEAglow growth technology at low temperatures. It was found that as the temperature decreased, the film thickness increased, indicating that low temperatures are conducive to higher growth rates. Films were gallium rich, with nanowires and nanostructures growing spontaneously. This feature was confirmed with microscopy (SEM and

AFM), bandgap measurements, and by the presence of superimposed sharp peaks detected during X-Ray diffraction. The density of nanowires as seen in electron microscopy were observed to inversely correlate with LED brightness, while there was some evidence that a film with greater surface roughness outside of these nanostructures emitted more light. It should be recognized that these were only preliminary investigations into the effect of magnesium introduction. Unfortunately, the growth system underwent a modification, and the comparison of lightly Mg-doped materials could not be made.

## Chapter 5

# Inverted High Indium Content InGaN LEDs with Codoped P-type Layer

The design hurdle in creating the Mesa LED structure described in Chapter 2 has been well established as it is the theme of this research; p-type GaN must be grown at a low temperature to prevent the indium decomposition from the InGaN active layer. This issue is especially acute for high indium content InGaN. Two problems persist. The first is the difficulty of growing at low temperatures, having the stoichiometric issues associated with it, and the second is the challenge in obtaining high p-type conductivity. A more ideal situation would be to grow the p-type layer at high temperatures first, and then grow the InGaN active layer. Since the heterojunction is present, a 2-dimensional hole gas may be formed, much in the same way it is done with electrons in high electron mobility transistors (HEMT) [73]. As a result, a layer grown above the InGaN to act as one side of a quantum well may not be necessary since charge confinement is already occurring.

This approach is not common place because of the high series resistance inherent in the p-type layer. As shown in Figure 5.1, for an inverted Mesa structure, current needs to travel along the p-type layer before it reaches the conductive n-type layer. Whereas, in standard Mesa structured LEDs, current flows mainly through the highly conductive n-type base layer, and

then only through a few nanometers of more resistive p-type GaN underneath the metal contact. Therefore, the inverted structure would create more heat, which would limit device performance. What is peculiar about the work done in this thesis is the low resistivity found in some magnesium doped GaN films. Resistivities were found to be as low as  $0.04\Omega \cdot cm$  in commercial samples, which is lower than published values of resistivity ( $0.18 \rightarrow 2.84\Omega \cdot cm$ , [62]<sup>1</sup>). Therefore, these samples have conductivities closer to that of n-type GaN ( $0.003 \rightarrow 0.03\Omega \cdot cm$  [62]<sup>2</sup>) and could potentially be used as a base layer for the LED structure.

It is likely that codoping could be the cause of the high conductivity. The resistivity becomes a weighted fraction of both the electrons and holes, and thus the carrier transport takes advantage of the high electron mobility. Therefore, the relation

$$\rho = \frac{1}{q(\mu_n n + \mu_p p)} \quad (5.1)$$

states that a small amount of electrons can decrease the resistivity sufficiently while maintaining p-type conductivity. This was the case for the commercial GaN samples. All films displayed electroluminescence, indicating its p-type conductivity, however two of the three samples showed codoping in Hall measurements because of the n-type conductivity reading. Since it was shown in equation (3.18) that a net p-type conductivity is still possible even though Hall measurements are n-type, this is strong evidence that codoping is present. Furthermore, changes in net carrier concentration for similar samples, as observed by Hall measurements, can be attributed to the background electron concentration. Two samples from the same manufacturer grown by MOCVD had drastically different Hall concentrations ( $-1.58 \times 10^{18}cm^{-3}$  versus  $+1.12 \times 10^{17}cm^{-3}$ ) and resistivities ( $0.038\Omega \cdot cm$  versus  $4.66\Omega \cdot cm$  respectively), but had approximately the same electroluminescence intensity when current passed across its n-type oxide surface. Since both samples' optical performances were the same, it is concluded that the same p-type conductivity is present, but the background dopant density - likely due to oxygen - is different. There is some evidence

---

<sup>1</sup>using  $\rho = 1/(\mu \cdot p \cdot q)$

<sup>2</sup>Depending on carrier concentration,  $\rho = 1/(\mu \cdot n \cdot q)$

that p-GaN films grown by MEAglow samples exhibit low resistivity due to codoping as well. One sample grown in a MEAglow environment<sup>3</sup> measured a resistivity of  $0.414\Omega \cdot cm$ . Although this sample was not prepared to be observed under electroluminescence to gauge carrier type, this value is on the lower side of the published range indicated above, thus electron drift could be increasing the conductivity.

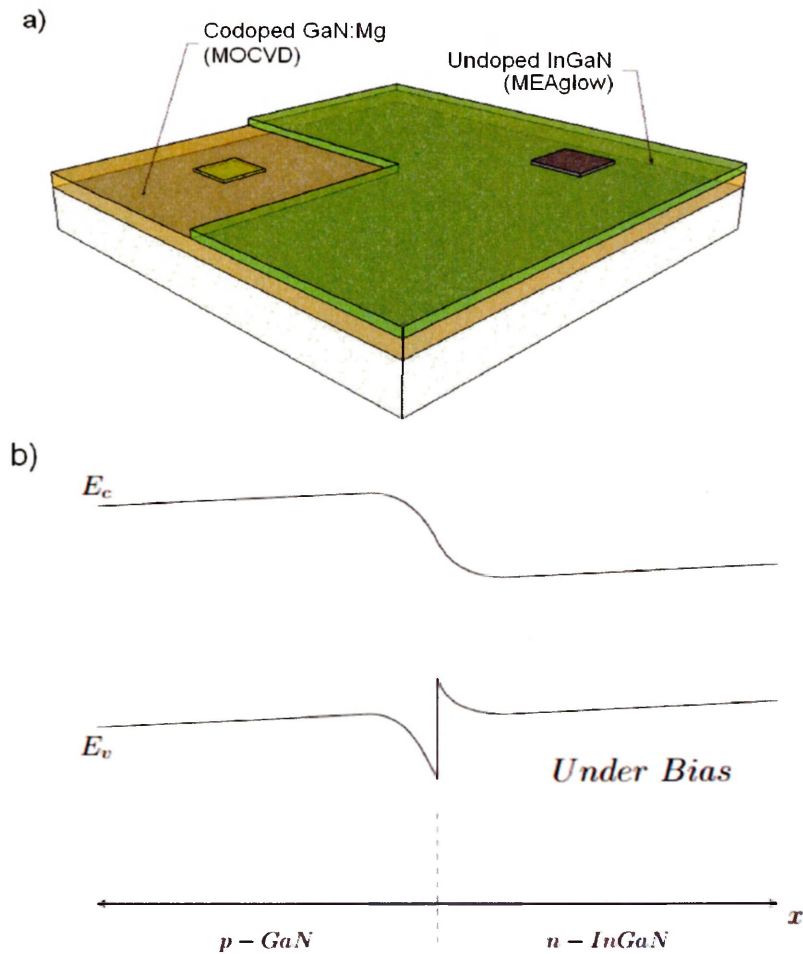


Figure 5.1: a) The structure of an inverted LED with the p-type layer at the bottom, and b) its resulting Anderson band model. When using codoped GaN:Mg, the series resistance along this base layer is lower, facilitating the inverted structure.

<sup>3</sup>Not grown by the parameters specified in Section 4.2

This chapter demonstrates the feasibility of fabricating LEDs with a p-type bottom layer, even if it is codoped to the point where it electrically measures n-type conductivity by Hall effect. A test device was fabricated with a tuned colour of emission, i.e. the InGaN active layer. Its I-V characterization is acquired to determine if a p-n structure is present, and an electroluminescent spectrum is obtained to gauge the colour and intensity of the emission.

## 5.1 Active Layer Growth

A commercially acquired magnesium doped GaN sample grown by HVPE was used as the base template. The film in question was codoped with background oxygen, showing a Hall concentration of  $-1.7 \times 10^{18}$  electrons per  $cm^3$  and a resistivity of  $0.122\Omega \cdot cm$ . The template was chemically etched in an HCl : H<sub>2</sub>O solution (1:3) for 5 minutes and placed in the reaction chamber for growth of InGaN on top. The growth conditions for InGaN are slightly different than that of pure GaN, hence the recipe had the following characteristics:

- The chamber was brought to  $540^{\circ}C$  under a flow of inert nitrogen gas - used to help clean the surface for contaminants.
- The same nucleation step was used as for the previous growths described in section 4.1.1 (1 minute of nitrogen plasma at 1000sccm, 100 Watts of RF power at an ambient pressure of 750mTorr)
- Metal modulation had a cycling period of either 3.5 or 5 seconds of metal organic (MO) delivery (Ga and In) to 20 seconds of nitrogen plasma delivery. In this growth, however, plasma activation was stopped during the MO period to prevent early nitridation of the elements. Both trimethylindium and trimethylgallium flowed at 0.5sccm, while nitrogen flowed at 500sccm consistently, regardless of plasma activation and had a pressure of 1310mTorr.
- After 25 modulation cycles, there was a 60 second period where no metalorganics flowed and the plasma remained inactive. This was in order to clean the chamber of accumulated excess

metalorganic and maintain the efficacy of metal modulation by reducing the chamber's memory effect [16]. As a result, the growth rate did not suffer as time progressed.

- After 54 repetitions of metal modulation then chamber cleaning, the growth was finished, taking 10 hours to complete.
- The sample was on a platform rotating at 50RPM during the growth.

## 5.2 Verification of Device Structure

A rectifying behaviour was sought from the device. If there was no built-in potential, then the device will not turn on. Therefore, the I-V characteristics were investigated on this device. Gold metal was sputtered on the p-type side, and indium-tin metal was placed on the n-type side to reduce the contact resistance and provide ohmic contacts. The I-V curve is shown below in Figure 5.2. Here, rectification is clearly present. In fact, rectification was present in both directions, likely due to the presence of the n-type oxide on the surface of the exposed p-GaN base layer, as shown in Figure 5.3. Since there is a Fermi level mismatch between this oxide and the n-InGaN, some amount of rectification occurs in the reverse bias direction. The series resistance, measured as the inverse of the slope in the flatband condition (large applied voltage) was determined to be  $398\Omega$ . It is also possible the surface oxide is contributing to this low value along with the p-GaN base. The built-in potential, when extrapolating the flatband curve, or when removing the effect of the series resistance as in section 3.3, was determined to be 17 Volts, which is not reasonable. The following explanation is given. At high forward currents and voltages - in this case producing a maximum of 2 Watts - the applied power heats the device, altering its characteristics. Since the resistivity is lowered, more current passes, heating the device further. Since these conditions can skew the measurement, the extrapolation is flawed and cannot be used to determine the built-in potential magnitude.

## InGaN grown by MEAglow on GaN:Mg grown by HVPE

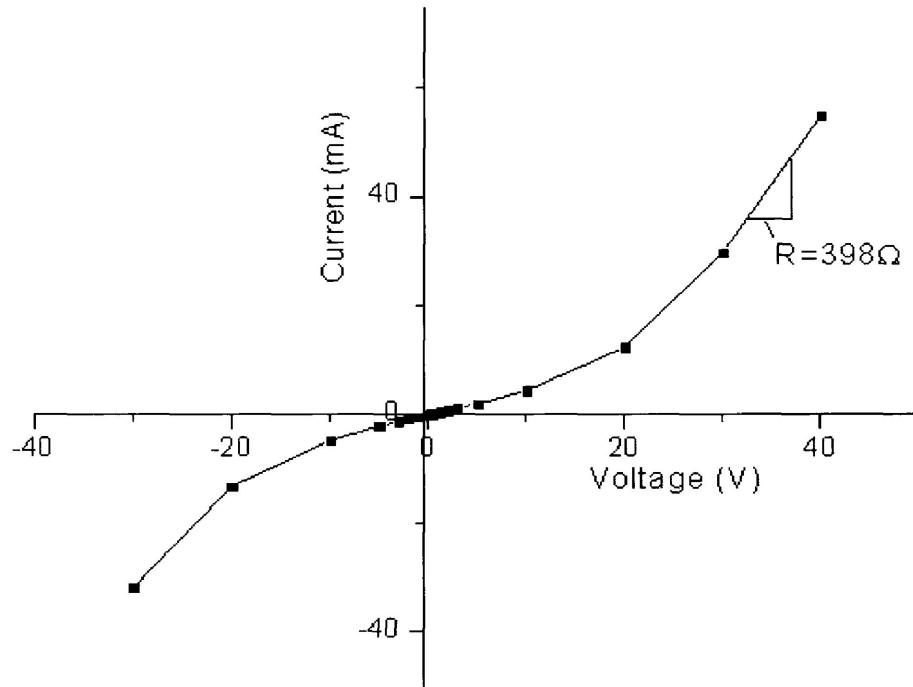


*Figure 5.2: The I-V characteristics of the InGaN - p-GaN LED. The series resistance measured in the flatband configuration was  $398\Omega$ , although this value could be underrepresented because of the surface n-oxide resting on the p-GaN.*

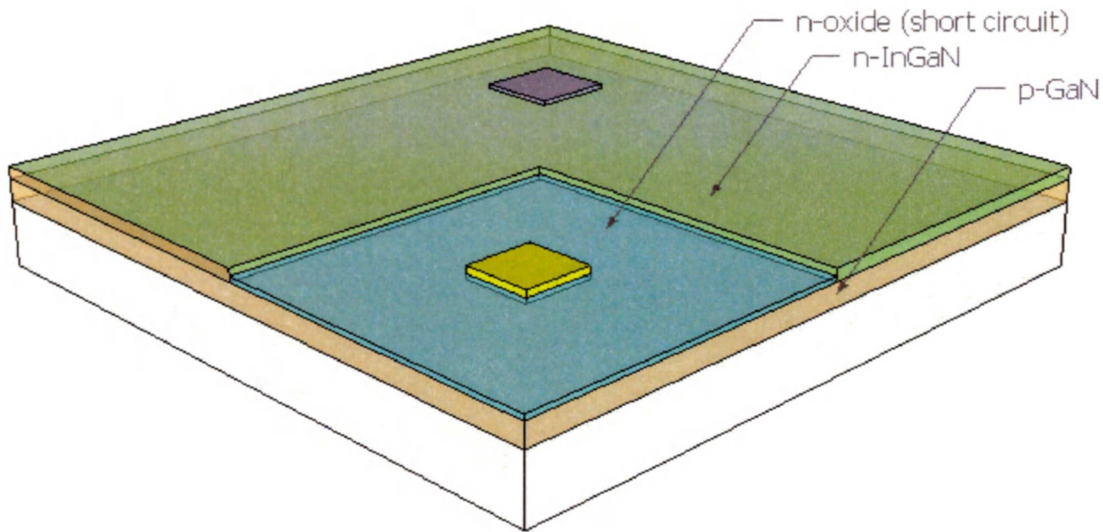


*Figure 5.3: The presence of an n-type oxide (blue) on the surface of the p-GaN acts as a conductive path (short circuit) to the gold contact.*

### 5.3 Device Performance

The LED shone a bright yellow colour (Figure 5.4). This was confirmed by electroluminescent spectroscopy. A photospectrometer was coupled to the LED in the same way as described in section 3.1. The detector acquisition time was set to 1000ms, and 10 acquisitions were averaged to reduce the noise. The applied current was varied, and resulting EL spectra are shown below in Figure 5.5. As can be seen, there is a peak luminescence at 560nm (2.2eV, green light), which is in the middle of the ‘green gap.’ The peak spanned from about 500 (blue-green) to 600nm (orange), measured at FWHM. This emission was not from the yellow defect inherent in some gallium nitride samples. That phenomenon, which was observed earlier, spans from 500 to 800nm, whereas this emission was sharper. Hence, the spectrum seen is mainly from the InGaN band to band transition.

The implications of this result are far reaching. As shown in Figure 1.1, luminosity from InGaN starts to decrease at green wavelengths, and is further reduced at longer wavelengths

(yellow, red). Since yellow-green light was present, this indicates that if the  $\text{In}_x\text{Ga}_{1-x}\text{N}$  mole fraction were tuned to true green or blue-green light, even brighter emission could result, addressing the green gap issue. This tuning, however, was difficult to achieve and would require significant optimization beyond the scope of this thesis. The relationship between bandgap and mole fraction is not linear, and is due to a bowing parameter [44]. Such a bowing is illustrated in Figure 5.6, where the bandgap of  $\text{In}_{1-x}\text{Ga}_x\text{N}$  as measured by low temperature photoluminescent spectroscopy<sup>4</sup> follows a curved contour with respect to the gallium mole fraction,  $x$ . That is why one of several attempts (5 films) yielded green light; others were yellow, orange or blue. Even with the yellow emission, the LED provided relatively bright light for a single heterostructure LED. With room lighting turned on, the LED was still visible. Hence, if the LED was fabricated with pristine quality and packaged properly, the device could potentially meet brightness criteria for some commercial lighting applications.

---

<sup>4</sup>Similar to electroluminescent spectroscopy, except incident photons excite the material instead of applied current

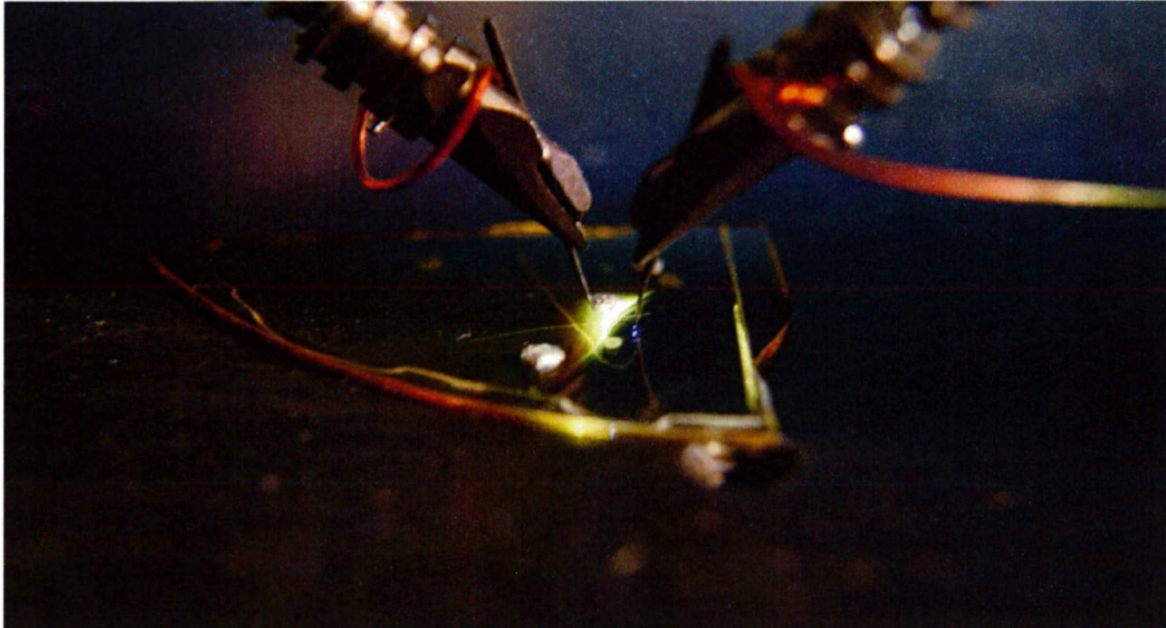


Figure 5.4: A picture of the InGaN on codoped p-GaN LED during operation. One side of the film (the right side) had a cover placed on top during growth so that it is exposed to the surface. Two electrodes can thus contact each side of the p-n junction, allowing light to emanate. Picture was taken with a high exposure time (30s).

### Electroluminescence of InGaN grown on codoped p-type GaN

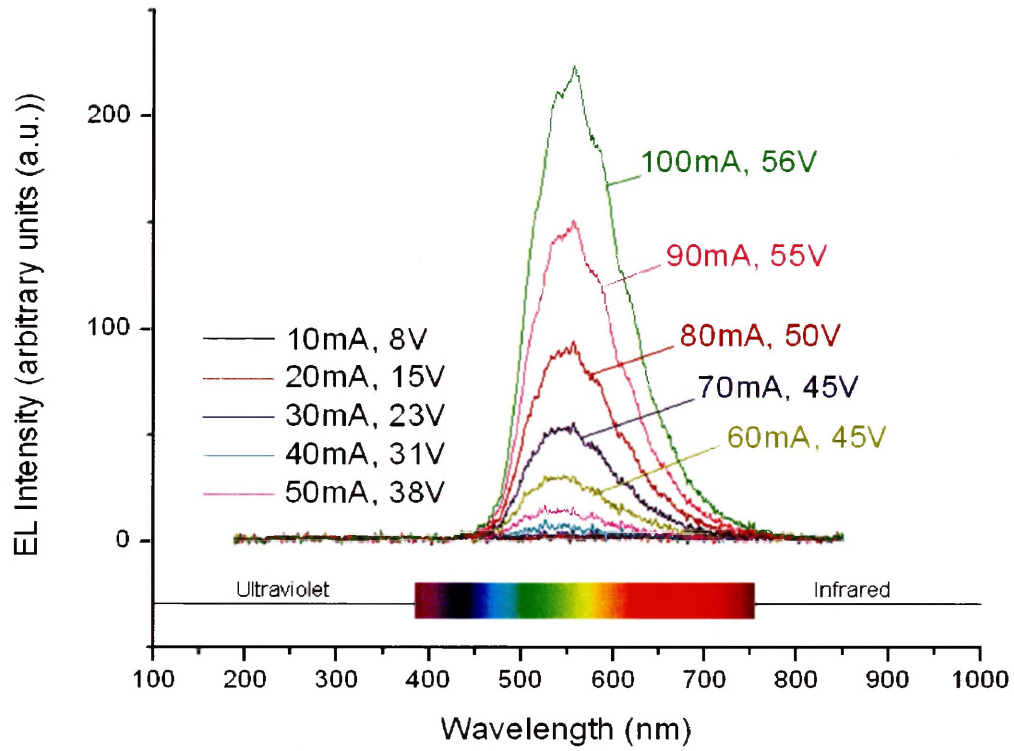


Figure 5.5: The measured electroluminescence of InGaN grown on a codoped p-type GaN template.

Here, the peak lies in the green - yellow region.

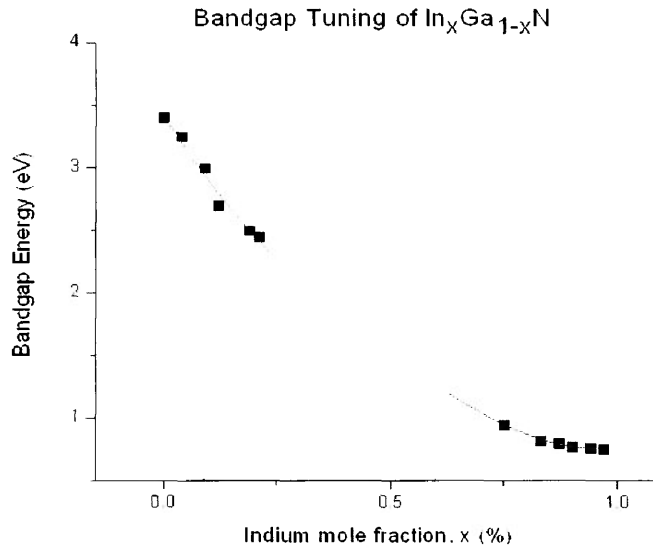


Figure 5.6: The bowing of bandgap energy of an InGa<sub>x</sub>N alloy (graph modified from [74]). Here, there is a nonlinear interpolation of the bandgap energy between low gallium content (indium rich) and high gallium content (gallium rich) films.

## 5.4 Chapter Summary

Codoped p-GaN materials have been shown to be a candidate for base layers in inverted LED structures. InGa<sub>x</sub>N was grown on top of a codoped p-GaN template layer and was observed to emit green-yellow light. The template layer was still slightly resistive, and heating became a problem at high forward currents. Current may have travelled along the n-type oxide resting on the surface of the p-GaN, making I-V characterization difficult, and potentially causing carrier drift in unexpected regions during operation. The green - yellow emission may be an indication that single heterojunction LEDs are a solution to the problems associated with low temperature p-GaN epilayer growth in high indium content, green LEDs

## Chapter 6

# Conclusions and Future Work

This thesis reports the first confirmed p-type gallium nitride film grown using low temperature MEAgrow. While the standard electrical measurement, the Hall effect, showed n-type conductivity for both commercially available films and those grown by MEAgrow, other methods proved the p-type surplus. Namely, electroluminescence spectroscopy showed the presence of carrier recombination, indicating the presence of p-type conductivity, while I-V characterization was able to measure this parameter in some samples. Therefore, characterization efforts should focus on these two approaches to optimize the carrier concentration of p-GaN films. The result has impact in the manufacturing of InGaN based LEDs. The low temperature necessary to prevent indium desorption is an additional constraint, reducing the quality of the material. Hence, the fabrication of p-type gallium nitride in a system favourable for low temperature nitride semiconductor growth such as the MEAgrow one is a good step in the device development.

The ability to fabricate semiconductors at low temperatures was assessed. Growth occurred at  $545^{\circ}\text{C}$ ,  $580^{\circ}\text{C}$ ,  $600^{\circ}\text{C}$  and  $635^{\circ}\text{C}$  in spite of the temperature at which indium decomposes from the lattice ( $\sim 600^{\circ}\text{C}$ ) to assess the system's capability of producing full quantum well LEDs. Samples were resistive, making electrical characterization difficult. Scanning electron microscopy, atomic force microscopy, transmission spectroscopy and X-Ray diffraction were used to determine the suitability of the growth conditions. It was found that, as the growth temperature increased,

the growth rate decreased, indicating that greater amounts of gallium and nitrogen desorb from the sample surface at higher temperatures. Growth rate, as indicated by the film thickness, also suffered by the formation of nanowires and nanostructures, which were readily formed under the gas flow rates, temperature ranges, pressures and growth progression used. These nanostructures were indicative of metal rich growth conditions, causing the bandgap transition to occur at longer wavelengths. Finally, there were correlations between the films with the lowest density of nanostructures, largest surface roughness, electroluminescence and net hole carrier concentration determined by I-V characterization. This suggests that growth conditions that suppress these formations are more optimal.

Magnesium was implicated in the deterioration of optimal growth conditions. A semiconductor film that did not have magnesium present during growth had a much higher X-Ray diffraction intensity and a moderately better crystalline structure determined by its XRD peak width. The exact physical mechanism behind this is not yet known. Attempts were made to discover the cause of film degradation due to magnesium incorporation and optimize the film quality, first by reducing CP<sub>2</sub>MG flow, then possibly by altering other conditions, however the plasma system changed since the growth of the above temperature series, causing comparisons between growth parameters to become inappropriate.

Some issues of low temperature growth of p-GaN films in LED applications, like that of stoichiometry could be eliminated if a structural solution was possible. It was found that inverting the LED structure such that the p-type GaN was grown below the InGaN layer would reduce the complications of growing p-GaN layers at low, indium preserving temperatures. If the p-type layer was at the bottom of the structure, it could be grown at a higher temperature without regard for any indium decomposition in the InGaN layer, while the *p-GaN / n-InGaN* heterostructure provides similar charge confinement as a quantum well LED. The essential property in achieving this structure is the reduced resistivity in codoped materials. P-type GaN with a high background electron concentration has been shown to have a resistivity two orders of magnitude lower than

its single-doped counterpart. As a result, an appreciable amount of current could pass through the p-type layer, producing noticeable light. The light produced was very impressive. Bright visible light under ambient room lighting was produced, and its yellow colour was indicative of stronger emission than it should have according to the green gap principle.

The ability to use the codoped p-GaN layer as the template is promising for future LED development. The codoped p-type layers studied in this work could conceivably be used as a template for additional InGaN growth. As a result, this could be a quick test for InGaN luminescence, and a prototype for a green LED grown entirely by MEAgrow.

# Bibliography

- [1] P. Hindle, "Future market opportunities for GaN" *Microwave Journal*, Mag., June 12, 2012.
- [2] W. Gotz, et al., "Activation of acceptors in Mg-doped GaN grown by metalorganic chemical vapor deposition," *Appl. Phys. Lett.*, vol. 68, pp. 667-669, 1996.
- [3] H. Morkoç, "Electronic band structure and polarization effects," in *Handbook of Nitride semiconductors*, vol. 1, Weinheim, Germany: Wiley-VCH, 2008, ch. 2, pp. 131-322.
- [4] R. F. Karlicek, "UV-LEDs and curing applications: technology and market developments," *Radtech Report*, Mag., pp. 17-23, Nov./Dec. 2009
- [5] S. J. Pearton, "GaN and related materials," New York: *Gordon and Breach*, 1997.
- [6] S. J. Pearton, et al., "Fabrication and performance of GaN electronic devices," *Mat. Sci. Eng.*, R30, pp. 55-212, 2000.
- [7] J. Wu, "When group-III nitrides go infrared: new properties and perspectives," *J. Appl. Phys.*, vol. 106, 011101, 2009.
- [8] M. Moseley, et al., "Control of surface adatom kinetics for the growth of high-indium content InGaN throughout the miscibility gap", *Appl. Phys. Lett.*, vol. 97, 191902, 2010.
- [9] D. J. Rogers, et al., "Improved LEDs and photovoltaics by hybridization and nanostructuring," *SPIE Newsroom*, Mag., 10.1117, June 15, 2012.

- [10] R. Oliver, et al., "Growth modes in heteroepitaxy of InGaN on GaN," *J. Appl. Phys.*, vol. 97, 013707, 2005.
- [11] A. G. Bhuiyan, A. Hashimoto, A. Yamamoto, "Indium nitride (InN): a review on growth, characterization, and properties," *J. Appl. Phys.*, vol. 94, pp. 2779 - 2804, 2003.
- [12] G. F. Yang, et al., "Temperature dependent growth of InGaN/GaN single quantum well," *Superlatt. Microstr.*, vol. 52, pp. 349-356, 2012.
- [13] A. White, W. Melville, "The decomposition of ammonia at high temperatures," *J. Am. Chem. Soc.*, vol. 27, no. 4, pp. 373-386, 1905.
- [14] S. C. Jain, et al., "III-nitrides: growth, characterization, and properties," *J. Appl. Phys.*, vol. 87, no. 3, pp. 965-1001, 2000.
- [15] S. W. Choi, K. J. Bachmann, G. Lucovsky, "Growth kinetics and characterizations of gallium nitride thin films by remote PECVD," *J. Mater. Res.*, vol. 8, no. 4, pp. 847-854, 1993.
- [16] S. D. Burnham, "Improved understanding and control of magnesium-doped gallium nitride by plasma assisted molecular beam epitaxy," Ph.D. dissertation, School of Elec. Comp. Eng., Georgia Institute of Technology, Atlanta, GA, 2007.
- [17] K. S. A. Butcher, et al., "Gallium Nitride Film Growth Using a Plasma Based Migration Enhanced Afterglow Chemical Vapor Deposition System," *Jap. J. Appl. Phys.*, vol. 51, 01AF02, 2012.
- [18] K. S. A. Butcher, et al., "InN grown by migration enhanced afterglow (MEAglow)," *Phys. Stat. Sol. A*, vol. 209, no. 1, pp. 41-44, 2012.
- [19] G. Martinez-Criado, et al., "Optical characterization of Mg-doped GaN films grown by metalorganic chemical vapor phase deposition," *J. Appl. Phys.*, vol. 88, pp. 3470-3478, 2000.

- [20] H. Obloh, et al., "Self-compensation in Mg doped p-type GaN grown by MOCVD," *J. Cryst. Growth*, vol. 195, pp. 270-273, 1998.
- [21] P. Vennéguès, et al., "Atomic structure of pyramidal defects in Mg-doped GaN," *Phys. Rev. B*, vol. 68, 235214, 2003.
- [22] C. Vinegoni, et al., "Morphological and optical characterization of GaN prepared by pulsed laser deposition," *Surf. Coat. Tech.*, vol. 124, pp. 272-277, 2000.
- [23] D. D. Awschalom, et al., "Spin coherence in GaN," Internet: <http://awschweb.physics.ucsb.edu/research/spintronics/gan/index.php>, May 8, 2008 [Feb 19, 2013].
- [24] S. Yoshida, S. Misawa, S. Gonda, "Improvements on the electrical and luminescent properties of reactive molecular beam epitaxially grown GaN films by using AlN coated sapphire substrates," *Appl. Phys. Lett.*, vol. 42, no. 5, pp. 427-429, 1983.
- [25] S. Nakamura, "GaN growth using GaN buffer layer," *Jap. J. Appl. Phys.*, vol. 30, no. 10A, pp. L1705-L1707, 1991.
- [26] H. Morkoç, "Growth and growth methods for nitride semiconductors," in *Handbook of Nitride semiconductors*, vol. 1, Weinheim, Germany: Wiley-VCH, 2008, ch. 3, pp. 323-816.
- [27] S. M. Sze, K. K. Ng, "Physics and properties of semiconductors - a review," in *Physics of Semiconductor Devices*, 3rd ed. New Jersey, Wiley, 2007, ch. 1, pp. 7-133.
- [28] P. Gibart, "Metal organic vapour phase epitaxy of GaN and lateral overgrowth," *Rep. Prog. Phys.*, vol. 67, pp. 667-715, 2004.
- [29] B. Beaumont, et al., "Alternative N precursors and Mg doped GaN grown by MOVPE," *MRS Int. J. Nitride Sem. Res.*, vol. 17, no. 17, 1996.
- [30] S. Nakamura, "The roles of structural imperfections in InGaN-based blue light-emitting diodes and laser diodes," *Science*, vol. 281, no. 5379, pp. 956-961, 1998.

- [31] P. Perlin, et al., "Towards the identification of the dominant donor in GaN," *Phys. Rev. Lett.*, vol. 75, no. 2, pp. 296-299, 1995.
- [32] C. G. Van de Walle, J. Neugebauer, "First-principles calculations for defects and impurities: applications to III-nitrides," *Appl. Phys. Rev.*, vol. 95, no. 8, pp. 3851-3876, 2004.
- [33] H. P. Maruska, J. J. Tietjen, "The preparation and properties of vapor-deposited single-crystalline GaN," *Appl. Phys. Lett.*, vol. 15, no. 10, 1969.
- [34] H. Morkoç, "Extended point defects, doping, and magnetism," in *Handbook of Nitride semiconductors*, vol. 1, Weinheim, Germany: Wiley-VCH, 2008, ch. 4, pp. 817-1230.
- [35] H. Amano, et al., "P-type conduction in Mg-doped GaN treated with low-energy electron beam irradiation (LEEBI)," *Jap. J. Appl. Phys.*, vol. 28, L2112-L2114, 1989.
- [36] S. Nakamura, M. Senoh, T. Mukai, "Highly p-typed Mg-doped GaN films grown with GaN buffer layers," *Jap. J. Appl. Phys.*, vol. 30, L1708-L1711, 1991.
- [37] D. Iida, et al., "Compensation effect of Mg-doped a- and c- plane GaN films grown by metalorganic vapor phase epitaxy," *J. Cryst. Growth*, vol. 312, pp. 3131-3135, 2010.
- [38] M. G. Cheong, et al., "Electrical transport properties of highly Mg-doped GaN epilayers grown by MOCVD," *J. Cryst. Growth*, vol. 221, pp. 734-738, 2000.
- [39] O. S. Elsherif, et al., "Characterisation of defects in p-GaN by admittance spectroscopy," *Physica B*, vol. 407, pp. 2960-2963, 2012.
- [40] M. Miyachi, et al., "The activation of Mg in GaN by annealing with minority-carrier injection," *Appl. Phys. Lett.*, vol. 72, pp. 1101-1103, 1998.
- [41] G. Namkoong, et al., "Metal modulation epitaxy growth for extremely high hole concentrations above  $10^{19} \text{ cm}^{-3}$  in GaN," *Appl. Phys. Lett.*, vol. 93, 172112, 2008.

- [42] R. Y. Korotkov, J. M. Gregie, B. W. Wessels, "Electrical properties of p-type GaN:Mg codoped with oxygen," *Appl. Phys. Lett.*, vol. 78, pp. 222-224, 2001.
- [43] N. R. Perkins, et al., "Halide Vapor Phase Epitaxy of Gallium Nitride Films on Sapphire and Silicon Substrates," in *MRS Fall Meeting*, Boston, MA., 1995.
- [44] H. Morkoç, "General properties of nitrides" in *Handbook of Nitride semiconductors*, vol. 1, Weinheim, Germany: Wiley-VCH, 2008, ch. 1, pp. 1-130.
- [45] A. J. Ptak, et al., "The relation of active nitrogen species to high-temperature limitations for (000) GaN growth by radio-frequency-plasma-assisted molecular beam epitaxy," *Appl. Phys. Lett.*, vol. 74, pp. 3836-3838.
- [46] R. Dingle, et al., "Electron mobilities in modulation-doped semiconductor heterojunction superlattices," *Appl. Phys. Lett.*, vol. 33, pp. 665-667, 1978.
- [47] "Graphene," Internet: [http://mxp.physics.umn.edu/s07/projects/s07\\_graphene/intro.htm](http://mxp.physics.umn.edu/s07/projects/s07_graphene/intro.htm), 2006 [Jan. 22, 2013].
- [48] M. Peter, et al., "New developments in green LEDs," *Phys. Stat. Sol. A*, vol. 206, no. 6, pp. 1125-1129, 2009.
- [49] O. B. Shchekin, et al., "High performance thin-film flip-chip InGaN-GaN light-emitting diodes," *Appl. Phys. Lett.*, vol. 89, 071109, 2006.
- [50] P.P.T. Chen, et al., "High energy Urbach characteristic observed for gallium nitride amorphous surface oxide," *Thin Sol. Film.*, vol. 496, pp. 342-345, 2006.
- [51] E. F. Schubert, I. D. Goepfert, J. M. Redwing, "Evidence of compensating centres as origin of yellow luminescence in GaN," *Appl. Phys. Lett.*, vol. 71, pp. 3224-3226, 1997.
- [52] J. Oila, et al., "Influence of dopants and substrate material on the formation of Ga vacancies in epitaxial GaN layers," *Phys. Rev. B.*, vol. 63, 045205, 2001.

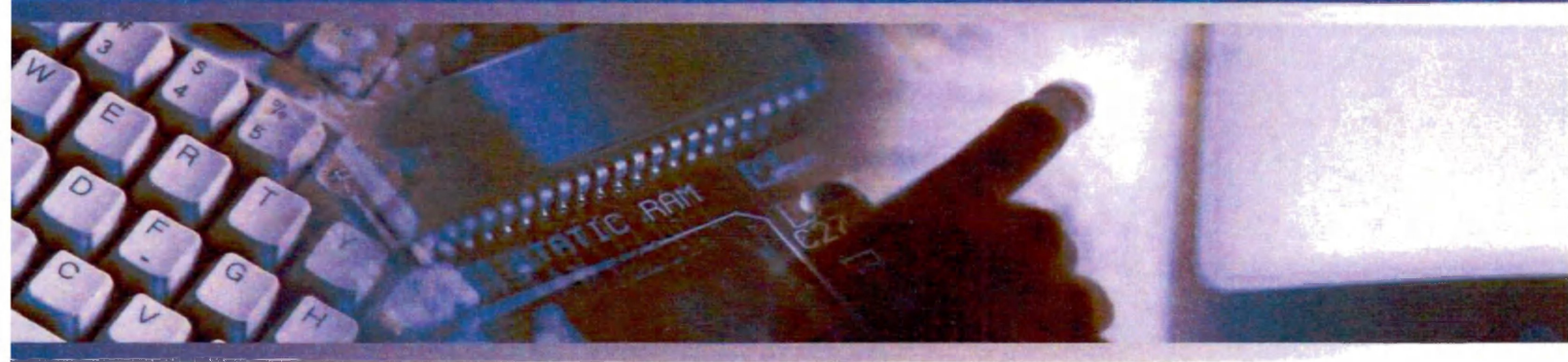
- [53] W. Kim, et al., "Mg doped ptype GaN grown by reactive molecular beam epitaxy," *Appl. Phys. Lett.*, vol. 69, no. 4, pp. 559-561, 1996.
- [54] D. Neamann, "Carrier transport phenomena," in *Semiconductor physics and devices*, New York: McGraw-Hill, 2003, ch. 5, pp. 154-188.
- [55] L. J. Van der Pauw, "A method of measuring specific resistivity and hall effect of discs of arbitrary shape," *Philips Research Reports*, vol. 13, pp. 1-9, 1958.
- [56] L. B. Valdes, "Resistivity measurements on germanium for transistors," *Proc. I.R.E.*, pp. 420-427, 1954.
- [57] C. Tai, "Complementary reciprocity theorems in electromagnetic theory," *IEEE Trans. Ant. Prop.*, vol. 40, no. 6, pp-675-681, 1992.
- [58] S. M. Sze, K. K. Ng, "Metal-semiconductor contacts," in *Physics of Semiconductor Devices*, 3rd ed. New Jersey, Wiley, 2007, ch. 3, pp. 134-196.
- [59] L. Reggiani, et al., "Hole drift velocity in germanium," *Phys. Rev. B*, vol. 16, no. 6, pp. 2781-2791, 1977.
- [60] R. Kube, et al., "Intrinsic and extrinsic diffusion of indium in germanium," *J. Appl. Phys.*, vol. 106, 063534, 2009.
- [61] E. H. Borneman, R. F. Schwarz, J. J. Stickler, "Rectification properties of metal semiconductor contacts," *J. Appl. Phys.*, vol. 76, no. 4, pp. 415-422, 1955.
- [62] "NSM archive - physical properties of semiconductors" Internet:<http://www.ioffe.rssi.ru/SVA/NSM/Semicond>, [Feb 19, 2013].
- [63] D. B. Cuttris, "Relation between surface concentration and average conductivity in diffused layers in germanium," *Bell Sys. Tech. J.*, vol. 40, no. 2, pp. 509-521, 1961.

- [64] "Silicon/germanium resistivity and carrier concentration calculators," Internet: <http://www.solecon.com/sra/rho2ccal.htm>, [Feb 19, 2013].
- [65] P. Blood, J. W. Orton, "Resistivity and Hall effect profiling of non-uniform materials" in *The electrical characterization of semiconductors: majority carriers and electron states*, San Diego, CA.: Academic Press, 1992, ch. 4, pp. 181-219.
- [66] Y. Fu, et al., "Electron mobilities, Hall factors, and scattering processes of n-type GaN epilayers studied by infrared reflection and Hall measurements," *Phys. Rev. B*, vol. 67, 113313, 2003.
- [67] M. Shur, B. Gelmont, M. Asif Khan, "Electron mobility in two-dimensional electron gas in AlGa<sub>N</sub>/Ga<sub>N</sub> heterostructures and in bulk Ga<sub>N</sub>," *J. Electron. Mat.*, vol. 25, no. 5, 1996.
- [68] C. R. Abernathy, "Growth of Group-III nitrides from molecular beams," in *GaN and related materials*, New York, Gordon and Breach, 1997, ch. 2, pp. 11-52.
- [69] "Scanning electron microscope" *Wikipedia*, Internet: [http://en.wikipedia.org/wiki/Scanning\\_electron\\_microscope](http://en.wikipedia.org/wiki/Scanning_electron_microscope) [Feb. 19, 2013].
- [70] R. Yan, D. Gargas, P. Yang, "Nanowire photonics," *Nature Photonics*, vol. 3, pp. 569-576, 2009.
- [71] "Atomic Force Microscopy," *Wikipedia*, Internet: [http://en.wikipedia.org/wiki/Atomic\\_force\\_microscope](http://en.wikipedia.org/wiki/Atomic_force_microscope) [Feb 19, 2013].
- [72] P. Chen, "*Remote plasma enhanced chemical vapour deposition growth and characterisation of polycrystalline indium nitride thin films*," Ph.D. dissertation, Dept. Physics and Astronomy, Macquarie Univ., Sydney, Australia, 2011.
- [73] K. Ng, "Modulation-doped field-effect transistor," in *Complete guide to semiconductor devices*, 2nd ed., New York: Wiley-IEEE press, 2002, ch. 25, pp. 209-218.

- [74] M. Moret, et al., "Optical, structural investigations and band-gap bowing parameter of GaInN alloys," *J. Cryst. Growth*, vol. 311, pp. 2795-2797, 2009.

# Appendix: Instrumentation Specifications

# Hall Effect Measurement System



## HMS-3000

Very Competitive Price, Compact Desktop Design, Easy-To-Use

The Ecopia HMS-3000 Hall Effect Measurement Systems are complete systems for measuring the resistivity, carrier concentration, and mobility of semiconductors.



# Hall Effect Measurement System

## HMS - 3000

### ■ Main Body



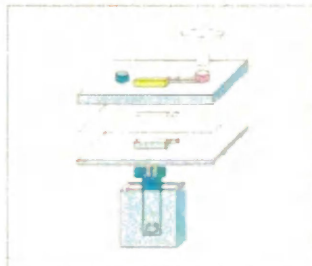
- Precise constant current source : 1nA ~20mA
- Confirm van der pauw law by this system.
- LED for checking Ohmic contact failure.
- Visualizing I-V, I-R curve.

### ■ Magnet Set



- Selectable magnetic set classified by Magnetic Flux Density.(1.0T, 0.51T, 0.37T, 0.31T)
- By ensuring magnet road, minimized outflow of Magnetic Flux Density.

### ■ Low temp test



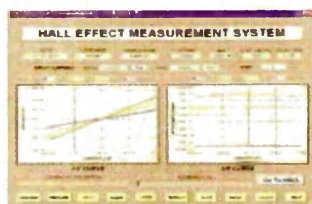
- 77K condition using liquid nitrogen offers simple structure cryostat.
- Sample protection by flowing liquid nitrogen through funnel.
- Measurable dark/light condition : built-in special material to intercept light.
- Maintain 15min at 77K by special insulating material.

### ■ HMS-3000 Software



- Results : bulk/sheet concentration, mobility, resistivity, magnetoresistance, hall coefficient (RH, RH1, RH2), conductivity, V/H ratio of resistance.

### ■ I-V, I-R Curve



- As applying input current, user can get I-V, I-R curve ranging from initial to final value.

## SPECIFICATION

<b>SIZE (W×D×H) : MAIN BODY</b>	<b>320×300×105 mm</b> <b>(Constant Current Source/Meter System)</b>
<b>WEIGHT :</b>	<b>7.7kg(without package)</b>
<b>MEASURABLE SAMPLE SIZE :</b>	<b>6mm×6mm,</b> <b>20 mm×20 mm</b>
<b>MEASUREMENT TEMPERATURE :</b>	<b>300K, 77K(Liquid Nitrogen)–Keep temp</b> <b>for 15min.</b>
<b>MEASUREMENT MATERIALS :</b>	<b>All semiconductors including Si, ZnO,</b> <b>SiGe, SiC, GaAs, InGaAs, InP, GaN</b> <b>(N Type &amp; P Type can be measured).</b>
<b>PERMANENT MAGNETIC SIZE</b>	<b>50mm Diameter</b>
<b>MAGNETIC FLUX DENSITY :</b>	<b>0.31, 0.37T, 0.51T, 1.0T</b>
<b>INPUT CURRENT RANGE</b>	<b>1nA-20mA, Compliance: 13V</b>
<b>MOBILITY(cm<sup>2</sup>/Volt-sec)</b>	<b>1~10<sup>7</sup> (including low temperature)</b>
<b>DENSITY(cm<sup>-3</sup>) :</b>	<b>10<sup>7</sup>~10<sup>21</sup></b>
<b>VOLTAGE MEASUREMENTS:</b>	<b>Input impedance: 2 x 10<sup>7</sup></b> <b>Input voltage range: +/- 12V</b>
<b>RESISTIVITY RANGE:</b>	<b>10<sup>-4</sup>~10<sup>7</sup> Ohms-cm</b>

For further information  
please contact:



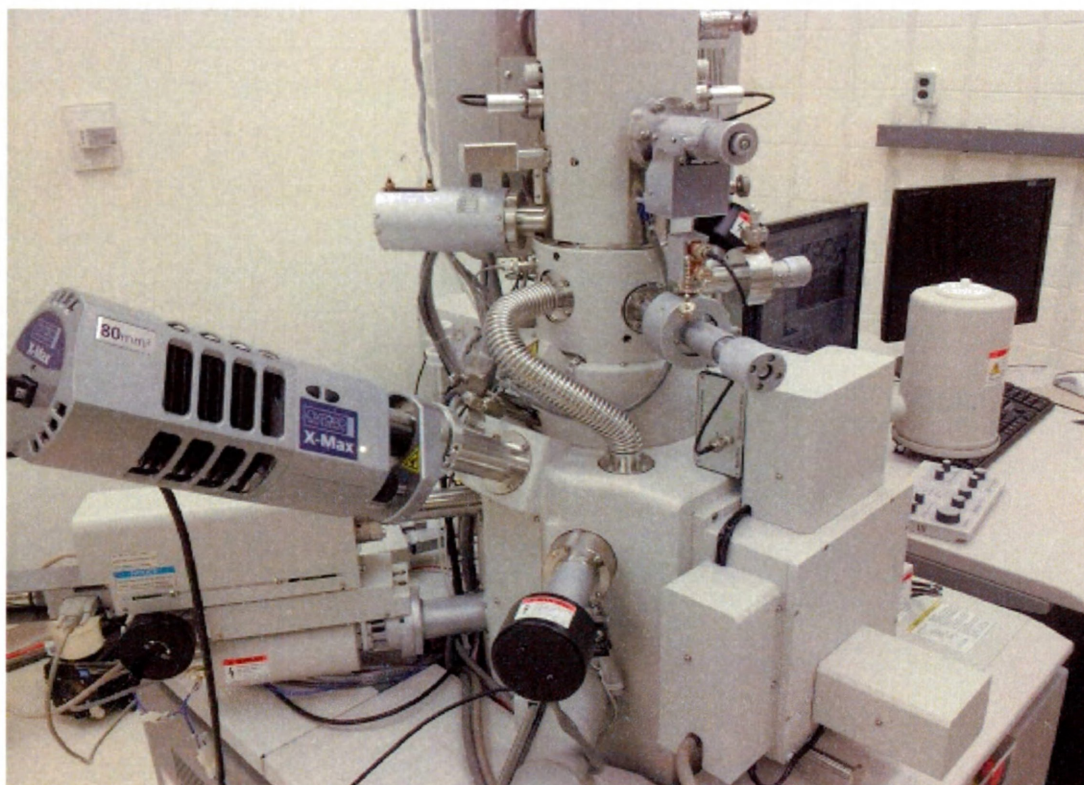
**Bridge  
Technology**

Bridge Technology  
(480) 988-2256 (in USA)  
sales@bridgetec.com

# SEM/EDS: Hitachi Su-70 Schottky Field Emission

## Scanning Electron Microscope (SEM/EDS)

The Scanning Electron Microscope/ Energy Dispersive Spectrometer (also termed SEM/EDXA) facilities at Lakehead University are used by a variety of departments including Anthropology, Biology, Chemistry, Engineering, Forestry, Geology and Physics. Training courses are available for honors and graduate students who require the instrument for their projects. The instrument is invaluable for examinations of microscopical structures including many biological and chemical materials and combined with its ability to measure elemental composition from areas as small as a few microns, it is an important tool for solving many industrial problems.



Close up of scanning electron microscope

## Equipment

### Hitachi Su-70 Schottky Field Emission SEM

Resolution is 1.0nm @15kv/ 1.5 nm at 1 kv

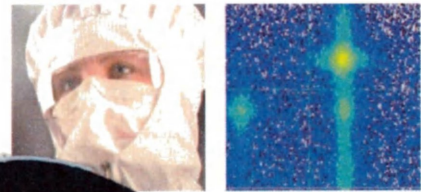
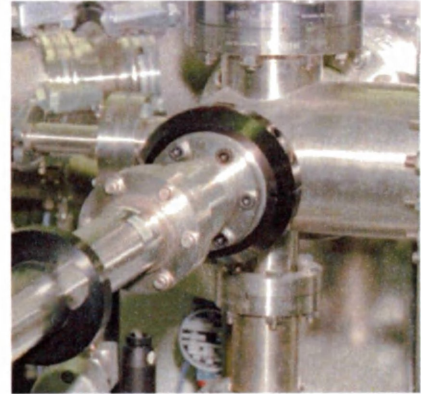
Stage size is 110mm. Analytical working distance is 15mm

Includes:

- Oxford Aztec 80mm/124ev EDX
- Specimen exchange airlock
- Gatan Mini CL (185nm-850nm)
- STEM detector
- Below the lens solid state 5 segment BSE detector
- Column faraday cup with HTC current monitorLiquid nitrogen based anti-contamination device

## ADVANCED X-RAY ANALYSIS

**X'Pert PRO MRD for new materials research and development**



## Advanced and innovative X-ray diffraction solutions



Progress in advanced semiconductor and thin film materials research has brought great changes to the way we live. It has driven the developments we now regard as a routine part of daily life. Fundamental to these is the significant progress in our knowledge and management of the physical, chemical and structural properties of semiconductors and advanced materials. X-ray diffraction (XRD) has proved to be an indispensable technique for revealing and analyzing the smallest structural details in a wide range of different materials. PANalytical's X'Pert PRO Materials Research Diffractometers have already played a major role in this area, and continue to work at the cutting edge, advancing the understanding of materials – from research to process development.

### PreFIX modules – fast, flexible and future-proof

PANalytical's proprietary PreFIX concept makes the X'Pert MRD PRO flexible, fast and future proof. The PreFIX mounting method of optics and stages allows the diffractometer to be reconfigured in minutes without realignment. When new tasks arise or when new X-ray applications are developed, simply add the necessary modules.

An extensive range of PANalytical PreFIX modules can be used with X'Pert PRO MRD systems, including:

- an X-ray mirror
- hybrid monochromators
- high-resolution monochromators
- an X-ray lens
- a mono-capillary
- the X'Celerator
- the high-end solid-state PIXcel detector

### X'Pert PRO MRD systems

X'Pert PRO Materials Research Diffractometers (MRD) are part of PANalytical's X'Pert PRO family of XRD systems. They have been specifically designed to meet the requirements of modern materials research and development laboratories:

**X'Pert PRO MRD** – the standard research and development version for use with thin film samples, wafers (up to 8 inches in diameter and complete mapping up to 4 inches) and solid materials

**X'Pert PRO MRD XL** – an enlarged version for use with bigger wafers (up to 300 mm in diameter) and complete wafer mapping up to 200 mm, suitable for process development.

Both systems can handle a wide variety of techniques for the analysis of thin films and new materials. These include high-resolution diffraction, reflectivity, thin film phase analysis, wafer mapping, stress and texture, and phase identification. Special additions enable high-intensity, high-resolution analysis and in-plane diffraction:

**extended arm option** - X'Pert PRO Extended MRD for high-resolution analysis with high intensities

**in-plane diffraction option** - X'Pert PRO MRD for the analysis of very thin films

The instruments all offer the advantages of PANalytical's PreFIX (Pre-aligned Fast Interchangeable X-ray) concept. This proprietary system ensures fast, flexible exchange of components, including optical modules. It provides a virtually unlimited capacity to adapt to changing requirements without time-consuming re-alignment.

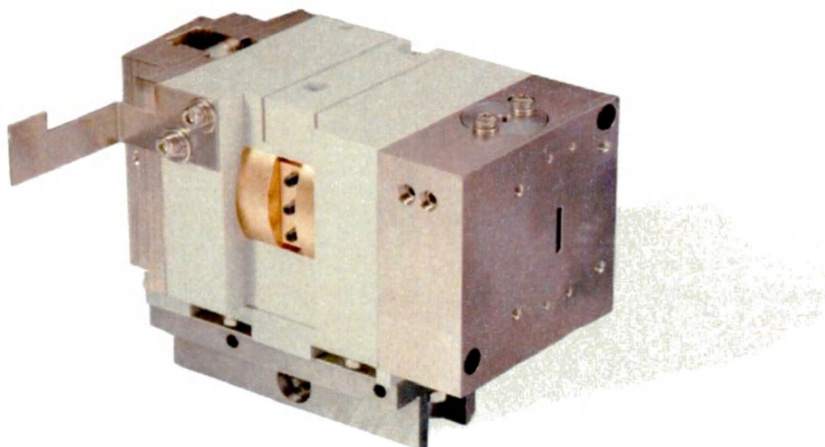
### Pioneers in materials research

With more than fifty years experience in X-ray analysis, PANalytical is committed to remaining at the forefront of developments in materials science. And the X'Pert PRO MRD range is the world's most widely used high-resolution diffraction system.

The introduction of the X'Pert PRO MRD XL has broadened its applicability, encompassing basic and applied research in advanced materials and moving into process development.

### X'Pert Software

PANalytical's X'Pert Data Collector, a powerful central module in the X'Pert Software range, is used to control all X'Pert PRO MRD systems. Optional the software module X'Pert Operator Interface is available to simplify complex measurements to the level of an operator push button action. Based on industry standard XML, and designed specifically for data acquisition and analysis, X'Pert Software supports all application techniques for advanced X-ray analysis.



# Nanosurf®

Microscopy Made Easy

Nanosurf Instruments

Nanosurf Didactic

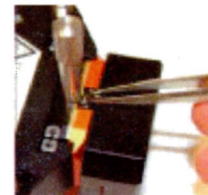
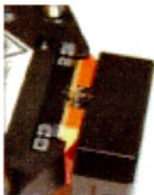
## Key Technologies

### Smart Scanner Features

Instead of piezoelectric materials that require high voltages and are vulnerable to creep, the Easyscan 2 AFM uses a patented electromagnetic scanner that boasts an XY-Linearity Mean Error of less than 0.6% with low noise and low power consumption. This and similar smart design features allow a significant reduction in cost and size without loss of precision performance. The Easyscan 2 AFM makes professional high resolution surface measurements available to everyone.

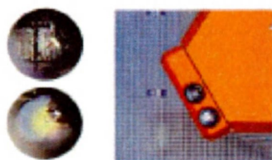
### Simple Cantilever Exchange

Replacing a cantilever only requires three simple steps and no laser adjustment, thanks to the the smart design of the Easyscan 2 cantilever spring and the use of cantilever alignment chip technology:



1. Cover the scanner with the DropStop 2: Lift the cantilever holder 3. Replace the cantilever

### Easy Positioning



The two view lenses built into the Easyscan AFM offer a top view that shows where on the sample the cantilever is positioned and a side view that shows the probe-sample distance. Positioning the sample for measurement thus becomes simple and intuitive.